EXPERIMENTAL INVESTIGATION OF FLOW BOILING OF WATER IN NARROW RECTANGULAR VERTICAL CHANNELS

Von der Fakultät Maschinenbau der Universität Stuttgart
zur Erlangung der Würde eines Doktoringenieurs (Dr.-Ing.)
genehmigte Abhandlung

vorgelegt von

Ewelina Sobierska
aus Jarocin, Polen

Hauptberichter: Prof. Dr.-Ing. habil. M. Groll
Mitberichter: Prof. Dr.-Ing. habil. H. Müller-Steinhagen

Tag der mündlichen Prüfung: 27.10.2008

Institut für Kernenergetik und Energiesysteme der Universität Stuttgart
2009

Contents

List of Tables

List of Figures

Abstract

In the last century electric and electronic devices have become an integral part of our life. Simultaneously, in pursuance of people's nature, needs and demands are incessantly increasing. Consequently, the devices are becoming more convenient (by means of being smaller and lighter) and the number of their functions is rising. One of the restrictions which stop this development is the Joule effect which creates a thermal management problem. Many options to achieve successful cooling are available, ranging from very simple passive cooling to active cryogenics methods. Among those, flow boiling offers very good heat transfer performance taking advantage of the latent heat of vaporisation.

During flow boiling in microchannels a liquid coolant is pumped through an array of channels which can be attached to heated surfaces. A closed loop containing an evaporator with microchannels, a micropump and a condenser can be very compact and relatively inexpensive. There are three aspects of flow boiling: flow pattern, pressure drop and heat transfer. All three and their relationship are experimentally investigated in this work with the aim to find the best heat transfer performance conditions. The experiments were carried out in three rectangular channels with hydraulic diameters below $0.5\ mm$. Deionised water was used as working fluid. The heat transfer and pressure drop were investigated. Additionally a visualisation of two-phase flow was done in order to obtain a better understanding of the heat transfer mechanism.

The results of this work can be briefly summarized as follows: The best heat transfer performance was found at thermodynamic vapour qualities close to zero, where slug flow was usually observed. The two-phase pressure drop can be predicted by a separate flow model which is based on governing equations (mass, energy and momentum conservation laws), the Lockhart-Martinelli method and the empirical void fraction equation with constants proposed by Lockhart and Martinelli.

Kurzfassung

In dem letzten Jahrhundert sind elektrische und elektronische Geräte ein wesentlicher Bestandteil unseres Lebens geworden. Gleichzeitig steigen, bedingt durch die Natur der Menschen, ihre Bedürfnisse und Anforderungen ständig. Infolgedessen werden verfügbare Geräte immer komfortabler (kleiner und leichter) und die Zahl ihren Funktionen steigt. Eine der Beschränkungen, die der Phantasie eine Grenze setzen, ist der Jouleeffekt, der ein thermisches Managementproblem verursacht. Viele erfolgreiche Kühlmethode existieren, vom sehr einfachen passiven Kühlen bis zu aktiven kryogenen Kühlmethoden. Unter ihnen bietet das Strömungssieden eine sehr gute Wärmeübertragungsleistung. Dabei wird die latente Verdampfungswärme genützt.

Beim Strömungssieden in engen Kanälen wird ein flüssiges Kühlmittel durch eine Matrix von Kanälen gepumpt, die an beheizten Oberflächen angebracht werden können. Ein entsprechender geschlossener Kreislauf, der einen Verdampfer mit engen Kanälen, ein Mikropumpe und einen Kondensator umfasst, kann sehr kompakt und verhältnismäßig preiswert sein. Es gibt drei Aspekte des Strömungssiedens: Strömungsmuster, Druckverlust und Wärmeübergang. Alle drei und ihre gegenseitigen Beziehungen werden in dieser Arbeit experimentell untersucht. Das Ziel war, die besten Wärmeübertragungsbedingungen zu finden. Die Versuche wurden in drei rechteckigen Kanälen mit hydraulischen Durchmessern unter $0.5\ mm$ durchgeführt. Demineralisiertes Wasser wurde als Wärmeträger benutzt. Die Wärmeübertragung und der Druckverlust wurden untersucht. Zusätzlich wurde die Zweiphasenströmung visualisiert, um ein besseres Verständnis der Wärmeübertragungsmechanismen zu erhalten.

Die Ergebnisse dieser Arbeit können kurz folgendermaßen zusammengefasst werden: die höchsten Wärmeübertragungskoeffizienten erhält man in engen Kanälen für thermodynamische Dampfqualitäten nahe Null. Dabei wird gewöhnlich Pfropfenströmung beobachtet. Der zweiphasige Druckverlust kann mit einem ”separated flow”-Strömungsmodell vorausgesagt werden. Dieses basiert auf den Erhaltungsgleichungen, der Lockhart-Martinelli-Methode und der empirischen Dampfgehaltgleichung mit den von Lockhart und Martinelli vorgeschlagenen Konstanten.

Acknowledgements

”What did I?” - I asked myself some years ago in a hotel after signing the contract with IKE. Now I can tell that it was one of the best decisions which I made (sticking to the assumption that the period while my set-up refused to cooperate was the time to open my mind and to practice my patience). The time at IKE would not have been so great without the people whom I was lucky to meet.

First I would like to express my sincere thanks to my advisor, Prof. Manfred Groll, for the support and guidance throughout this work. I thank him for his patience and efforts that drove me to give the best of myself. I also thank Prof. Hans Müller-Steinhagen for accepting to be the thesis co-examiner.

A huge thanks for all the friends at the institute. For Dr. Rudi Kulenovic and Dr. Rainer Mertz, the group leaders, for the patience, the indulgence and the support in all cases. For Dr. Yuming Chen, with whom I had many helpful discussions. For Dr. Patrick Schäfer, who provided invaluable support whenever I needed especially during the initial days of my stay in Germany. For Ying Fu, who tried to show me the spiritual aspect of life.

I would also like to thank the institute/university administrators, research collaborators/financiers and technical/secretarial staff for their active support throughout my doctoral program.

There is no way to omit here my family and friends without whom everything would have been without sense, especially my Mother, who believes in myself more than I ever did, to Vivak and to Olek. There are no words to express how important they are for me. I only believe that they know about it.

Nomenclature

a	aspect ratio, $-$
A_{cs}	cross-section area, m^2
A_{ht}	heat transfer area, m^2
B	bias limit (fixed error), $-$
C_O	distribution parameter, Eq. 2.8, $-$
c_p	specific heat capacity, $J/kg\ K$
d_h	hydraulic diameter, m
f	friction factor, $-$
F'	parameter in Eq. 2.25, $-$
g	gravitational acceleration, m/s^2
G	mass flux, kg/m^2s
h	depth of channel, m
h	heat transfer coefficient, $W/m^2\ K$
Δh_{lg}	latent heat of vaporization, J/kg
i	specific enthalpy, J/kg
j	superficial velocity, m/s
K	Poiseuille constant, $-$
K'	slip ratio, $K' = u_g/u_l,\ -$
L	length, m
$\dot{m}$	mass flow rate, kg/s
M	number of parameters, $-$
MAE	mean absolute error, $MAE = \sum \lvert y_{exp} - y_{calc} \rvert 100 / \sum y_{exp},\ \%$
N	number of samples, $-$
p	pressure, Pa
P	wetted perimeter of channel, $P = 2(w + h),\ m$
Q	heat flow, W
q	heat flux, W/m^2
R^2	coefficient of determination, $-$
R_a	roughness (average deviation from the mean line), μm
S	heated perimeter of channel, $S = w + 2h,\ m$
S	precision index in Eqs. G.5 and G.6, $-$
S'	parameter in Eq. 2.26, $-$
T	temperature, K

t	Student's multiplier, $-$
u	velocity, m/s
U	uncertainty, %
V	volume, m^3
$\dot{V}$	volumetric flow rate, m^3/s
w	width of channel, m
x	independent parameter, $-$
	coordinate, m
X	Lockhart-Martinelli parameter, $-$
X_{tt}	Lockhart-Martinelli parameter for gas turbulent- liquid turbulent flow, $-$
x	vapour quality, $-$
y	results,
z	distance from inlet, m

Nondimensional numbers

Bo	Boiling number, $Bo = q/(G\Delta h_{lg}),\ -$
Co	confinement number, $Co = [\sigma/\left((\rho_l - \rho_g)gd_h^2\right)]^{0.5},\ -$
$N_{\mu l}$	viscosity number, Eq. 2.12, $-$
Nu	Nusselt number, $Nu = d_h h/\lambda,\ -$
Pr	Prandtl number, $Pr = c_p\mu/\lambda,\ -$
Re	Reynolds number, $Re = Gd_h/\mu,\ -$
We	Weber number, $We = \rho u^2 d_h/\sigma,\ -$

Greek symbols

α	void fraction, $-$
β	contact angle, $^\circ$
μ	dynamic viscosity, $Pa\,s$
ν	specific volume, m^3/kg
ρ	density, kg/m^3
σ	surface tension, N/m
τ	shear stress, Pa
λ	thermal conductivity, $W/m\,K$
Φ	two-phase multiplier, $-$
Θ	inclination angle to the vertical line, $^\circ$

Subscripts

A	acceleration
ad	adiabatic
c	circular
$calc$	calculated
CBD	convective boiling dominant
cs	cross-section

exp	experimental
F	frictional
g	gas
G	gravitational
i	number of parameter
in	inlet
k	sample number
l	liquid
lo	liquid only
loss	loss
NBD	nucleate boiling dominant
ONB	onset of boiling
out	outlet
pl	plate
sat	saturation
sp	single-phase
th	thermodynamic
tp	two-phase
ts	test section
vb	vapour body
vw	viewer window
w	wall

Chapter 1

Introduction

This chapter presents briefly actual thermal management problems with their reasons and possible solutions. Small scale devices enlarge the problems. Flow boiling is one of the available cooling methods with a heat flux capacity of order of 100 W/cm^2 or even more [1] which makes it a very important field of investigations. An effective design of a micro heat exchanger requires detailed knowledge of the characteristics of heat transfer and fluid flow mechanisms in such structures. Therefore, the aim of this work is to experimentally investigate such phenomena during flow boiling in narrow channels in order to find the optimal heat transfer conditions.

1.1 Thermal management problems in the era of miniaturisation

In the last century electric and electronic devices have become an integral part of our life. Simultaneously, in pursuance of people's nature, needs and demands are incessantly increasing. Consequently, the devices are becoming more convenient (by means of being smaller and lighter) and the number of their functions is rising. One of the restrictions which stop the imagination is the Joule effect. This phenomenon can be briefly explained in the following way: when electric current flows in a conductor, work is generated by the electric field accelerating the charges constituting the current. Due to the electrical resistance this work is transformed into heat. If a large amount of heat is generated, the increased temperature may damage the device. Already in 1965, Gordon E. Moore, before he co-founded Intel (1968), bravely predicted that the number of integrated circuit components will be increasing at a rate of roughly a factor of two per year. In 1975, he updated his prediction to doubling

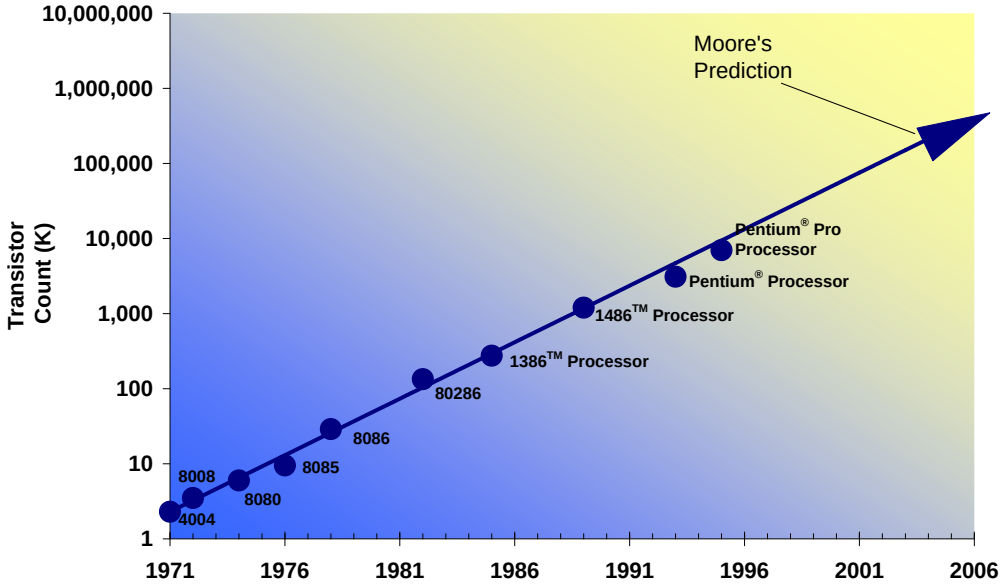

Figure 1.1: Moore's law [2]

in 18 months and in 1995 to doubling in every two years. History shows that he was very close to the truth, Fig. 1.1

The rapid development and wide application of high performance very large-scale integration (VLSI) technology resulted in a significant improvement of the electronic and microelectronic devices. The increase of integrated circuit components on a chip together with miniaturisation of electronic devices caused the growing power density, and consequently the thermal management became a big challenge. The evolution of ink-jet printing technology and microelectro-mechanical systems showed that hydraulic diameters even less than 200 μm became relevant. The development of MEMS (micro-electro-mechanical systems) in engineering, biomedical and genetic research opened a whole new field on micro-level for new cooling methods. Many options to achieve successful cooling are available, ranging from very simple passive cooling to cryogenics methods. There are different ways to systematise cooling systems. One divides the methods into two broad categories: passive and active cooling [3].

Passive cooling: fluid movement occurs in a natural way (e. g., natural convection), energy is transported by conduction and/or radiation heat transfer. In such systems, designers typically attempt to utilise conduction and radiation as the primary modes of heat transfer to maximise the thermal transport and to induce higher levels of natural convection. Additional conductive plates and/or heat sinks specifically designed are made to spread the heat. In limited spaces heat pipes can be used as heat transport elements from the devices to places where heat can be easier removed from the system (Fig.1.2).

Figure 1.2: Heat pipe and heat spreader combination [3]

Active cooling: fluid motion is caused by an external source, a fan in a forced air cooled system or a pump in a liquid cooled system or in a refrigeration cooling system.

A further distinction may be made between indirect and direct cooling (Fig. 1.3). *Indirect liquid cooling* is one in which the liquid is separated by a high thermal conduction path from the microelectronics chips and from the substrate upon which the chips are mounted. Since there is no contact with the electronics, water can be used as the liquid coolant, taking advantage of its superior thermophysical properties.

Direct liquid cooling may also be termed direct liquid immersion cooling, since heat-dissipating electronic components are not physically separated from the coolant. This form of cooling offers the opportunity to remove heat directly from the chip(s) with no intervening thermal conduction resistance, other than that between the device heat sources and the chip surfaces in contact with the liquid. Interest in direct liquid immersion as a method for cooling integrated circuit chips may be traced back as early as the 1960s [4].

In order to select a suitable cooling method a number of factors such as the required cooling capacity, cost and spatial constrictions have to be considered. A short description of available and common cooling methods is presented below.

Single-phase cooling technology can be divided into natural and forced convection cooling. Air natural convection is the simplest solution but can be applied only in application with low heat fluxes. Typical heat transfer coefficients for natural convection with air, which is widely used as a cooling method in e. g. PCs, range from 5 to 12 W/m^2K. Single-phase forced convection offers $5-12$ times higher heat transfer coefficients (compared to the corresponding natural convection method), however with extra costs for fans or pumps. Immersing in

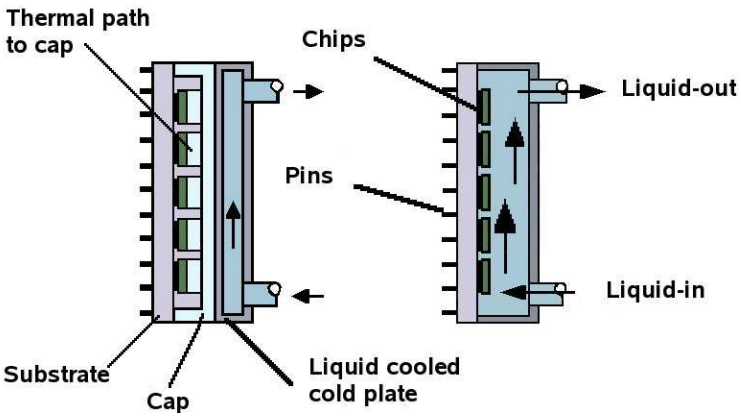

Figure 1.3: Example of indirect (left side) and direct liquid (right side) immersion cooling for a multi-chip module package [4]

fluoro-chemical dielectric liquids enhances the heat transfer coefficient up to $200 - 500\ W/m^2K$.

In both cases (natural or forced convection) a gas (e. g. air, nitrogen) or a liquid (e. g. water, refrigerants) can be used as working fluid. The major benefit of changing from gas to liquid cooling is increased packaging density and lower noise. One significant difference to air cooling is the volumetric thermal capacity of water, close to 4000 times compared to air. The volume of water required per hour will be slightly lower than the volume of air required per second to provide the same thermal capacity. On the other hand liquid cooling can create potential problems, such as leakage, corrosion, extra weight, condensation, etc. While water may be employed for indirect cooling, use of dielectric fluids is necessary for direct cooling options. Liquids used in direct cooling must meet such requirements as high thermal conductivity, chemical inertness and high boiling point [5].

Because of high latent heat required for vapour generation the two-phase cooling systems offer very good cooling efficiency with moderate wall superheat. Pool boiling, falling film, liquid jet impingement, spray cooling, heat pipes and flow boiling represent two-phase cooling methods.

Pool boiling is the simplest example of the phase change electronics cooling technique, where the boiling takes place at a hot surface immersed in a pool with a dielectric fluid. The heat transfer coefficient is about $10 - 50$ times higher than that for single phase forced convection with the same working fluid (Chu 1999 [6], cited from [5]). The critical heat flux imposes a maximum limit to the dissipation heat flux [5]. Additional improvement can be obtained by enhanced surfaces. Depending on liquid, working conditions and given surface structure the heat transfer performances can be several times better than that of plain surfaces [7].

Table 1.1: Summary of cooling methods

	method	advantages	disadvantages/drawbacks
single-phase technology	air/liquid natural convection	- simplicity - low cost - reliability	- very low heat transfer coefficient
	air/liquid forced convection	- higher heat transfer rates than by natural convection	- extra costs for fan or pump - noisy (by air forced convection)
two-phase technology	pool boiling	- the simplest case of two-phase cooling	- requires relatively large space
	falling film	- higher convective heat transfer coefficients and a higher CHF than for pool boiling - pumped closed loop	- extra equipment - temperature overshoot - lack of versatility in orientation - complicated cooling process - uncontrolled cooling
	liquid jet impingement	- boiling heat flux up to 70 W/cm^2 - pumped closed loop	- re-circulated loop - sophisticated control system - restricted operational conditions - surface erosion - nozzle obstruction
	spray cooling	- uniform surface temperature - good cooling performance - no surface erosion - pumped closed loop	- sophisticated control system - restricted operational conditions
	flow boiling	**- compactness - pumped closed loop - easy attachment onto hot surface**	**- extra cost for pump**
special technology	heat pipes	- efficient cooling - no extra equipment - low costing - no moving parts	- suitable only for moderate heat flux dissipation (order of 50 W/cm^2)
	capillary pumped loop, loop heat pipe	- heat flux up to 125 W/cm^2 - capability to transport heat on long distances - no moving parts	- relatively high cost
	thermoelectric devices	- compactness - quiet - free of moving parts - easy controlled	- suitable only for low heat flux dissipation - cost of material and additional power consumption - low coefficient of performance
	curved-channel cooling/rotating -stirrer cooler	- very good cooling efficiency	- extra equipment
	refrigeration/ cryogenics cooling systems	- very good cooling performance	- extra equipment - requires large space

Falling film cooling is achieved by gravity driven flow of the coolant passing over a vertical/inclined hot surface or chip assembly. Boiling is induced to enhance heat transfer performance over the hot surface. Although this technique has demonstrated higher CHF than pool boiling, due to various constraints and different limitations (see Table 1.1), it is not very popular (Grimley et al., 1988 [8], cited from [5]).

Liquid jet impingement involves jets of liquid coolant passing over the heated surface providing an extremely effective means of dissipating large heat fluxes at low operating temperatures. The design may involve solely single-phase jets or alternatively surface boiling may be induced achieving very high heat fluxes of the order of 70 W/cm^2. The impinging jet forms a very thin hydrodynamic and thermal boundary layer and heat transfer coefficients of the order of 100 W/m^2K have been obtained for single-phase jets [9]. The performance is affected by jet geometry, low Reynolds number, presence of confinement walls and distance between the jet and the dissipating heated chips [Vader et al. [10] and Chrysler et al. [11], cited from [5]]. However, the need of a re-circulation loop, control of jet velocity, possibility of surface erosion and nozzle obstruction are some of the major disadvantages. Another variation of jet impingement to achieve a more uniform temperature distribution and to avoid surface erosion is *spray cooling*. A much slower stream of coolant is applied and continuous formation and evaporation of a thin liquid film is achieved.

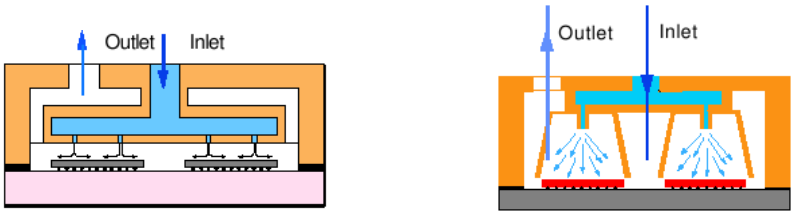

Figure 1.4: The module at the left employs liquid jet impingement cooling. The model at the right uses spray cooling. [12]

Thermoelectric devices are based on the Peltier effect, by which a temperature gradient develops across two joined dissimilar materials when a DC current is applied across them. This effect is explained in the following way: electrons speed up or slow down under the influence of a contact potential difference. In the first case the kinetic energy of the electrons increases and then turns into heat. In the second case the kinetic energy decreases and the joint temperature drops. In case of usage of semiconductors of p- and n- types the effect becomes more vivid (Fig. 1.5). Combination of many pairs of p- and n-semiconductors allows to create cooling units - Peltier modules - of relatively high power (Fig. 1.6).

The Peltier effect found practical applications in the mid-1950s, although the

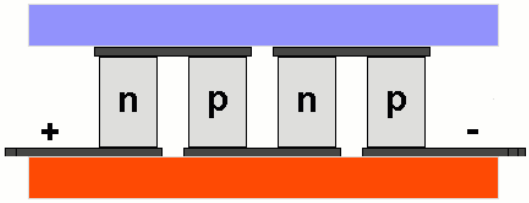

Figure 1.5: Peltier effect. Usage of semiconductors of p- and n- type in thermoelectric coolers [www.digit-life.com/articles/peltiercoolers]

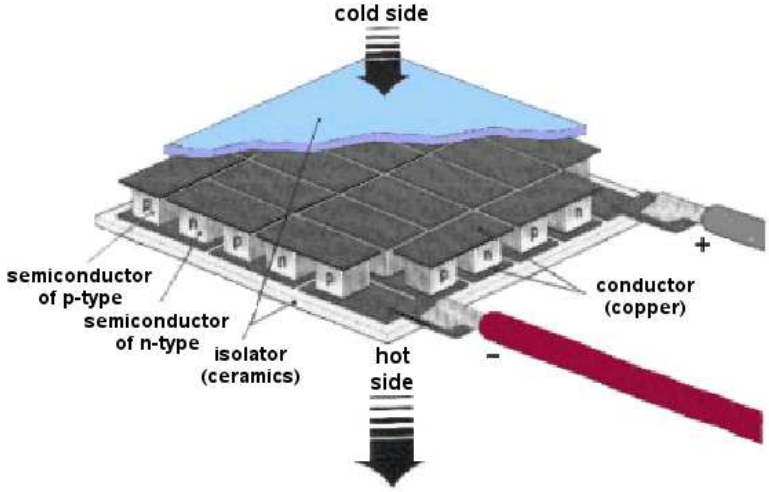

Figure 1.6: Peltier module [www.digit-life.com/articles/peltiercoolers]

thermoelectric phenomenon is known since 1834. Only the development of suitable semiconductor materials like Bi_2Te_3 (Bismuth-Telluride) made it possible to attain a temperature difference of about $60 - 70°C$. Therefore the temperatures can be even below the ambient temperature. The disadvantages given in Table 1.1 have generally limited thermoelectrics to specialised niche applications characterised by low heat fluxes [13].

A *heat pipe* is a highly efficient passive heat transport element. It consists of three sections: evaporator, adiabatic section and condenser, e.g. in the form of a closed tube. Heat from a source is added to the evaporator. In this section the working fluid, which is in equilibrium with its own vapour, is vaporised and afterwards flows to the condenser driven by the small pressure difference between the hot and the cold ends. The vapour is condensed in the cold condenser section. During the phase changes, the fluid takes up or releases, respectively, latent heat of vaporisation/condensation. Through a capillary structure, e.g. at the heat pipe wall, the liquid flows back from the condenser to the evaporator driven by capillary forces. By virtue of capillary pumping action, the heat pipe can be operated in a micro gravity field (as

in satellites) or against gravity (on the ground with the evaporator above the condenser).

A *pulsating heat pipe* is a bare small diameter tube (no capillary structure inside) with many turns. It can be either of closed loop design (tube ends are connected to each other) or open loop design (tube ends are closed and not connected to each other) [14]. It is partly filled with a liquid. Upon heating the evaporator an oscillation of bubbles and liquid slugs is induced between evaporator and condenser. Thereby thermal energy is transported mainly in the form of sensible heat from the hot side to the cold side.

Capillary pumped loops (CPLs) and *loop heat pipes* (LHPs) are two-phase heat transfer devices with capillary pumping of a working fluid. They possess all the main advantages of conventional heat pipes, but owing to the design and special properties of the capillary structure, are capable of transferring heat efficiently over distances up to several meters at any orientation in the gravity field, or over several tens of meters in a horizontal position. However, a potential reliability problem can prevent their application in microsystems cooling. If any vapour or gas bubbles exist in the liquid return line, the capillary pumping can be blocked. For a CPL, heat fluxes have been reported of order of $125\ W/cm^2$ by Kirshberg ([15] cited from [5]). A new generation of LHP-miniature heat pipes-seems to be a promising solution for thermal management problems in electronics and computer equipment [16].

The centrifugal force is used in *curved-channel cooling* to enhance the contact between liquid and hot surface (hence extension of the nucleate boiling range) and in a *rotating-stirrer cooler* to drive the liquid coolant radially outwards to the vessel wall. The chips have to be mounted on curved channels in the first case and on the inside wall of a cylindrical vessel in the second one. Therefore a significant change in the configuration of an electronics device is required and consequently the practical application of such method is limited [5].

During *flow boiling* in microchannels a liquid coolant is pumped through an array of channels which can be attached to hot surfaces. The removed heat fluxes can be of the order of $100\ W/cm^2$ or even more [1]. A closed loop containing an evaporator with microchannels, a micropump and a condenser, usually employing water, can be very compact and relatively inexpensive [5]. The microchannel structure can exist either as a parallel channel system or a fractal structure [17] or in any required shape. The parallel channel system, called also multichannels, is commonly investigated considering single-phase ([18], [19], [20]) and two-phase ([1], [21], [22]) flow. The cross-section of channels may have a rectangular/triangular/trapezoidal/etc. shape. But in such structures there is an interaction between heat transfer processes in neighbouring channels. The uniform distribution of working fluid yields an additional problem.

Cryogenics and refrigeration loops are characterised by very good cooling efficiency but their application is limited due to the large space requirement. Additionally they require a complex equipment (Fig. 1.7). More details about this cooling method can be found in reference [12].

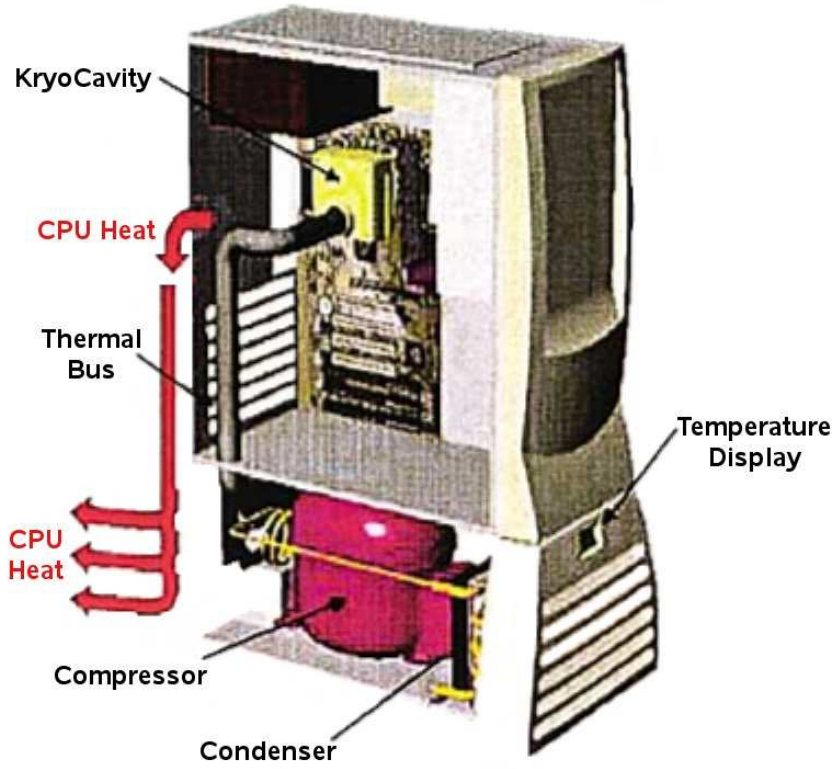

Figure 1.7: The first commercially available refrigerated processor [12]

Summarising the available cooling methods (see Fig.1.8 and Table 1.1) it is clear that natural convection methods have the lowest cooling efficiency but on the other hand they are characterised by low cost, simplicity and reliability. A heat flux of moderate level can be removed by using single-phase forced convection with extra costs for fan or pump. The best cooling can be obtained by applying phase change methods. Such solutions require a more or less complex re-circulating loop.

1.2 The aim of work

As mentioned earlier, flow boiling is characterised by one of the best heat transfer performances (see Fig. 1.8). Because of decreasing size of electronic devices heat transfer has to occur in small size hydraulic diameter channels. Up to now, there is no uniform and adequate theory to describe the fluid

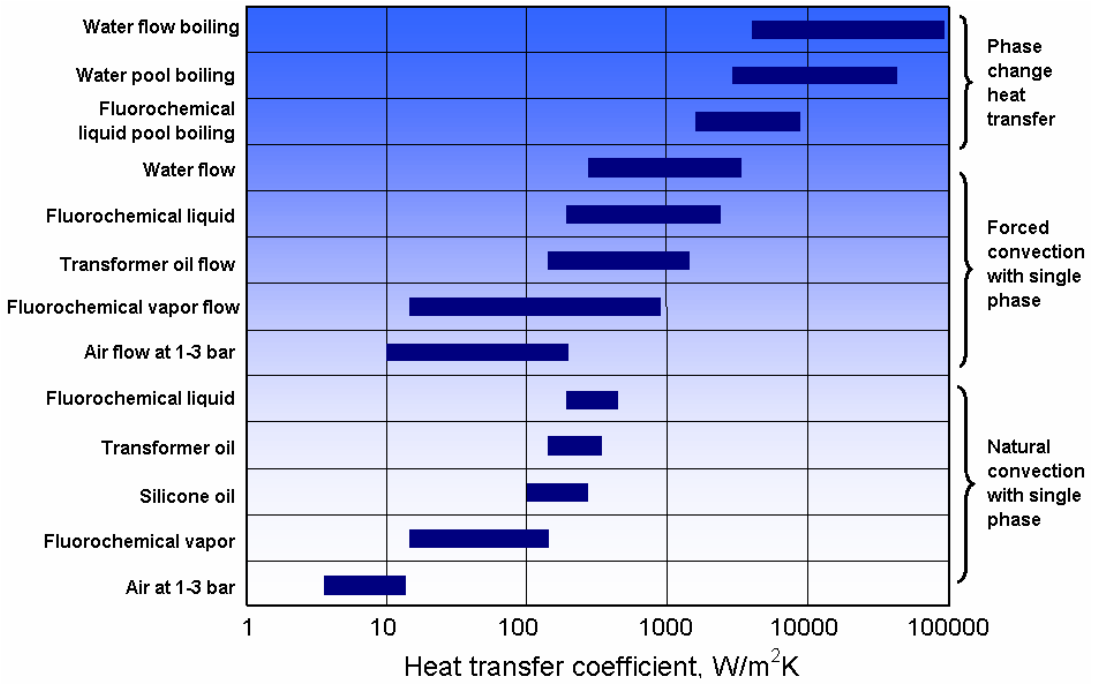

Figure 1.8: Achievable ranges of heat transfer coefficients for various cooling technologies [5]

flow mechanics and the heat transfer mechanism in microchannels, and also no consistent explanation about the significant deviations of predictions using conventional thermo-fluid mechanics are available. However, the fundamental understanding of flow characteristics such as velocity distribution, pressure loss and heat transfer mechanism is essential in design and process control of microchannel devices. Since the heat transfer, the pressure drop and the flow regimes for small diameter channels cannot be correctly predicted using existing models and correlations for large ducts, further detailed research is needed.

In order to understand the mechanisms in microchannels experimental investigations were carried out using three different rectangular, vertically oriented channels. Single channels and not assemblies consisting of various parallel channels were chosen in order to avoid interactions between ducts. As first step single-phase experiments under adiabatic and diabatic conditions took place. These results were taken for a validation of the test rig and were used to estimate the heat loss for two-phase flow investigations (see Appendix A and B, respectively). The two-phase flow experiments were carried out to investigate pressure drop, heat transfer, flow pattern regimes and the relationship between these in order to find the best heat transfer performance conditions.

Chapter 2

Background

In this chapter a short review of experimental results on single- and two-phase flow in conventional size channels as well as in mini/microchannels is presented. In the literature experimental results obtained in channels of size ranging from some ten micrometers to few millimeters can be found. Summarising, some investigators have reported larger heat transfer and/or pressure drop than in conventional-size channels while others reported the opposite. There is no generally acceptable flow pattern map for flow boiling in minichannels. Additionally, the available empirical correlations with which the experimental results were compared are presented.

2.1 An introduction to flow in microchannels

Among the electronics cooling methods presented in Chapter 1 the flow boiling in microchannels offers a promising solution of the thermal management problem. When discussing heat transfer and the fluid behaviour in microchannels, first a definition of the term ”microchannel” should be known. Even though the research on flow boiling is going on since several years, still there is no well acceptable definition of the microchannel. The most general definition says that a channel, in which the classical theory (in terms of pressure drop and heat transfer correlation) is no longer fully applicable, is called a microchannel. The theory, in the sense of understanding physics and basic governing equations, remains the same for large and small channels. It is just so, that different effects become relevant when the geometry becomes smaller.
Kew and Cornwell [23] proposed a simple criterion for ”flow boiling in confined space”. The onset of the ”narrow channel” starts when a characteristic bubble departure size is greater than half of the hydraulic channel diameter, $Co > 0.5$. A group termed Confinement number, Co, represents the ratio of both diame-

Table 2.1: Typology of channels based on hydraulic diameter

Mehendale's typology	Kandlikar's typology
micro-scale span:	microchannel:
$1\ \mu m < d_h < 100\ \mu m$	$10\ \mu m < d_h < 200\ \mu m$
meso-scale span:	
$100\ \mu m < d_h < 1\ mm$	minichannel:
compact-scale span:	$200\ \mu m < d_h < 3\ mm$
$1\ mm < d_h < 6\ mm$	
conventional-scale span:	conventional channel:
$6\ mm < d_h$	$3\ mm < d_h$

ters.
Similar criterion can be built on the fact that in microscale the bubble growth is confined by the size of the channel and only one bubble can exist in the cross-section, opposed to the existence of multiple bubbles in a conventional-size channel ([24], Chapter 4: J.R. Thome, M. Groll and R. Mertz, Boiling and evaporation). Hence the threshold to confined bubble flow could be taken as the microscale threshold (viz. when the bubble departure diameter is larger than the channel diameter, $d_h < d_{bubble,\ depature}$). For this purpose, the bubble departure diameter can be calculated from Eq. 2.1 given by Fritz ([25] cited from [24]) for nucleate pool boiling.

$$d_{bubble,\ Fritz} = 0.0208\beta \left[\frac{\sigma}{g(\rho_l - \rho_g)}\right]^{0.5} \tag{2.1}$$

where β is a static contact angle.

For application to a wider range of pressures, this correlation has been expanded to Eq. 2.2 ([24], Chapter 4: J.R. Thome, M. Groll and R. Mertz, Boiling and evaporation).

$$d_{bubble,\ departure} = 0.0012 \left[\frac{\rho_l - \rho_g}{\rho_g}\right]^{0.9} d_{bubble,\ Fritz} \tag{2.2}$$

Mehendale et al. [26] and Kandlikar [27] proposed the hydraulic diameter as a criterion of liquid flow in the "narrow channel", Table 2.1.

The presented work deals with channels of $d_h = 0.271, 0.359$ and $0.484\ mm$. Their Confinement number (Co) in the investigated range is higher than 0.5 which defines "flow boiling in confined space". According to criteria given by Mehendale et al. and Kandlikar, the considered channels belong to meso- and mini- scale span, respectively. However according to Eq. 2.2 they can be called microchannels (considering the smallest obtained value of $d_{bubble,departure}$). In order to avoid confusion they are called "narrow channels" in this thesis.

The microchannel heat sink cooling concept was first introduced by Tuckerman and Pease in the 1980s using water as cooling fluid ([28] cited from [24]). Since this time intensive investigations have been carried out on the influence of small size on the flow and heat transfer performances. Experimental results reported in literature reviews (e. g. [29], [30], [24]) are very scattered. They indicate both higher and lower heat transfer performance and/or pressure drop than expected based on conventional/classical theory. This can be caused by parameters (e.g. roughness, axial conduction, electrokinetic effect) which in conventional size channels were neglected.

Generally, in large and narrow channels different kinds of forces are dominant, hence they cause the different flow/thermal behaviours. The forces which are proportional to the characteristic length with a higher power (e.g. gravitational, buoyancy forces) are dominant in large channels and become less important with decreasing characteristic length. Inversely, the forces which are proportional to characteristic length with a lower power (e.g. viscous force, surface tension) become more important and even dominant in narrow channels, but with increasing characteristic length they become negligible [31].

Some authors pointed out that differences occur due to the existence of an electric double layer (EDL). Mala et al. [32] found that the EDL and the streaming potential act against the liquid flow resulting in a higher apparent viscosity and in a lower heat transfer rate. The investigated separation distance was $25\ \mu m$ and the channel was $1\ mm$ long.
Yang et al. [33], based on investigations of rectangular channels with the shortest side around $20 - 40\mu m$, found that the electrokinetic effect could have significant influence on the friction factor and the Nusselt number. By means of their model they estimated the friction factor and the Nusselt number for an aqueous solution for low concentration and a wall surface of high zeta potential. The authors concluded that, for the conditions used in the evaluations of the model, the EDL effects should not be important for pressure drop and heat transfer in channels larger than $40\mu m$.
A good agreement between experimental and modelling data for adiabatic conditions was found by Ren et al. [34] using an electrokinetic flow model. Comparisons showed that the EDL and the electro-viscous effect were one significant reason for higher pressure drop in rectangular microchannels with hydraulic diameters from 27 to $58\ \mu m$ (working fluids water and low concentration KCl solution).
The analytical solution of time-dependent microfluid flow in rectangular microchannels by combining electrokinetic effect with liquid slippage was presented and summarised by Yang and Kwok [35]. Results suggested that the electrokinetic transport phenomena are very different from traditional flow. Slippage of liquid induced by surface energetic treatment can reduce the resis-

tance of microfluid flow. For pressure-driven-flow, liquid slippage counteracts the effect by the EDL and induces a larger flow rate so that the flow efficiency in microchannels can be increased. The effect of slip on flow rate depends on channel wall material, electrolyte concentration and pH. From their analysis for parallel plates, a new method to measure simultaneously the zeta potential and slip coefficient was described.

Tretheway and Meinhart [36] compared the velocity profile of water flowing in a channel with hydrophobic and hydrophilic surfaces and a hydraulic diameter of $109\ \mu m$ ($30x300\ \mu m^2$). They found that for the hydrophilic surface the measured velocity profiles agree with the solution of the Stokes equation and therefore they accepted the non-slip boundary conditions. But for the flow in hydrophobic microchannels the velocity profiles were significantly different.
Wu and Cheng [37] found that for trapezoidal microchannels ($d_h = 0.067 - 0.156\ mm$) the laminar Nusselt number and apparent friction factor increase with the increase of surface roughness and surface hydrophilic property (the hydrophilic effect was investigated in channels with hydraulic diameters up to $100\ \mu m$). A comparison of results shows that the geometric parameters have a more significant effect on the performance than the surface roughness and surface hydrophilic property.

Kenning and Yan [38] presented that for diabatic water flow in a rectangular channel with hydraulic diameter $1.3\ mm$ the compressibility of the two-phase flow has an influence on flow and pressure fluctuations but not on the heat transfer coefficient. For low inlet compressibility (a degassing procedure of working fluid had been applied), the pressure drop has been larger than for high inlet compressibility.

For conventional size channels wall thickness is usually negligibly small in comparison to inner hydraulic diameters. Therefore axial thermal conduction problems can be omitted. The lower the hydraulic diameter, the more important the coupling between wall and bulk fluid temperature becomes because the heat transfer coefficient reaches large values. In consequence, the axial conductive heat transfer in the wall has to be taken into account and the wall heat flux cannot stay uniform: heat transfer mainly occurs at the entrance of mini-microchannels [39].

The reasons for discrepancy between the microchannel flow/thermal behaviour and the macroscale theory can be much more trivial than those described above. Following difficulties of determining the experimental parameters with high enough accuracy can occur ([24] Chapter 3: B. Palm and X.F. Peng, Single-phase convective heat transfer):

- Measuring the average channel diameter with good accuracy may be

problematic. Additionally it may also vary along the channel. In laminar flow, the Nusselt number is inversely proportional to the diameter and the friction factor is proportional to the diameter by power five. This indicates a huge experimental error for a small uncertainty of diameter measurement.

- For the same channel material the relative surface roughness changes depending on the diameter. Some investigators have suggested that the surface roughness has been a cause for deviation from classical behaviour both in laminar and turbulent flow.

- Most investigations used thermocouples to measure the wall temperatures. Their accuracy could be questioned as the dimensions of the thermocouples may have the same order of magnitude as the channels themselves.

- For multichannel investigations the results may be influenced by maldistributions between the channels. For parallel channels the measurement of representative wall temperatures is especially difficult.

- The classical correlations are valid only under idealised conditions of either constant temperature or constant heat flux. These conditions may be difficult to achieve in microchannels, especially because of longitudinal thermal conduction in the channel wall.

Three aspects of flow boiling

The flow boiling investigations consist of three aspects: heat transfer, pressure drop and flow pattern. The research on this field is complicated because their effect cannot be considered separately. By means of Fig. 2.1 interactions between these can be explained as follows.

During heating under saturated condition the vapour quality increases changing the flow pattern from bubbly to slug and then to annular flow. With such change the void fraction increases simultaneously and affects the pressure drop (total pressure drop is a function of void fraction, Eq. 3.34).
In the saturated region the fluid temperature profile depends on the pressure profile. The fluid temperature, by definition of the heat transfer coefficient, influences the heat transfer.
Since the viscosity of fluid changes while heating (in case of water the dependency is quite strong) the frictional pressure drop is diminished. In consequence the total pressure drop is influenced, because the frictional term usually represents more than 50 % of the total pressure drop.

The pressure profile, apart from its obvious influence on the temperature profile, can influence the flow pattern by controlling nucleation.

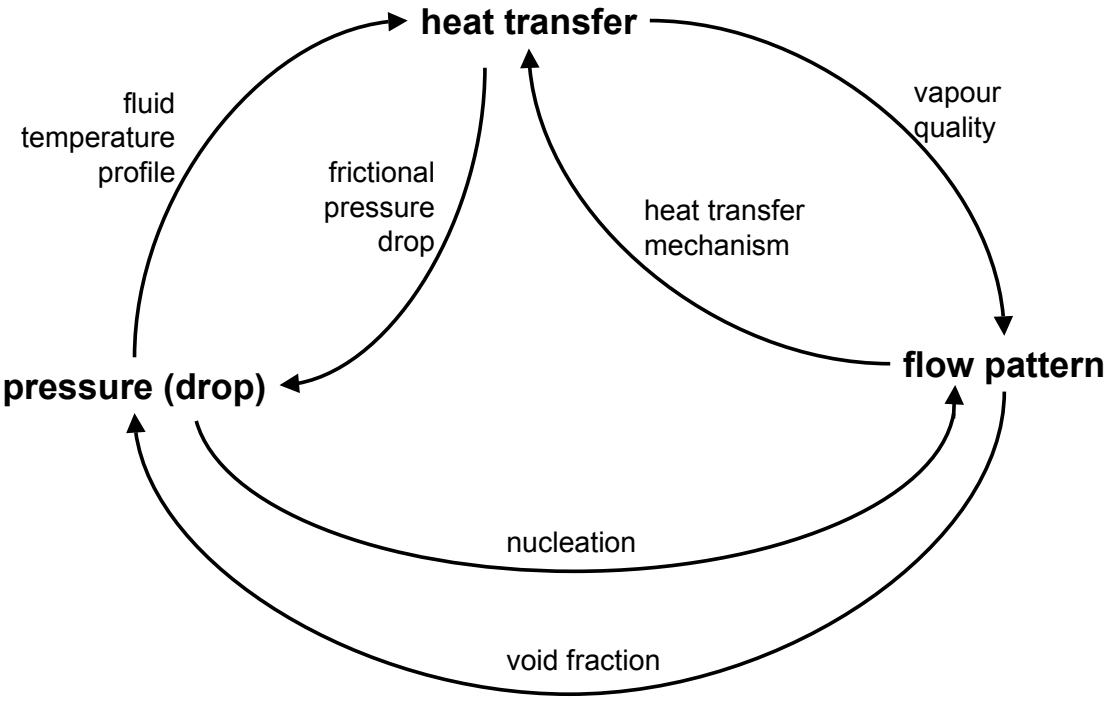

Figure 2.1: Three aspects of flow boiling and their interactions

2.2 Flow visualisation and flow pattern maps

Visualisation

Vapour and liquid flowing together in a channel can create different flow forms, called flow patterns, depending on geometry, fluid properties and flow conditions (mass and heat flux). In the diabatic case flow patterns change along the channel axis because of evaporation and vapour body agglomeration. All conditions affect void fraction (Eq. 2.3) and vapour quality [1] (Eq. 2.4) [40] and they in turn can be taken as parameters to describe flow patterns and their regimes.

$$\alpha = \frac{A_g}{A_{cs}} \tag{2.3}$$

[1] thermodynamic vapor quality x_{th} is calculated from heat balance according to Eqs. 3.40-3.43

$$x = \frac{G_g}{G} \tag{2.4}$$

With a change of the channel diameter, different forces become dominant and in consequence different flow patterns can occur at the same remaining conditions. For instance, bubbly flow in conventional size channels is a flow with small, isolated bubbles. For much smaller channel diameters bubbles reach a size close to the channel size very fast and then slug flow occurs.

One of the first flow pattern investigations in vertical tubes (2.5 *cm* diameter pipes) with an adiabatic two component system was carried out by Kozlov in 1954 [41]. First experimental results in a diabatic system were presented by Bennett et al. [42]. Experiments with water-steam systems at high pressure were undertaken under steady-state and fully developed flow conditions. In vertical conventional channels during upward two-phase flow, usually bubbly, slug, churn and annular flow occur. There can also be some mixed types like wispy-annular or mist flow. In the literature, further different flow pattern names and their definitions coexist. In multichannels with hydraulic diameter less than 1.7 *mm* Cornwell and Kew [43] found isolated bubbles, confined bubbles and annular-slug flow. Nucleate boiling with isolated bubbles, nucleate boiling with coalesced bubbles and partial dryout regimes in a narrow vertical gap were reported by Bonjour and Lallemand [44]. For air-water and steam-water flows in horizontal tubes, Feng and Serizawa [45] distinguished following flow patterns: dispersed bubbly flow, gas slug flow, liquid ring flow and liquid lump flow.

Flow pattern maps

Because the different flow patterns are determined by forces between phases, it is reasonable to use diagrams, so-called flow pattern maps, to depict the boundaries between the various flow patterns in their dependence on these forces. They give some idea of the particular pattern likely to occur for a given set of local flow parameters.
In the literature, a lot of flow pattern maps exist. The first flow pattern map for a horizontal channel was presented by Baker ([46] cited from [47]) and modified by Scott ([48], cited from [47]). Hewitt and Roberts ([49], cited from [47]) proposed one of the first flow pattern maps for vertical tubes. They distinguished bubbly, bubbly-slug, slug, churn, wispy-annular and annular flow. The investigations were undertaken on low-pressure air-water and high-pressure steam-water flows in small diameter tubes ($10 - 30$ *mm*).

On the basis of experimental results obtained from vertical pipes (diameter 20-60 *mm*) with an air-water flow and physical mechanisms proposed for each flow transition, Taitel et al. [50] proposed a flow pattern map with superficial gas and

liquid velocities. The transition boundaries separated bubbly, dispersed bubbly, slug, churn and annular flow.
The slug flow requires a process of bubble agglomeration or coalescence which happens when the void fraction is high enough (e. g. $0.25 \leqslant \alpha \leqslant 0.3$). For the calculation of the bubbly-slug transition boundary, $\alpha = 0.25$ was considered. Finally this transition boundary corresponding to the liquid superficial velocity j_l was described by Eq. 2.5.

$$j_l = 3.0 j_g - 1.15 \left(\frac{\sigma g (\rho_l - \rho_g)}{\rho_l^2} \right)^{0.25} \tag{2.5}$$

For conventional size channels annular flow cannot exist unless the gas velocity in the gas core is sufficient to lift the entrained droplets. When the gas rate is insufficient the droplets fall back, accumulate and form a bridge and churn or slug flow take place. Eq. 2.6 predicts the minimum value of the superficial gas velocity j_g needed for stable annular flow.

$$\frac{j_g \rho_g^{0.5}}{(\sigma g (\rho_l - \rho_g))^{0.25}} = 3.1 \tag{2.6}$$

A flow pattern map similar to Taitel et al.'s map, also for vertical tubes but with different transition criteria, was reported by Mishima and Ishii [51] who postulated that flow parameters such as void fraction are conceptually simpler and therefore more reliable parameters to predict flow pattern boundaries.
The Mishima-Ishii model, based on the same fundamentals as the Taitel et al.'s model, assumes a void fraction $\alpha = 0.3$ for the bubbly-slug transition boundary. With this assumption and the relationship between superficial velocities derived from the drift velocity for bubbly flow the bubbly-slug boundary was described by Eq. 2.7, [52].

$$j_l = \left(\frac{3.33}{C_0} - 1 \right) j_g - \frac{0.76}{C_0} \left(\frac{\sigma g (\rho_l - \rho_g)}{\rho_l^2} \right)^{0.25} \tag{2.7}$$

The distribution parameter C_0 for rectangular ducts was given by Eq. 2.8.

$$C_0 = 1.35 - 0.35 \sqrt{\frac{\rho_g}{\rho_l}} \tag{2.8}$$

The Mishima-Ishii model contains two criteria for the churn-annular boundary. In this thesis these criteria were used to describe the slug-annular transition. For small diameter channels, Eq. 2.9 was proposed.

$$j_g = \sqrt{\frac{g d_h (\rho_l - \rho_g)}{\rho_l}} (\alpha - 0.11) \tag{2.9}$$

For large channels, Eq. 2.10 was applicable.

$$j_g \geqslant \left(\frac{\sigma g(\rho_l - \rho_g)}{\rho_g^2} \right)^{0.25} N_{\mu l}^{-0.2} \tag{2.10}$$

The boundary for the above two cases was defined as Eq. 2.11.

$$d = \frac{\sqrt{\frac{\sigma}{g(\rho_l - \rho_g)}} N_{\mu l}^{-0.4}}{\left(\frac{1 - 0.011 C_0}{C_0} \right)^2} \tag{2.11}$$

The viscosity number $N_{\mu l}$ in Eqs. 2.10 and 2.11 can be approximately calculated with Eq. 2.12.

$$N_{\mu l} \cong \frac{\mu_l}{\left(\rho_l \sigma \sqrt{\frac{\sigma}{g(\rho_l - \rho_g)}} \right)^{0.5}} \tag{2.12}$$

For air-water flow at $20\,^{\circ}C$ and atmospheric pressure the "transition" diameter is $d \approx 58\ mm$.

Lin et al. [53] proposed flow pattern maps for vertical small tubes ($d = 1.0$ and $2.36\ mm$) with two dimensionless parameters (Confinement and Kutateladze Number) as axes.

The importance of surface tension for two-phase flow in horizontal channels was emphasised in a flow pattern map for horizontal miniature and micro tubes by Tabatabai and Faghri, [54]. The flow pattern map was compared against a number of experimental data sets (condensation of different fluids in tube diameter ranges from $15.88\ mm$ to $4.8\ mm$ and air/water flow in tube diameter ranges from $12.3\ mm$ down to $1\ mm$) totaling 1589 data points. The surface tension dominated regime refers to plug, slug and bubbly flow, particulary in tubes of small diameter. The shear-dominated regime refers to annular, mist, stratified and wavy flow. The liquid volume fraction corresponding to the bubbly/slug-annular boundary in the proposed flow pattern map was determined according to Eq. 2.13.

$$\frac{j_l}{j_l + j_g} = 0.06 \tag{2.13}$$

For diabatic horizontal flow, boiling transition boundary criteria have been proposed by Steiner ([55] cited from [56]). Because of different flow patterns compared to vertical flows, only the intermittent to annular flow transition was useful for a vertical channel. According to the authors the intermittent flow pattern occurs at a low vapour quality and unsteady flow patterns like plug and slug flow.

An intermittent-annular criterion based on the Martinelli parameter (Eq. 2.14) is proposed in reference [55] (cited from [56]).

$$X_{tt} = \left(\frac{1 - x_{th}}{x_{th}}\right)^{0.875} \left(\frac{\rho_g}{\rho_l}\right)^{0.5} \left(\frac{\mu_l}{\mu_g}\right)^{0.125} = 0.34 \tag{2.14}$$

Morgante and Fabre [57] investigated flow patterns of a nitrogen-water mixture passing through a tube and rectangular channels of millimeter size in horizontal orientation. They found two flow patterns and proposed a model to predict the transition between them. One of the distinguished patterns, intermittent flow, was characterised by the existence of long bubbles separated by liquid slugs (slug flow). The second one, separated flow, was characterised by the continuity of the gas-liquid interface (annular flow with or without waves, stratified flow). The liquid flows close to the wall whereas the gas flows in the core. From a similarity analysis, only surface tension and inertia could explain the observed transition. The transition between the intermittent flow dominated by surface tension force and separated flow dominated by inertia force occurs when the mixture Weber number is close to unity. The transition in the flow pattern map is given by Eq. 2.15.

$$\rho_l (j_l + j_g)^2 d_h = C\sigma \tag{2.15}$$

where C is a constant whose value is not too far from unity.

The *superficial velocities* (Eqs. 2.16 and 2.17) are defined as the volumetric flow rate per channel cross-sectional area for each phase. Gas and liquid superficial velocities are needed to establish flow pattern maps in order to compare flow regimes for different channel geometries.

$$j_g = \frac{\dot{V}_g}{A_{cs}} = \frac{G x_{th}}{\rho_g} \tag{2.16}$$

$$j_l = \frac{\dot{V}_l}{A_{cs}} = \frac{G(1 - x_{th})}{\rho_l} \tag{2.17}$$

2.3 Pressure drop

To approach the pressure drop for two-phase flow two basic models are usually employed: the homogeneous and the separated flow model. Either a strong assumption of equal phase velocities (homogeneous model) or additional empirical correlations of void fraction (separated model) are necessary to solve the equations.

The homogeneous model, also known as 'the friction factor' or 'fog-flow' model, considers the two phases to flow as a single phase possessing mean fluid properties. The assumptions are: equal vapour and liquid velocity, thermodynamic equilibrium of the phases and use of a suitably defined single-phase friction factor for two-phase flow. The separated flow models consider phases to be segregated into a liquid and a vapour stream. One of those was proposed by Lockhart and Martinelli [58] to estimate the adiabatic two-phase frictional pressure drop. Chisholm's method described in [59] shows the influence of the mass velocity on the two-phase friction factor. Yan and Lin [60] obtained a new empirical equation for the evaporation friction factor. In addition, they found that the measured pressure drop was higher for increased mass and heat flux.

Qu and Mudawar [21] examined ten different correlations to calculate the pressure drop for water flowing through 21 heated rectangular parallel ($0.231\ x\ 0.713\ mm^2$) channels with the hydraulic diameter of $0.349\ mm$. The authors suggested that the pressure drop in the two-phase region can be expressed as the sum of acceleration and frictional components. They checked six popular macro-channel correlations and four correlations developed especially for mini/micro-channels. The four mini/micro channels correlations are all based on the separated flow model, and employ the void fraction correlation (Eq. 2.18) of Zivi ([61] cited from [21]) to evaluate $(\Delta p_a)_{tp}$.

$$\alpha_{out} = \frac{1}{1 + \left(\frac{1-x_{th,\,out}}{x_{th,\,out}}\right)\left(\frac{\rho_g}{\rho_l}\right)^{(2/3)}} \tag{2.18}$$

Among the six macro-channel correlations one was based on homogeneous flow, while the remaining five employed the separated flow model and the Martinelli void fraction correlation (Eq. 2.19) to calculate the acceleration pressure drop $(\Delta p_a)_{tp}$.

$$\alpha = 1 - \frac{1}{\Phi_l}, \qquad \Phi_l^2 = 1 + \frac{C}{X} + \frac{1}{X^2} \tag{2.19}$$

Among all of them, the Lockhart-Martinelli correlation for laminar liquid - laminar vapour flow predicted the experimental data best (± 28.6 %). A new correlation for the C-parameter which takes into account the effects of both, channel size (d_h $[m]$) and coolant mass velocity (G $[kg/m^2 s]$), was proposed, Eq. 2.20. This model was recommended especially for heat sink designs because it provided a detailed description of various transport processes occurring in microchannels.

$$C = 21\left(1 - e^{-0.319 \cdot 10^3 d_h}\right)(0.00418G + 0.0613), \tag{2.20}$$

Wen and Kenning [62] reported diabatic pressure drop data for flow boiling of water in a vertical rectangular microchannel with a hydraulic diameter of

1.33 *mm* (width x depth = $2x1$ mm^2). The experiments were performed for mass fluxes from 57 to 211 kg/m^2s and heat fluxes from 25 to 105 kW/m^2. They pointed out that in the small channels the frictional pressure drop had a major influence on the overall pressure drop. The measured pressure drops were compared with homogeneous flow model and separated flow model calculations using the Lockhart-Martinelli method with modified C-parameter (Eq. 2.21 given by Mishima [63]), the Chisholm method and the Tran method.

$$C = 21\left(1 - e^{-0.27s}\right), \tag{2.21}$$

where s is the gap width in *mm*.

They concluded that despite a big difference between small and large channels the two-phase frictional pressure drop was well correlated by the Lockhart-Martinelli correlation with a C-value modification. The homogeneous, the Chisholm and the Tran correlations have been less rewarding. The same methods for water flowing through a microchannel with hydraulic diameter of 0.058 *mm* (width x depth = $0.050x0.070$ mm^2) have been checked by the authors. The Tran and the Chisholm methods overestimated experimental data more than ten times, whereas the homogeneous and the Lockhart-Martinelli methods overpredicted data by around 100 %. Therefore the authors concluded that none of the presented correlations could predict the pressure drop for microchannels with hydraulic diameters lower than 0.058 *mm* well.

Shuai et al. [64] presented diabatic experimental data for rectangular channels with hydraulic diameters 0.80 *mm* ($0.5x2$ mm^2) and 2.67 *mm* ($2x4$ mm^2). They found that the two-phase flow pressure drop in the small channel was much greater than in the larger one. The frictional pressure drop was compared with the Lockhart-Martinelli correlation. For both channels the experimental results have been described well by this method.

Aforementioned Kim et al. [65] compared predictions of some available correlations with results obtained for a water-air mixture flow in a test section which consisted of a horizontal header (circular tube) with hydraulic diameter of 5 *mm* and ten upward directed circular channels with hydraulic diameters of 1.5 *mm*. The mass flux and the inlet gas quality were from 50 to 200 kg/m^2s and from 0.1 to 0.3, respectively. The best agreement (average error $\pm 12\%$) with experimental data was obtained with the Friedel correlation [66].

Some authors proposed to use the modified Lockhart-Martinelli correlation. Lee and Lee [67] presented an experimental study for adiabatic water-air flow in horizontal rectangular channels with hydraulic diameter from 0.78 to 6.67 *mm*. They found that the classical Lockhart-Martinelli correlation cannot describe the experimental data properly. Therefore, the authors proposed a modification of the C-parameter (Eq. 2.22), which contains the effect of mass flux and gap size. The modified correlation predicted the pressure drop successfully for

extremely narrow channels where the effect of the surface tension force is becoming dominant.

$$C = A\chi^a\psi^b Re_{lo}^c, \tag{2.22}$$

where ψ shows the relative importance of the viscous and the surface tension effect, χ is a parameter independent of the liquid slug velocity (obtained by combination of ψ and Re_{lo}). The constant A and exponents a, b, c were determined through a data regression process.

$$\chi = \frac{\mu_l^2}{\rho_l \sigma d_h}, \qquad \psi = \frac{\mu_l u}{\sigma}.$$

Kawahara et al. [68] presented adiabatic results for gas-liquid two-phase flows through a circular microchannel with internal diameter $0.100\ mm$. In order to study the effect of liquid properties on the pressure drop, four aqueous ethanol solutions with different mass concentration were used as the working liquid, while nitrogen gas was used as the gas phase. They found that the homogeneous flow model cannot predict the experimental data. On the other hand, the Lockhart-Martinelli correlation with C-constant modification (Eq. 2.23) proposed by Mishima and Hibiki [69] can predict the presented data well.

$$C = 21\left(1 - e^{-0.319 d_h}\right) \tag{2.23}$$

All of the above mentioned investigations showed that the two-phase pressure drop sometimes can be properly predicted by the classical correlations (e. g. the Lockhart-Martinelli method, the Friedel method). Otherwise some modifications of the classical correlations have been made to extend their validity to mini- and microchannels. In Table 2.2 the accuracy (expressed by the mean absolute error - MAE) of the original Lockhart-Martinelli method (Eq. 3.17-3.30) and its modifications is presented, when they are used to predict the pressure drop for two-phase flow in mini- and microchannels.

2.4 Heat transfer

Flow boiling is complicated by the fact that, simultaneously with a change of flow patterns, different vaporisation mechanisms may be encountered at different positions along the channel, Fig. 2.2. The boiling of refrigerants in small-diameter channels can be dominated by nucleate boiling, by convective boiling, or both mechanisms. Near to the onset of boiling the nucleation mechanism usually dominates. With increasing vapour quality the flow regime undergoes a transition to annular or to nearly annular flow. Then, the film vaporisation (convective boiling) becomes a considerable heat transfer mechanism and thereafter can even completely suppress nucleate boiling. Because of vaporisation

Table 2.2: Accuracy of the Lockhart-Martinelli correlation and its modifications

author	accuracy	
	of the original Lockhart-Martinelli correlation	of the modified Lockhart-Martinelli correlation
Lee and Lee [67]	–	± 10%, Eq. 2.22
Qu and Mudawar [21]	±28.6 % lam. liquid-lam. vapour ±44.6 % lam. liquid-turb. vapour	±12.4 %, Eq. 2.20
Wen and Kenning [62]	–	±35 %, Eq. 2.21
Shuai et al. [64]	±30 %	–
Kawahara et al. [68]	–	±20 %, Eq. 2.23

(and for conventional size channels an entrainment of liquid droplets) the liquid film may disappear completely (dryout) or only at some position (partial dryout). As a result, the heat transfer coefficient increases along the channel up to onset of dryout. Because the local dry areas are relatively inactive, with decrease of the wetted wall fraction the heat transfer coefficient (average around the channel perimeter) continuously decreases [40].

In order to describe the flow boiling phenomenon many empirical correlations have been proposed. As examples of empirical equations for the two-phase heat transfer coefficient in conventional size channels, the Chen correlation [70] and the method proposed by VDI-Wärmeatlas [71] are shown. Chen assumed that the two-phase heat transfer is composed of convective and nucleate boiling mechanisms, Eq. 2.24.

$$h_{tp} = h_{tp,\,NBD} + h_{tp,\,CBD} \tag{2.24}$$

The convective component $h_{tp,\,CBD}$ is represented by Eq. 2.25. The nucleate boiling component $h_{tp,\,NBD}$ is expressed by Eq. 2.26.

$$h_{tp,\,CBD} = 0.023 \left(\frac{G(1-x_{th})d_h}{\mu_l} \right)^{0.8} \left(\frac{\mu c_p}{\lambda} \right)_l^{0.4} \left(\frac{\lambda_l}{d_h} \right) (F') \tag{2.25}$$

where

$$F' = \left(1 + \frac{1}{X_{tt}^{0.5}} \right)^{1.78}.$$

$$h_{tp,\,NBD} = 0.00122 \left(\frac{\lambda_l^{0.79} {c_{pl}}^{0.45} \rho_l^{0.49}}{\sigma^{0.5} \mu_l^{0.29} \Delta h_{lg}^{0.24} \rho_g^{0.24}} \right) \Delta T_{sat}^{0.24} \Delta p_{sat}^{0.75} (S') \tag{2.26}$$

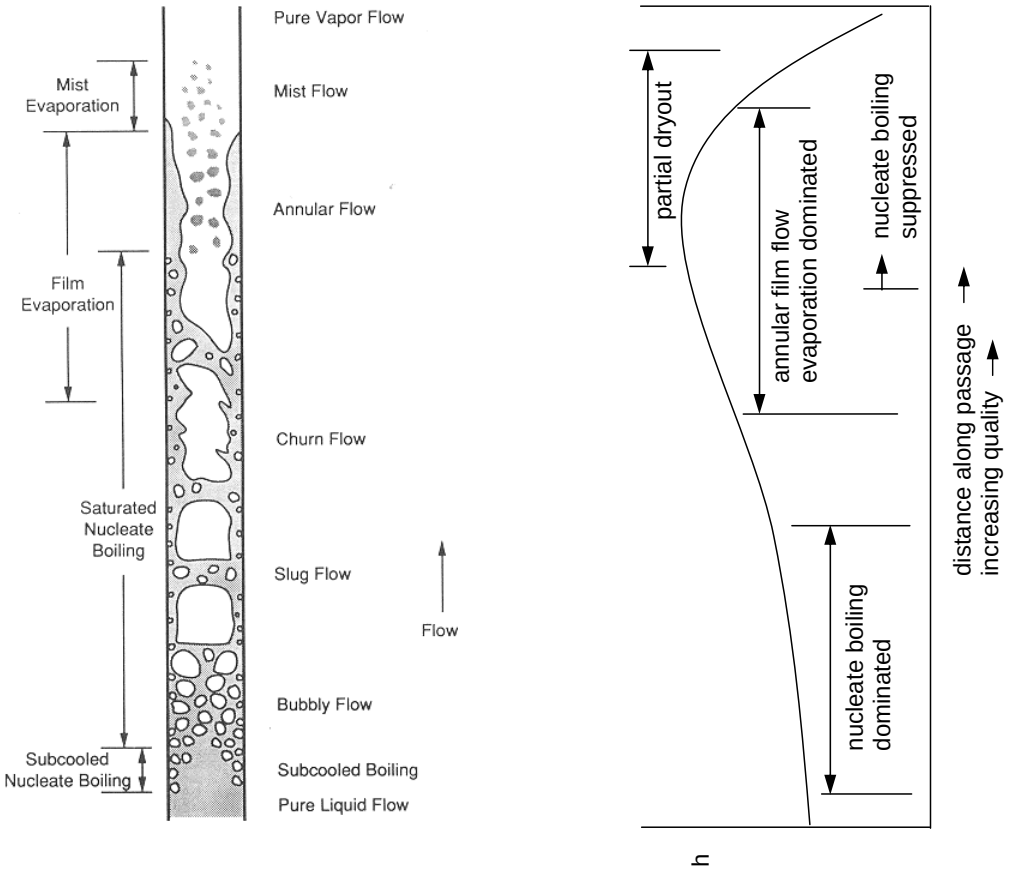

(a) flow patterns (b) heat transfer coefficient

Figure 2.2: Flow boiling in conventional size channels [40]

where

$$S' = 0.9622 - 0.5822 \left(\frac{1}{tan\left(6.18 \cdot 10^{-4} Re_{lo} \left(F'\right)^{1.25}\right)} \right).$$

For the whole thermodynamic vapour quality range Eq. 2.27, following reference [71], can be used to describe the local heat transfer coefficient under saturated conditions.

$$\frac{h(z)}{h_{lo}} = \left[(1 - x_{th})^{0.01} \left[(1 - x_{th})^{1.5} + 1.9 x_{th}^{0.6} \left(\frac{\rho_l}{\rho_g} \right)^{0.35} \right]^{-2.2} + \right.$$
$$\left. + x_{th}^{0.01} \left[\frac{h_{go}}{h_{lo}} \left(1 + 8(1 - x_{th})^{0.7} \left(\frac{\rho_l}{\rho_g} \right)^{0.67} \right) \right]^{-2} \right]^{-0.5} \quad (2.27)$$

where h_{lo} and h_{go} are the liquid and gas single-phase heat transfer coefficients, respectively.

One of the first investigations on flow boiling in narrow channels was reported by Lazarek and Black [72]. They found that at saturation conditions the heat transfer coefficient h_{tp} was independent of the vapour quality x_{th}. Hence, they concluded that the "saturated wall heat transfer process" was controlled by nucleate boiling. Based on 728 data points obtained for flow of R-113 in a round tube with an internal diameter of 3.1 *mm* and using a least squares data fitting algorithm the best agreement was found for Eq. 2.28.

$$Nu = 30Re^{0.857}Bo^{0.714} \tag{2.28}$$

Cornwell and Kew [43] found in multi-channels with hydraulic diameters smaller than 1.7 *mm* isolated bubbles, confined bubbles and annular-slug flow. For each type of flow, correlations for the heat transfer coefficient h_{tp} were developed. In contrast to Lazarek and Black [72], Wambsganss et al. [73] reported that with increasing vapour quality x_{th} the heat transfer coefficient h_{tp} decreased and was dependent also on the heat and the mass flux. Similar decreasing tendency was found by Ravigururajan [74], Warrier et al. [75], Steinke and Kandlikar [76] and Lin and Kew [77], but only for a high heat flux, and by Yen et al. [78] for vapour quality $x_{th} < 0.3$.

Kandlikar [79] suggested Eq. 2.29 which spans the whole saturated boiling range. It shows that the heat transfer mechanism varies along the channel length with the evaporation process.

$$h_{tp} = \text{larger one of} \begin{cases} h_{tp,\,NBD} \\ h_{tp,\,CBD} \end{cases} \tag{2.29}$$

For evaporation of water in vertical flows, $h_{tp,\,NBD}$ and $h_{tp,\,CBD}$ are the two-phase heat transfer coefficients in the nucleate boiling dominated and convective boiling dominated region, respectively, given by Eqs. 2.30 and 2.31 and using the single-phase heat transfer coefficient h_l of the Gnielinski correlation.

$$h_{tp,\,NBD} = 0.6683Co^{-0.2}(1-x_{th})^{0.8}h_l + 1058.0Bo^{0.7}(1-x_{th})^{0.8}h_l \tag{2.30}$$

$$h_{tp,\,CBD} = 1.136Co^{-0.9}(1-x_{th})^{0.8}h_l + 667.2Bo^{0.7}(1-x_{th})^{0.8}h_l \tag{2.31}$$

Tran et al. [80] found for flow boiling of refrigerants that nucleation dominates the flow boiling mechanism in microchannels. Yu et al. [81] and Shuai [82] observed similar tendency for water. Hence, they proposed ([80], [81], [82]) correlations as a function of the Boiling number $Bo = q/(Gh_{lg})$ and the vapour quality in order to describe the heat transfer performance in minichannels,

whereas Eq. 2.32 given by Yu et al. [81] is a modification of the Tran et al. correlation [80] for other experimental conditions.

$$h = 6.4 \cdot 10^6 (Bo^2 We_l)^{0.27} \left(\frac{\rho_l}{\rho_g}\right)^{-0.2} \tag{2.32}$$

By regression analysis of the experimental data (more than 600 points) for the two narrow channels $0.86 \times 2.0\ mm^2$ and $0.54 \times 1.60\ mm^2$ the following final correlations were determined (Eqs. 2.33 and 2.35) by Shuai [82].

For experimental data taken in the ranges: $0.002 < x_{th} < 0.55$ and $0.07 < Bo \cdot 10^4 < 7.32$ and $Re_{lo} < 2300$, Eq. 2.33 was obtained.

$$h_{tp} = 664.13 Bo^{0.7} x_{th}^{-0.297} h_{lo} \tag{2.33}$$

where h_{lo} is given by the Shah correlation [83], Eq. 2.34.

$$Nu = \begin{cases} 1.953 \left(RePr\frac{d}{L}\right)^{1/3}, & \left(RePr\frac{d}{L}\right) \geqslant 0.33 \\ 4.364 + 0.0722 \left(RePr\frac{d}{L}\right), & \left(RePr\frac{d}{L}\right) < 0.33 \end{cases} \tag{2.34}$$

For experimental data taken in the ranges: $0.002 < x_{th} < 0.03$ and $0.06 < Bo \cdot 10^4 < 0.63$ and $Re_{lo} > 2300$, Eq. 2.35 was obtained.

$$h_{tp} = 434 Bo^{0.7} x_{th}^{-0.2627} h_{lo} \tag{2.35}$$

where h_{lo} is the Dittus-Boelter-type correlation given by

$$Nu = C \cdot 0.012 (Re_{lo}^{0.87} - 280) Pr^{0.4} \tag{2.36}$$

C is 0.78 and 0.9 for the $0.86 \times 2.0\ mm^2$ and the $0.54 \times 1.60\ mm^2$ channel, respectively. The experimental data (more than 600 points) were described by the above method with a mean deviation below 20 %.

Warrier et al. [75] proposed correlations for subcooled and saturated boiling regimes. Single-phase forced convection and subcooled and saturated nucleate boiling experiments have been performed in a small rectangular channel with hydraulic diameter of $0.75\ mm$ using FC-84 as test fluid. The maximum difference between the experimental data under saturated condition and the proposed correlation (Eq. 2.37) was ± 28 %.

$$h_{tp} = (1 + 6.0 Bo^{1/16} - 5.3(1 - 855 Bo) x_{th}^{0.65}) h_{sp} \tag{2.37}$$

In the literature further information about the influence of heat flux ([77], [78]) or mass flux [74] or both ([77], [75]) can be found.

Diaz at al. [84] investigated the flow boiling of water and hydrocarbons (n-hexane, n-heptane, n-octane and a mixture n-hexane/n-heptane) in a circular

tube ($d = 1.5\ mm$) and rectangular channels (height=$0.3 - 0.7\ mm$, width=$10\ mm$). For pure hydrocarbons it was observed that the heat transfer coefficient had a maximum value in the initial region, what can suggest a dominance of nucleate boiling. Then, with increasing vapour quality along the channel axis the heat transfer coefficient decreased. This behaviour was explained by "steam-influenced boiling" characterised by increasing partial dryout. However, for water and a mixture, after an initial region with locally dominating nucleate boiling, an increase of heat transfer coefficient with increasing vapour quality was observed. Such increase is typical for convective boiling. The same tendency was observed by Lin et al. [85] for water in a tube with hydraulic diameter $1.1\ mm$, but only for moderate heat fluxes. For heat fluxes grater than $\approx 60\ kW/m^2$, the heat transfer coefficient decreased with quality throughout the range. Authors suggested that nucleate boiling was dominant at these heat fluxes.

Agostini and Bontemps [22] investigated flow boiling of R134a in multi-port extruded tube composed of eleven parallel rectangular channels ($d_h = 2.01\ mm$) for limited mass flux ($G < 295\ kg/m^2s$) and heat flux ($q < 31.6\ W/m^2$). They observed a weak influence of vapour quality on heat transfer coefficient for $Bo \geqslant 4.3 \cdot 10^{-4}$ and $x \leqslant 0.4$. Thus the nucleate boiling regime governed this region. For the same Boiling number but vapour quality higher than 0.4 the heat transfer coefficient decreased. This suggested that partial dryout occurred because of slug/bubble confinement thinning the liquid layer thickness at the tube wall. For $Bo \leqslant 4.3 \cdot 10^{-4}$ the heat transfer coefficient was weakly dependent on vapour quality up to a transition value. Then, it started to increase. This behaviour may correspond to a competition between convection boiling and a dryout regime where partial dryout and regeneration of the liquid layer occurs. Based on these observations, the transition from nucleate boiling to supposed convective boiling occurred for $Bo(1-x) \approx 2.2 \cdot 10^{-4}$ regardless of the heat and mass flux.

A nice review of the thermal behaviour of refrigerants boiling in small channels ($d_h = 0.51$ - $3.69\ mm$) was presented by Vlasie at al. [86] which can be briefly summarised as follows:

- Three flow pattern names are commonly used: isolated bubble, confined bubble and annular flow.
- The boiling of refrigerants in small-diameter channels can be dominated by nucleate boiling, by convective boiling, or both mechanisms.
- The boundary between nucleate and convective boiling as a function of the wall superheat was proposed by Tran et al. [80] as follows. The convective heat transfer region is likely to occur at low wall superheats, with a heat transfer coefficient independent of heat flux, and increasing with

vapour quality and mass flux. The nucleate boiling region occurs at high wall superheats, with a heat transfer coefficient depending on heat flux and independent on vapour quality and mass flux. In spite of same limitations (e. g. the operating pressure, the fluid critical pressure) the above classification appears to be successful in reconciling the different trends observed by various researchers.

– Most of the time, correlations based on the nucleate boiling mechanism work satisfactorily for boiling of pure fluids in small diameter channels.

It can be summarised that till now no well-accepted correlations exist for boiling heat transfer in narrow channels. Therefore, the experimental results of this thesis will be compared also with correlations for normal-size channels.

Chapter 3

Data evaluation

During the experiments the temperature (wall and fluid) and the pressure (absolute at the inlet and outlet and differential) were measured to describe in some range the flow and heat transfer phenomena. The aim of this chapter is to show the transformation from raw data to the final experimental results.

3.1 General calculations

Characteristic length of flow

For fluid flow in a pipe its inner diameter is the characteristic length. For a turbulent flow in a non-circular duct, the hydraulic diameter is an appropriate approximation of the characteristic length (whereas for laminar flow the approximation is less accurate, particulary with cross-sections characterized by sharp corners). This allows to compare experimental and numerical data obtained for different geometries. The hydraulic diameter of a rectangular channel is described by Eq. 3.1, [87].

$$d_h = \frac{4A_{cs}}{P} = \frac{4wh}{2(w+h)} \tag{3.1}$$

In the presented investigation an asymmetrical heating condition was applied. Since heat was transported to the fluid only via three channel walls (see Chapter 4), the wetted perimeter P changes into the heated perimeter S and in consequence the hydraulic diameter is redefined.

$$d_{h,\,thermal} = \frac{4A_{cs}}{S} = \frac{4wh}{w+2h} \tag{3.2}$$

A partial-peripheral heating causes non symmetrical velocities and fluid fields. Hence the thermal and flow phenomena are expected to be different in comparison to the symmetrical heating case. In one of the few publications dealing with asymmetrical heating it was pointed out that for fully developed turbulent flow the Nusselt number was approximately 10 % below predictions for a uniformly heated circular channel of the same hydraulic diameter. The investigations were carried out for upward flow in rectangular channels with channel spacings of 2.0, 1.0, and 0.5 *mm* and aspect ratios of 1 : 10, 1 : 20, and 1 : 40. One side was uniformly heated and the remaining sides were approximately adiabatic [88].
Since to calculate heat transfer coefficients the assumed mean bulk fluid temperature was used and it makes more sense to consider friction on all walls, the first definition of the hydraulic diameter (Eq. 3.1) was chosen to describe the investigated channels. An eventual use of the "thermal"-hydraulic diameter (Eq. 3.2) probably could lead to changes of about 10 % in the results (like in reference [88]) and this would be within the error range. Therefore it should be kept in mind that, **the first definition of the hydraulic diameter (Eq. 3.1) is used in this thesis for all kinds of calculations.**

3.2 Visualisation and flow patterns

At every thermocouple position[1] along the channel axis two-phase flow was vizualised using a high-speed video system. Because of the design of the test section only a two-dimensional visualisation was possible, Fig. 3.1. The length of the channel portion inside the view window was calculated from the real channel width (in this case length of the view window equals approximately 3 *mm*). The recording time and frequency were given in the description on the right hand side of the view window.

Basic flow patterns

As mentioned in Chapter 2.2 in the literature review different flow pattern names and their definitions can be found. In order to avoid a confusion in the following discussions three basic flow patterns were distinguished, viz. bubbly flow, slug flow and annular flow. A way to estimate the vapour body length, which is a major parameter in defining the flow pattern, is described later in this chapter. Because of the design of the test section only a two-dimensional visualisation was possible. Hence, some assumptions related to the third dimension had to be

[1] for the 0.359 mm channel only at seven positions (position of the fourth thermocouple was covered by an outer frame)

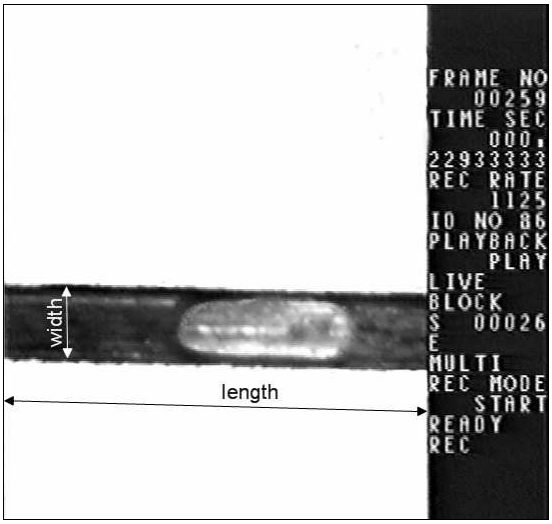

Figure 3.1: Original picture from digital high speed camera

made. It must be pointed out that the depths of the channels ($h = 0.255,\ 0.266$ and $0.346mm$) are smaller than their widths ($w = 0.289,\ 0.550$ and $0.807mm$).

Three different kinds of vapour bodies were observed. In the first category there are spherical bubbles with diameters smaller than the channel depth (Fig. 3.2a). The second category shows vapour bodies with diameters between the width and the depth which seem to be spherical, but in fact they have an elliptical cross section (Fig. 3.2b). Vapour bodies with a length larger than the width of channel belong to the third category. These slugs fill almost the whole cross-section of the channel (Fig. 3.2c).

If there was a majority of vapour bodies of the first and the second category then it was called bubbly flow. For slug flow, Taylor bubbles were typical. The diameters of these bubbles were close to the channel diameter, and they had a round front-side and usually a flat back-side shape. They belong to the third category. For annular flow, the gas phase is in the channel core, and the liquid phase flows along the wall. For the present investigations a typical annular flow was not observed. There were always some liquid bridges which interrupted the annular flow. Such type of flow can be treated as a flow with very long slugs (third category). Hence, the differentiation between slug and annular flow was introduced on the basis of slug lengths, i.e. a flow with slugs longer than fifty times the channel width was called annular flow, this will be explained in Chapter 5.1.

In Table 3.1 the classification of vapour bodies in the channels is presented. Note, all slugs were divided into three groups with different lengths. Flow with slugs longer than fifty times the width of the channel was defined as annular flow.

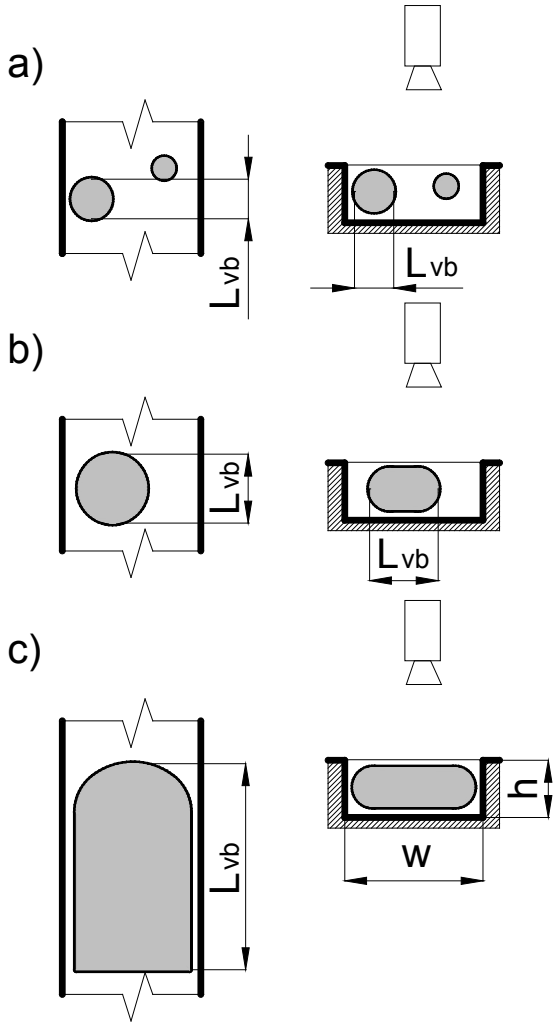

Figure 3.2: Classification of observed vapour bodies into three categories

Table 3.1: Classification of vapour bodies in the channels

vapour body length [mm]	$d_h = 0.271$ [mm]	$d_h = 0.359$ [mm]	$d_h = 0.484$ [mm]	liquid-vapour formation	defined flow pattern
depth 1 x width	0.255 0.289	0.266 0.550	0.346 0.807	bubble	bubbly
10 x width 50 x width	2.89 14.45	5.50 27.50	8.07 40.35	slug	slug
100 x width	28.90	55.00	80.70		annular

It should be mentioned that there were hardly image sequences containing only vapour bodies of one category. Hence, in order to define flow patterns and to confirm the visual observations, histograms of the vapour body length were established by means of image analysis.

Velocity and length of vapour body and liquid plug

For every vapour body passing the view window four points in time were detected (Fig. 3.3):

a) when the vapour body top crossed the right hand edge of the view window, t_1,

b) when the vapour body top crossed the left hand edge of the view window, t_2,

c) when the vapour body bottom crossed the right hand edge of the view window, t_3,

d) when the vapour body bottom crossed the left hand edge of the view window, t_4.

The velocity of a vapour body was calculated as the length of the channel portion inside the view window divided by the time required for the vapour-liquid interface to pass through it. Considering flow direction, the velocities of the top and bottom of the vapour body were calculated by Eqs. 3.3 and 3.4, respectively. The vapour body mean velocity $\overline{u}$ was calculated as the arithmetic average of these two values.

$$u_{top} = \frac{L_{vw}}{t_2 - t_1} \tag{3.3}$$

$$u_{bottom} = \frac{L_{vw}}{t_4 - t_3} \tag{3.4}$$

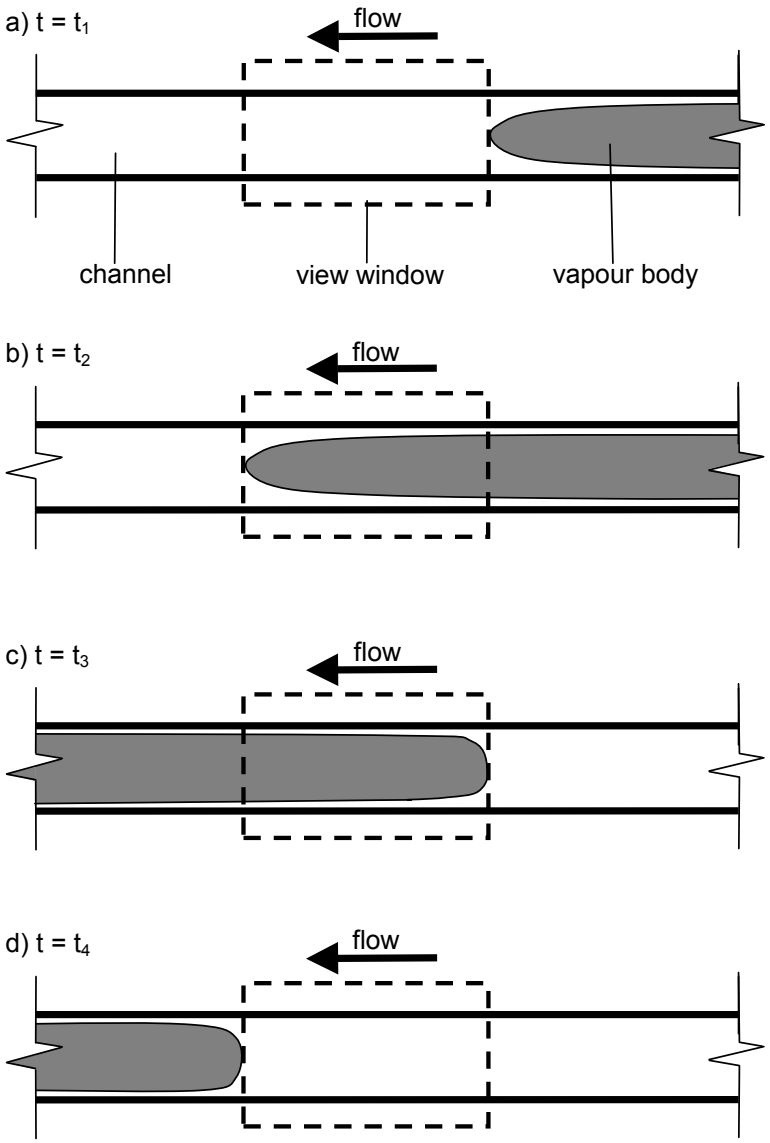

Figure 3.3: Calculation of vapour body velocity

For most cases the vapour body was longer than the view window length, therefore it's length could not be calculated directly from visualisation. Using the average vapour body velocity and the time while a certain position (right/left hand edge of view window) was crossed first by the front and further by the bottom interface, the vapour body length was calculated (Eqs. 3.5-3.7). The liquid plug velocities and lengths were calculated in an analogue way.

$$L_{vb,\ right} = \overline{u}(t_3 - t_1) \tag{3.5}$$

$$L_{vb,\ left} = \overline{u}(t_4 - t_2) \tag{3.6}$$

$$L_{vb} = 0.5(L_{vb,\ right} + L_{vb,\ left}) \tag{3.7}$$

Assuming a third dimension and a very thin liquid layer between vapour and wall (important for slugs) a vapour body volume could be estimated. For the first (Fig. 3.2a) and second (Fig. 3.2b) category these values were calculated as volume of a sphere (Eq. 3.8) and of an ellipsoid (Eq. 3.9), respectively.

$$V = \frac{\pi L_{vb}^3}{6} \tag{3.8}$$

$$V = \frac{4}{3}\pi\frac{h}{2}\frac{L_{vb}}{2}\frac{L_{vb}}{2} \tag{3.9}$$

The vapour body volume for the third category (Fig. 3.2c) was calculated as an elliptical cross-sectional area multiplied by the vapour body length, Eq. 3.10.

$$V = \pi\frac{h}{2}\frac{w}{2}L_{vb} \tag{3.10}$$

Experimental void fraction

Void fraction, per definition, is the ratio between an area occupied by vapour and the total cross section area, Eq. 2.3. The area occupied by vapour changed with time and position. Summarising volumes of vapour bodies observed during a record and dividing these values by the "total length of flow" (summarised lengths of observed vapour slugs and liquid plugs) an area occupied by vapour could be approximated, Eq. 3.11.

$$A_g = \frac{\sum V_{vapour\ body}}{L_{total}} \tag{3.11}$$

Flow pattern maps

Three different flow pattern maps were generated based on experimental visualised data. The one with superficial gas/liquid velocities as co-ordinates had to be limited to samples obtained under saturated conditions. For the subcooling range (negative thermodynamic vapour quality, Eqs. 3.42 and 3.43) the superficial gas velocity would be negative (Eq. 2.16) which is physically meaningless. The whole set of data (280 points) is presented in two further ways. First, mass flux versus thermodynamic vapour quality. The second one was proposed by Tabatabai and Faghri [54] and emphasises the importance of surface tension in small size channels.
Some of flow pattern transition boundaries proposed by different authors are described in Chapter 2.2.

3.3 Pressure drop

As already discussed, flow boiling offers a very good solution for thermal management problems, however, at the cost of a high pressure drop. Therefore an estimation of the required inlet pressure is essential for the design and optimisation of a cooling device. An algorithm to predict the pressure profile in the investigated channels with consideration of single- and two-phase pressure drop is described below.

The governing equations for steady-state one dimensional two-phase flow are: the conservation of mass (Eq. 3.12), energy (Eq. 3.13) and momentum (Eq. 3.14).

$$\dot{m}_g + \dot{m}_l = \dot{m} \tag{3.12}$$

$$\frac{d}{dz}\left(\dot{m}_g i_g + \dot{m}_l i_l\right) + \frac{d}{dz}\left(\frac{\dot{m}_g u_g^2}{2} + \frac{\dot{m}_l u_l^2}{2}\right) + \left(\dot{m}_g + \dot{m}_l\right) g cos\Theta = \frac{dQ}{dz} \tag{3.13}$$

$$\frac{dp}{dz} + \frac{P}{A}\tau_w + \frac{d}{Adz}\left(\dot{m}_g u_g + \dot{m}_l u_l\right) + [\alpha\rho_g + (1-\alpha)\rho_l] g cos\Theta = 0 \tag{3.14}$$

Since investigated channels were installed in the vertical position ($\Theta = 0$), the term $cos\Theta$ is omitted in further part of this work.

The momentum equation is often written as an equation for the total pressure gradient. Three components can be distinguished: friction, acceleration and gravity pressure drop.

$$\left(\frac{dp}{dz}\right) = \left(\frac{dp}{dz}\right)_F + \left(\frac{dp}{dz}\right)_A + \left(\frac{dp}{dz}\right)_G \tag{3.15}$$

The pressure drop along the channel was calculated as the sum of the single-phase and the two-phase pressure drop.

For single-phase flow the pressure drop was calculated by

$$\frac{dp}{dz} = -\frac{2f_{sp}G^2}{d_h\rho} - G^2\frac{d\nu}{dz} - g\rho \tag{3.16}$$

where f_{sp} is the single-phase friction factor.

The length of the single-phase region is the length of the tube where the fluid is heated up to saturation temperature corresponding to the local absolute pressure inside the tube. The saturation condition of the single-phase flow region was used as the inlet condition of the subsequent two-phase flow region.

To determine the two-phase pressure drop the separated flow model was applied. In the separated flow model different velocities have to be taken into account. The acceleration and gravitational terms require the knowledge of the void fraction which is very difficult to measure. To solve this problem, usually correlations of Lockhart-Martinelli, Martinelli-Nelson, the drift flux model or other models can be used.

In the present case, the two-phase frictional pressure gradient was calculated using the standard Lockhart-Martinelli method. This method assumes that the integral effect of the two-phases is a function of each individual single-phase pressure drop in the channel. The frictional component of the pressure drop can be described as:

$$-\left(\frac{dp}{dz}\right)_F = -\left(\frac{dp}{dz}\right)_{F,\,l}\phi_l^2 = \left(\frac{2f_l(1-x_{th})^2G^2\nu_l}{d_h}\right)\phi_l^2 \tag{3.17}$$

or it can be also expressed in terms of the single-phase frictional pressure gradient for the "liquid only" phase which is considered to flow solely in the channel.

$$-\left(\frac{dp}{dz}\right)_F = -\left(\frac{dp}{dz}\right)_{F,\,lo}\phi_{lo}^2 = \left(\frac{2f_{lo}G^2\nu_l}{d_h}\right)\phi_{lo}^2 \tag{3.18}$$

The two-phase multipliers of Eqs. 3.17 and 3.18 are related by

$$\phi_{lo}^2 = \phi_l^2(1-x_{th})^2\frac{f_l}{f_{lo}} \tag{3.19}$$

where the single-phase friction factors are expressed as follows.

$$f_l = B_l Re_l^{-n_l} \qquad \text{and} \qquad f_{lo} = B_{lo}Re_{lo}^{-n_{lo}} \tag{3.20}$$

$$Re_l = \frac{G(1-x_{th})d_h}{\mu_l} \qquad \text{and} \qquad Re_{lo} = \frac{Gd_h}{\mu_l} \tag{3.21}$$

with the constants

$B_l = 16, \quad B_{lo} = 16, \quad n_l = 1, \quad n_{lo} = 1, \quad \text{for } Re < 2300$
$B_l = 0.079, \quad B_{lo} = 0.079, \quad n_l = 0.25, \quad n_{lo} = 0.25, \quad \text{for } Re \geqslant 2300$

The two-phase friction multiplier Φ_l^2 is correlated by a function of the Lockhart-Martinelli parameter X.

$$X^2 = \frac{\left(\frac{dp}{dz}\right)_{F,\,l}}{\left(\frac{dp}{dz}\right)_{F,\,g}} \tag{3.22}$$

The individual pressure gradients for each fluid phase flowing alone in the channel are calculated with the following equations:

$$\left(\frac{dp}{dz}\right)_{F,\,l} = -\frac{2 f_l G^2 (1 - x_{th})^2 \nu_l}{d_h} \tag{3.23}$$

$$\left(\frac{dp}{dz}\right)_{F,\,g} = -\frac{2 f_g G^2 x_{th}^2 \nu_g}{d_h} \tag{3.24}$$

$$f_l = B_l Re_l^{-n_l} \quad \text{and} \quad f_g = B_g Re_g^{-n_g} \tag{3.25}$$

$$Re_l = \frac{G(1 - x_{th}) d_h}{\mu_l} \quad \text{and} \quad Re_g = \frac{G x_{th} d_h}{\mu_g} \tag{3.26}$$

with the constants:

$B_l = 16, \quad B_g = 16, \quad n_l = 1, \quad n_g = 1, \quad \text{for } Re < 2300$
$B_l = 0.079, \quad B_g = 0.079, \quad n_l = 0.25, \quad n_g = 0.25, \quad \text{for } Re \geqslant 2300$

Substituting Eqs. 3.23 and 3.24 into Eq. 3.22 the Lockhart-Martinelli parameter is defined by Eq. 3.27.

$$X^2 = \left(\frac{1 - x_{th}}{x_{th}}\right)^{2-n} \left(\frac{\rho_g}{\rho_l}\right) \left(\frac{\mu_l}{\mu_g}\right)^n \tag{3.27}$$

For the case when both the liquid and the vapour are turbulent the exponent $n = 0.25$ and Eq. 3.28 is obtained.

$$X_{tt} = \left(\frac{1 - x_{th}}{x_{th}}\right)^{0.875} \left(\frac{\rho_g}{\rho_l}\right)^{0.5} \left(\frac{\mu_l}{\mu_g}\right)^{0.125} \tag{3.28}$$

Table 3.2: Constant C for different flow regimes

liquid	gas	C
turbulent	turbulent	20
laminar	turbulent	12
turbulent	laminar	10
laminar	laminar	5

The two-phase friction multiplier Φ^2 is calculated from the frictional pressure gradient for each fluid phase flowing alone in the channel using the following equations.

$$\Phi_l^2 = 1 + \frac{C}{X} + \frac{1}{X^2} \tag{3.29}$$

$$\Phi_g^2 = 1 + CX + X^2 \tag{3.30}$$

where the constant C has different values for different flow regimes. The values are presented in Table 3.2.

The acceleration pressure drop is given by

$$-\left(\frac{dp}{dz}\right)_A = G^2 \frac{d}{dz}\left(\frac{x_{th}^2 \nu_g}{\alpha} + \frac{(1-x_{th})^2 \nu_l}{1-\alpha}\right) \tag{3.31}$$

whereas the gravitational pressure component is given by

$$-\left(\frac{dp}{dz}\right)_G = g(\alpha\rho_g + (1-\alpha)\rho_l) \tag{3.32}$$

Differentiating Eq. 3.31 and neglecting the liquid compressibility leads to

$$\begin{aligned} -\left(\frac{dp}{dz}\right)_A = \; & G^2\left(\frac{dx_{th}}{dz}\left(\frac{2x_{th}\nu_g}{\alpha} + \frac{2(1-x_{th})\nu_l}{1-\alpha}\right) + \right. \\ & \left. + \frac{d\alpha}{dz}\left(\frac{(1-x_{th})^2\nu_l}{(1-\alpha)^2} - \frac{x_{th}^2\nu_g}{\alpha^2}\right) + \frac{x_{th}^2}{\alpha}\frac{d\nu_g}{dp}\left(\frac{dp}{dz}\right)\right) \end{aligned} \tag{3.33}$$

Substituting Eqs. 3.18, 3.32 and 3.33 into Eq. 3.15, the total pressure gradient is represented as

$$\left(\frac{dp}{dz}\right) = \frac{\left(\frac{dp}{dz}\right)_F - G^2\left(\frac{dx_{th}}{dz}\left(\frac{2x_{th}\nu_g}{\alpha} + \frac{2(1-x_{th})\nu_l}{1-\alpha}\right) + \frac{d\alpha}{dz}\left(\frac{(1-x_{th})^2\nu_l}{(1-\alpha)^2} - \frac{x_{th}^2\nu_g}{\alpha^2}\right)\right) + \left(\frac{dp}{dz}\right)_G}{1 + \frac{G^2 x_{th}^2}{\alpha}\frac{d\nu_g}{dp}}$$

(3.34)

From Eq. 3.34 it can be seen that the void fraction is required to calculate the pressure gradient. The available empirical correlation to predict the void fraction in its general form is

$$\alpha = \left(1 + C_1 \left(\frac{1 - x_{th}}{x_{th}}\right)^{n_1} \left(\frac{\rho_g}{\rho_l}\right)^{n_2} \left(\frac{\mu_l}{\mu_g}\right)^{n_3}\right)^{-1} \tag{3.35}$$

where values of constants C_1, n_1, n_2 and n_3 proposed by different authors are given in Table 3.3 [89].

Table 3.3: Constants C_1, n_1, n_2 and n_3 for empirical void-fraction-correlations

correlation	C_1	n_1	n_2	n_3
homogeneous model	1	1	1	0
Lockhart-Martinelli model	0.28	0.64	0.36	0.07
Zivi model	1	1	0.67	0
Thom model	1	1	0.89	0.18
Baroczy model	1	0.74	0.65	0.13

The calculations were performed by means of a computer program MATLAB 7.0. To proceed to numerical simulations of pressure drop the following initial conditions are required.

- hydraulic diameter of the channel,
- total length of the channel,
- inclination of the channel to the vertical line,
- temperature and pressure of working fluid at the inlet,
- mass flow rate of the fluid,
- heat input.

It should be pointed out that the used program is able to check the type of the flow (single- or two-phase flow) along the channel axis for given working conditions as well as a start position of the two-phase range (the shortened algorithm of the used program is shown in Appendix D). Hence, it was also used to predict the single-phase pressure drop (see Appendix A).

3.4 Heat transfer

Under diabatic conditions the heat loss was mainly caused by the convective heat transfer from the test section to the environment. To determine the heat loss Q_{loss}, an energy balance for single-phase flow has been used (Eq. 3.36) and further the heat loss was evaluated as a function of the average wall temperature (Appendix B).

$$Q = GA_{cs}c_p\left(T_{l,\,out} - T_{l,\,in}\right) + Q_{loss} \tag{3.36}$$

The effective heat flux for the single- and two-phase flow can be defined as Eq. 3.37.

$$q = \frac{Q - Q_{loss}}{A_{ht}} \tag{3.37}$$

On the basis of the effective heat flux the local heat transfer coefficient for flow boiling as well as for single-phase flow is calculated, Eq. 3.38.

$$q = h\left(T_w(z) - T_l(z)\right) \tag{3.38}$$

The required local wall temperature was measured at eight positions and corrected considering the distance between thermocouple and channel wall. Since the fluid temperature was measured only at the channel inlet and the channel outlet some assumptions had to be made. By means of Fig. 3.4 the way to calculate the fluid temperature profile is explained as follows.

Due to the high pressure drop between the inlet and the outlet of a microchannel during flow boiling, the change of the fluid pressure and the corresponding fluid saturation temperature along the channel can not be neglected. The length Z_{sat} from the channel inlet to the position where saturation conditions are reached, was calculated by the following heat balance.

$$GA_{cs}c_p\left(T_{l,\,sat} - T_{l,\,in}\right) = qSZ_{sat} \tag{3.39}$$

From former investigations it is well known that the two-phase flow starts already under subcooled flow conditions. Therefore, flow visualisation was used to define the position Z_{ONB} of the onset of nucleate boiling. The pressure drops of the single-phase flow length were calculated by the Darcy-Weisbach equation [90] and after subtraction from the inlet pressure these results were used as the pressures at the positions Z_{sat} and Z_{ONB}, respectively. The two dash-dotted lines in Fig. 3.4 show the possible two-phase pressure profiles (the linear pressure drop was assumed), when the two-phase flow pressure drop starts at Z_{sat} and at Z_{ONB}, respectively (pressure drop under subcooled conditions was also handled as a two-phase pressure drop). The mean values

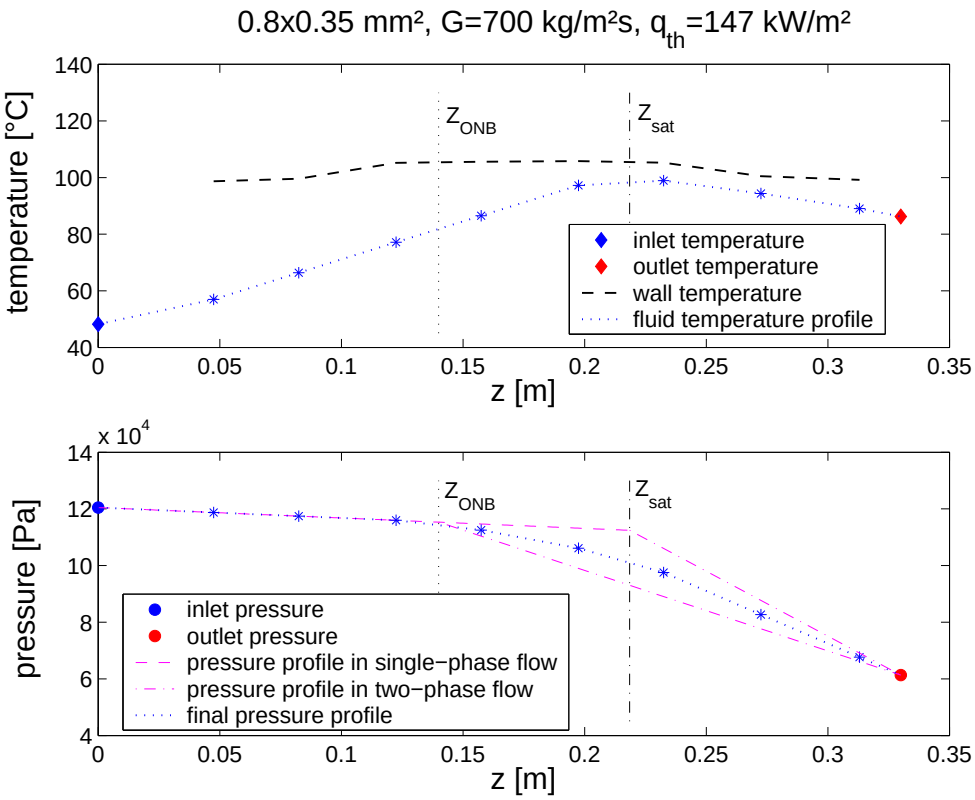

Figure 3.4: Temperature and pressure profile along the 0.484 *mm* channel length for $G = 700 kg/m^2 s$ and $q = 147 kW/m^2$

between these two profiles were taken as the final pressure profile of the two-phase flow regime. Thus, the pressure and the fluid saturation temperature T_{sat} could be determined as a function of the position z along the channel axis. The specific enthalpy of liquid and vapour for the saturation pressures $p(z)$ are known. Based on the energy balance and the conservation of mass, the thermodynamic vapour quality x_{th} at a cross section at position z can be calculated. Equations 3.40 to 3.43 describe the liquid temperature T_l and thermodynamic vapour quality x_{th} under unsaturated and saturated conditions.

$$T_l(z) = T_{l,\,in} + \frac{qSz}{GA_{cs}c_p} \qquad z < Z_{sat} \tag{3.40}$$

$$T_l(z) = T_{sat}(p(z)) \qquad z \geq Z_{sat} \tag{3.41}$$

$$x_{th}(z) = \frac{i_l(z) - i_{l,\,sat}}{\Delta h_{lg}} \qquad z < Z_{sat} \tag{3.42}$$

$$x_{th}(z) = \frac{1}{\Delta h_{lg}} \left(\frac{qSz}{GA_{cs}} + i_{l,\,in} - i_{l,\,sat} \right) \qquad z \geq Z_{sat} \tag{3.43}$$

Chapter 4

Experimental set-up and experimental conditions

This chapter comprises the descriptions of test-rig, measurement methods, experimental conditions and procedure.

4.1 The experimental set-up

The schematic of the experimental set-up used for investigation of thermo-fluid-dynamic phenomena in vertical microchannels is shown in Fig. 4.1. The main components of the closed flow loop are the fluid tank, the pump, the test section and the condenser. The flowmeter and the pre-heater are embedded in the pump. The working fluid (de-ionised water) was heated in the fluid tank and afterwards in the pre-heater where it was brought up to the channel inlet temperature. Then it was pumped through the channel of the test specimen where it was heated via three channel walls and partly evaporated. The two-phase mixture was condensed in the condenser and then flowed back to the fluid tank.

The test section (Fig. 4.2) consists of two main parts: four heater-blocks and the test specimen with the rectangular channel, both made from copper. The flowing water in the channel was heated electrically by the heater-blocks on the back side of the test section. Compared to the channel size, the heater-blocks had a huge heat capacity. Thus it was reasonable to assume that the heat flux on the test specimen was constant along the channel.

Single rectangular channels with hydraulic diameters less than $0.5\ mm$ were machined by conventional milling into the upper surface of copper plates, Fig. 4.3. All channels had the same length, $330\ mm$, of which $300\ mm$ were heated.

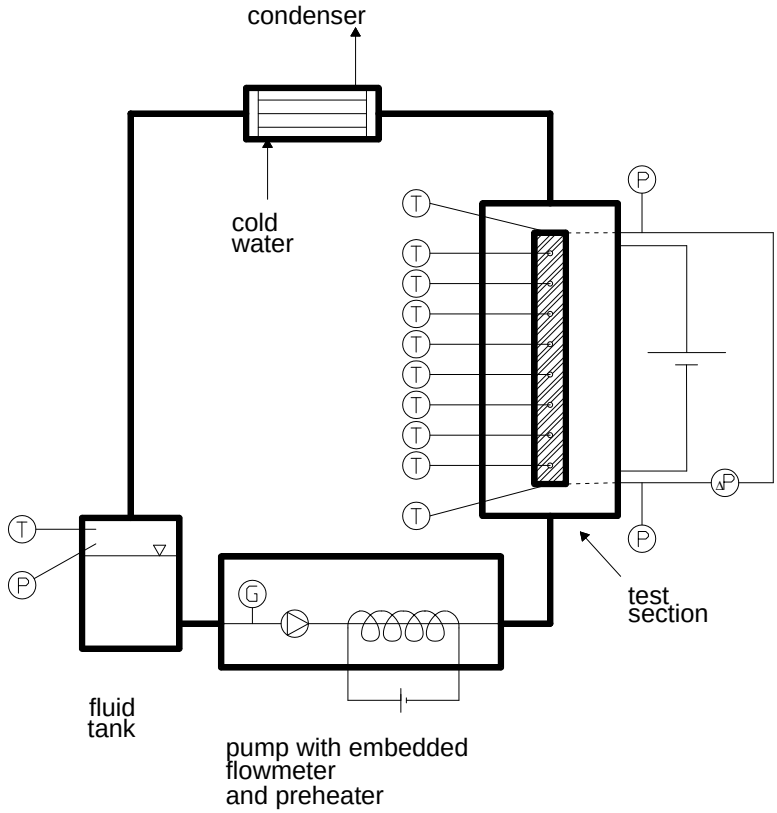

Figure 4.1: Schematic of set-up

Other geometrical data are given in Table 4.1. In the literature the importance of surface roughness on the flow in microchannels is pointed out. Therefore, some notice should be made about it. The surface roughness (R_a) of the investigated channels was below $1\ \mu m$. Since the relative surface roughness (R_a/d_h) was below 0.5 %, the roughness effect could be neglected under the considered conditions. The measurements of surface roughness and channel height were made by electron microscope at ENEA[1]. Exemplary results are shown in Appendix H.

Table 4.1: The geometry of the channels

width $[mm]$	height $[mm]$	d_h, hydraulic diameter $[mm]$	aspect ratio $[-]$	cross-sectional area $[mm^2]$	heated area $[mm^2]$
0.289	0.255	0.271	0.88	0.074	239.68
0.550	0.266	0.359	0.48	0.146	324.57
0.807	0.346	0.484	0.43	0.279	449.66

[1] Ente per le Nuove Technologie, l'Energie e l'Ambiente Sezione, Istituto di Termofluidodinamica Energetica, Rome, Italy

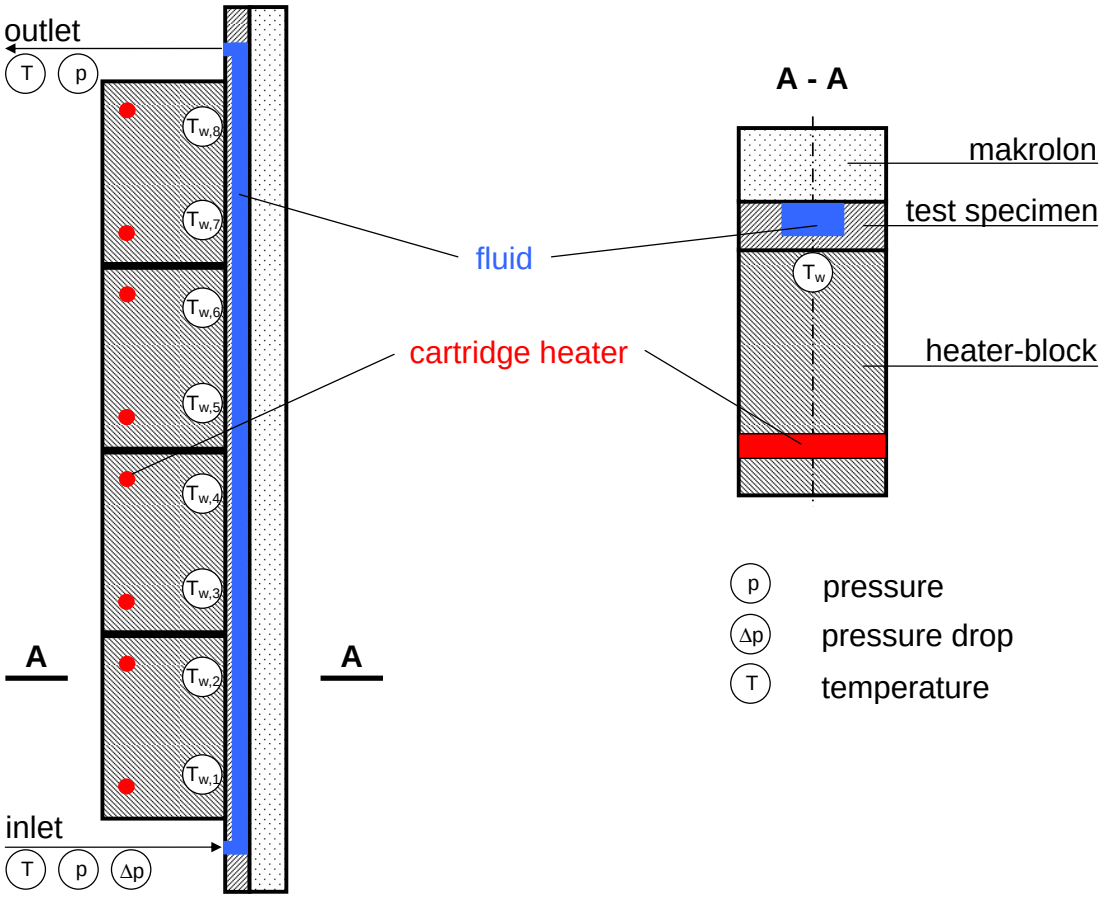

Figure 4.2: The test section

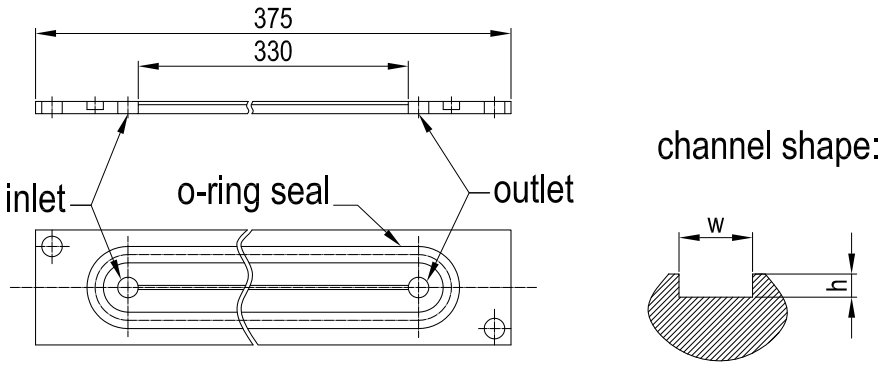

Figure 4.3: The test specimen

To enable flow visualisation, the upper channel side was covered by a transparent plate (makrolon). During installation, a thin nylon foil (for the 0.271 *mm* channel) or a thin teflon layer (for the 0.359 and 0.484 *mm* channels) was embedded between the makrolon plate and the test specimen surface to ensure good sealing. A digital high-speed video camera (Kodak Motion Analyser 4500) was employed to observe flow patterns and their transitions along the channel at the eight thermocouple positions.

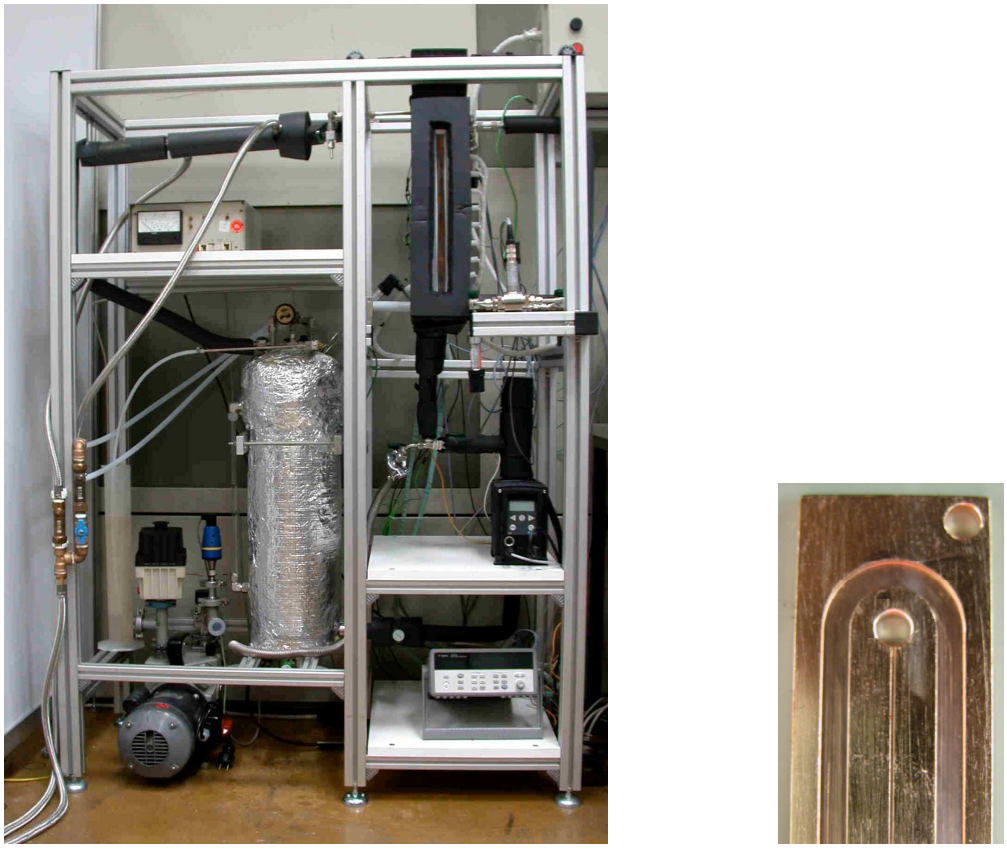

(a) experimental set-up (b) test specimen

Figure 4.4: Photographies of experimental set-up and test specimen

In order to analyse the heat transfer and the pressure drop phenomena four measurement parameters were determined:

- Fluid temperatures at the inlet and at the outlet of the test section (PT-100) and the wall temperature. The wall temperature T_w was measured at eight positions along the channel axis, viz. at $z = 47.5, 82.5, 123, 158, 198, 233, 273, 313$ *mm* behind the channel inlet.
- The inlet and the outlet fluid pressure (piezoresistive pressure sensors) and the pressure drop between the inlet and the outlet of the test section.

Because of the large pressure drop range two piezoresistive differential sensors with different working ranges were used. Such solution guaranteed good accuracy also in small pressure drop experiments.

- The input heating power (digital multimeter).
- The mass flow rate of the working fluid (embedded in pump).

Accuracy of measurements obtained by calibrations and error analysis is presented in Appendix F and G, respectively.

Finalising the description of the test rig photographies of the set-up and the test specimen are shown in Fig. 4.4.

4.2 Working fluids; why water?

Various fluids are considered for electronic cooling. There are several coolants (both dielectric and non-dielectric) commercially available. However, selection of the best coolant for a particular application requires a proper understanding of all the characteristics and thermo-physical properties of these fluids as well as of the device application and cooling method. Following is a list of some general requirements [91]:

- Good thermo-physical properties (high thermal conductivity and specific heat; low viscosity; high latent heat of evaporation for two-phase applications)
- Low freezing point
- High atmospheric boiling point (or low vapour pressure at the operating temperature) for single phase system; a low boiling point for a two-phase system
- Good chemical and thermal stability for long life of the electronics system
- High flash point and auto-ignition temperature (sometimes non-combustibility is a requirement)
- Non-corrosive to materials of construction (metals as well as polymers and other non-metals)
- No or minimal regulatory constraints (environmentally friendly, nontoxic, and possibly biodegradable)
- Economical

- In case of direct cooling methods low electrical conductivity

In case of direct cooling methods dielectric fluids (aromatics, silicate-ester, aliphatics, silicones, fluorocarbons) have to be used. Fluorocarbon liquids (perfluorocarbons (i.e., FC-72, FC-77) hydrofluoroethers (HFE) and perfluorocarbon ethers (PFE) [91]) are generally considered to be the most suitable liquids for direct immersion cooling, in spite of their poorer thermo-physical properties [4]. Description of other dielectric fluids can be found in reference [91]. Fluorocarbons are clear, colourless per-fluorinated liquids with a relatively high density and low viscosity. They also exhibit a high dielectric strength and a high volume resistivity [4]. These fluids are non-combustible and non-toxic. Some fluorinated compounds have zero ozone depleting potential and other positive environmental properties. Some of these fluids have low freezing points and low viscosity at low temperatures. However, these fluids are very expensive, have poor thermal properties, some of them have global warming potential (greenhouse effect), and, due to the extremely low surface tension, leaks can develop around fittings [91].

For indirect cooling non-dielectric liquid coolants are often used because of their superior thermal properties, as compared with the dielectric coolants. Non-dielectric coolants are normally water-based solutions. Therefore, they possess a very high specific heat and thermal conductivity. Some of those can work at temperature below $0\,^{\circ}C$, but they are either toxic (ethylene glycol) or flammable (ethanol/water mixture) or corrosive (calcium chloride solution). Even with higher price than calcium chloride, aqueous solutions of potassium formate and acetate salts have found a large number of applications in recent years, because they are non-flammable and non-toxic as well as not much corrosive and thermally quite efficient.

De-ionized water is a good example of a widely used electronics coolant. The possible limitations of using it are caused by the high electrical conductivity, the chemical incompatibility with some materials (e. g. aluminium) and the requirement of a working temperature above $0\,^{\circ}C$. Apart from these restrictions, water has a very good thermal performance. Additionally, it is non-toxic, non-flammable, commonly available, cheap and environmentally friendly.

In Table 4.2 thermophysical properties of most popular coolants for direct (fluorocarbons) and indirect cooling methods (water) are shown. It is clear that the thermal conductivity, specific heat and heat of vaporisation of fluorocarbon coolants are much lower than of water.

Because flow boiling belongs to the indirect cooling methods, heat transfer characteristics of the fluid become a major factor in choosing a refrigerant.

The test specimen made from copper material solves the corrosion problem. Working temperatures above $0\,^{\circ}C$ were planned for the investigation. As can

be seen, all limitations are omitted and therefore the good thermal characteristics as well as other advantages make water the best working fluid for research and for practical applications.

Table 4.2: Thermophysical properties of fluorocarbon coolants and water

property	FC-87	FC-72	FC-77	water
boiling point at 1 atm [$^\circ C$]	30	56	97	100
density x 10^{-3} [kg/m^3]	1.633	1.680	1.780	0.997
specific heat x 10^{-3} [Jkg$^{-1}K^{-1}$]	1.088	1.088	1.172	4.179
thermal conductivity [$Wm^{-1}K^{-1}$]	0.0551	0.0545	0.057	0.613
dynamic viscosity x 10^4 [$kgm^{-1}s^{-1}$]	4.20	4.50	4.50	8.55
heat of vaporisation x 10^4 [Jkg^{-1}]	8.79	8.79	8.37	243.8
surface tension x 10^3 [Nm^{-1}]	8.90	8.50	8.00	58.9
thermal coefficient of expansion x 10^3 [K^{-1}]	1.60	1.60	1.40	0.20
dielectric constant	1.71	1.72	1.75	78.0

Other fluid and surface properties (compressibility, electrokinetic effect, hydrophobicity, etc., see Chapter 2) could influence the flow boiling process.

The compressibility effect for liquid-gas flow was investigated by Kenning's group [38]. In order to avoid this effect, the working fluid was degassed by a special treatment, as described below.

For the present study the shape of the observed vapour bodies suggested a hydrophilic surface (compare Fig. 5.1 with Fig. 4.5), where the no-slip assumption and the Navier-Stoke equations are valid [36]. In the literature, the hydrophobicity effect was investigated usually in channels with hydraulic diameter up to 100 μm and only for this channel size its influence is proofed. The electrokinetic effect becomes significant in channels with hydraulic diameters below 40 μm [33]. Since the investigated channels have hydraulic diameters at least twice as big, the electrokinetic and the hydrophobicity effect can be neglected.

Water was de-ionised in a chemistry laboratory to avoid the influence of particles on the nucleation process. Afterwards, in order to reduce the amount of dissolved gasses and hence to eliminate any compressibility effect, the working fluid was degassed by an intensive boiling in the fluid tank above the operating temperatures (at about $\approx$ 120 $^\circ C$). Simultaneously, the air from other parts of the test rig was removed by a vacuum pump.

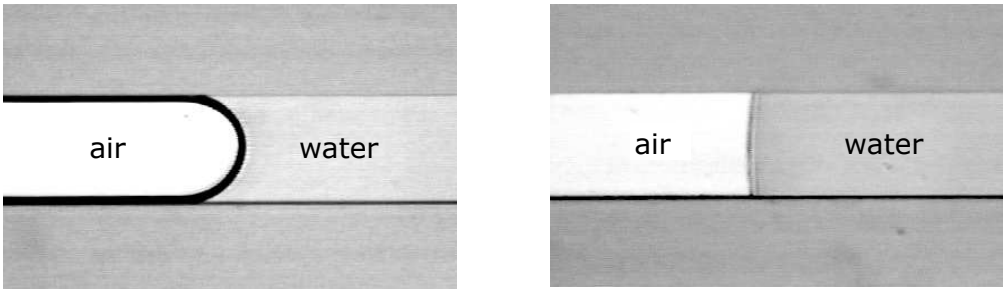

(a) Water in hydrophilic microchannel (b) Water in hydrophobic microchannel

Figure 4.5: Hydrophobicity effect in microchannel [33]

4.3 Experimental conditions

Before the flow boiling experiments started, calibration of sensors, treatment of the working fluid and the (a)diabatic single-phase flow experiments have been carried out. The calibrations of pressure sensors and thermocouples were carried out before their installation, Appendix F.

For every channel the same procedure was applied, comprising the following steps:

- calibration of flow meter embedded in the pump (Appendix F),
- degassing of water (see section 4.2),
- adiabatic single-phase flow experiments (Appendix A),
- diabatic single-phase flow experiments in order to estimate a heat loss function (Appendix B),
- evacuation of whole set-up by means of a vacuum pump (Leybold-Heraeus D6A single-stage oil pump, 10^{-1} *mbar*),
- diabatic two-phase flow experiments (Chapter 5).

Before going into details about the experimental conditions in terms of mass and heat fluxes the limitations of the used set-up should be underlined. The mass flux range during single-phase flow for different channels was limited either by too high pressure drop (0.271 *mm* channel) or by the maximum flow rate of the pump (0.359 and 0.484 *mm* channel). However, in all cases experiments could be performed up to 1000 kg/m^2s, as it was planned at the beginning. The pump (dosing pump DME 2-18, TELAB Technology GmbH) covers a flow rate range from 15 ml/h to 2.5 l/h and it can work against a pressure of up to 18 *bar*. During experiments the whole possible working range was tested.

Second kind of limitation was caused by the properties of the used transparent plate (melting point at $\approx 130\,^{\circ}C$). Since from experience it is well known that makrolon starts to creep at about $100\,^{\circ}C$, the fluid temperature was limited. In consequence the applied heat flux and hence vapour quality was also limited.

Single-phase flow experiments were performed to validate the set-up and show eventual discrepancy with theory. Additionally a heat balance of the diabatic data allowed to estimate the heat loss of the two-phase flow experiments. In Table 4.3 experimental conditions for single-phase flow (adiabatic and diabatic cases) are presented.

Table 4.3: Single-phase flow experimental conditions

hydraulic diameter [mm]	mass flux [kg/m^2s]	heat flux [kW/m^2]
0.271	50 - 7000	-
	50 - 6500	7 - 260
0.359	50 - 5000	-
	100 - 5000	4 - 650
0.484	50 - 2600	-
	200 - 2600	8 - 400

The *two-phase flow* investigations were performed for two different outlet pressures. The bigger one (about 0.9 *bar*) was chosen because of similarity with environment pressure. It was assumed that in technical cooling systems ambient pressure would be a most convenient working condition. A pressure below 0.6 *bar* at the outlet was applied to reach saturation condition sooner than for 0.9 *bar* outlet pressure. A low outlet pressure allowed to consider a larger distance, where two-phase flow occurs, and hence flow patterns and their transitions could be investigated in a larger region. Note, the large inlet subcooling range is a consequence of different outlet pressures and mass fluxes.

Table 4.4: Two-phase flow experimental conditions

hydraulic diameter [mm]	mass flux [kg/m^2s]	heat flux [kW/m^2]	inlet subcooling [K]
0.271	100 - 2000	19 - 148	7 - 62
0.359	100 - 2500	25 - 198	13 - 64
	2600 - 4500	72 - 462	43 - 79
0.484	100 - 2500	16 - 335	18 - 61

The raw data were collected and saved during steady state by means of Data Acquisition Switch Unit Agilent 34970A and computer program VEE Pro 6.0.

Chapter 5

Experimental results

This chapter is the essential part of the present work. Experimental results and discussions considering visualisation, pressure drop and heat transfer during flow boiling are presented.

5.1 Visualisation and flow pattern maps

High-speed videos were recorded at every thermocouple position along the channel axis, when two-phase flow was observed. The main goal of visualisation was to define flow patterns for given conditions (hydraulic diameter, mass and heat flux) along the channel axis in order to obtained a better understanding of the heat transfer mechanism. Some noteworthy tendencies were observed. Because of a relatively big human error occurring during the image evaluation, the results presented in this chapter are essentially of qualitative nature.

Basic flow patterns

As discussed in Chapter 3.2 three basic flow patterns were defined: bubbly, slug and annular flow. In Fig. 5.1 real images of bubbly, slug and annular flow for the three channels are presented. No distinguishable differences within the same flow pattern (e. g. bubbly flow) were observed in the investigated channels .

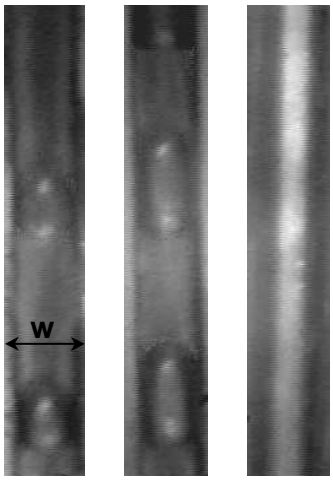

(a) $d_h = 0.271\ mm$ ($w = 0.289\ mm,\ h = 0.255\ mm$)

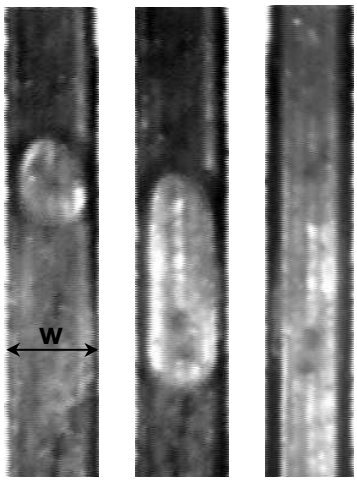

(b) $d_h = 0.359\ mm$ ($w = 0.550\ mm,\ h = 0.266\ mm$)

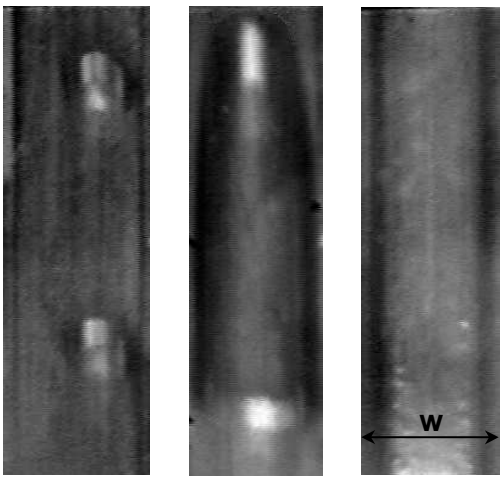

(c) $d_h = 0.484\ mm$ ($w = 0.807\ mm,\ h = 0.346\ mm$)

Figure 5.1: Photographies of bubbly, slug and annular flow in the channels

Vapour body velocity

For all channels and three mass fluxes (300, 700 and 1500 kg/m^2s) and various heat fluxes the number of vapour bodies, their velocities and lengths were directly or indirectly obtained from video recordings (see Chapter 3.2). These data are presented in Figs. 5.2 and 5.3. For every vapour body the velocities of its top (closed symbol) and its bottom (open symbol) are presented. The dashed horizontal line indicates the approximate inlet liquid velocity (at the channel inlet there were always subcooled conditions ensuring only liquid flow). The unexpected low vapour body velocities characterised a small bubble flowing close to the channel wall and is a consequence of the velocity profile in the duct. The dashed vertical lines shown from the left to the right correspond to different vapour body lengths: equal to the depth and equal to one, ten, fifty and one hundred times the channel width (see Table 3.1).

From Fig. 5.2 and Fig. 5.3 it is becomes obvious that the velocity of a vapour body increases with its increasing length up to a certain value and then remains unchanged or nearly constant. The increasing tendency is observed for a ratio $L_{vb}/w < 1$ in any case. For some conditions the increasing tendency is observed till the vapour body length equals ten times the channel width (e. g. Fig. 5.2a and for 700 kg/m^2s in Fig. 5.3).

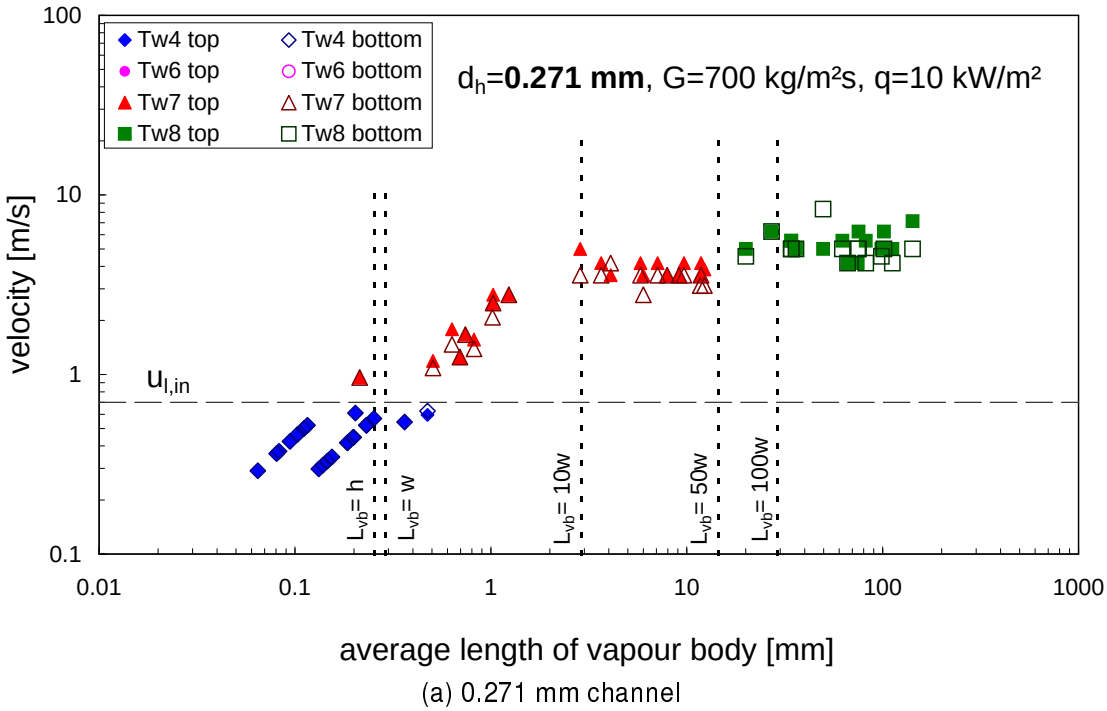

(a) 0.271 mm channel

Figure 5.2: Vapour body velocity vs. vapour body length

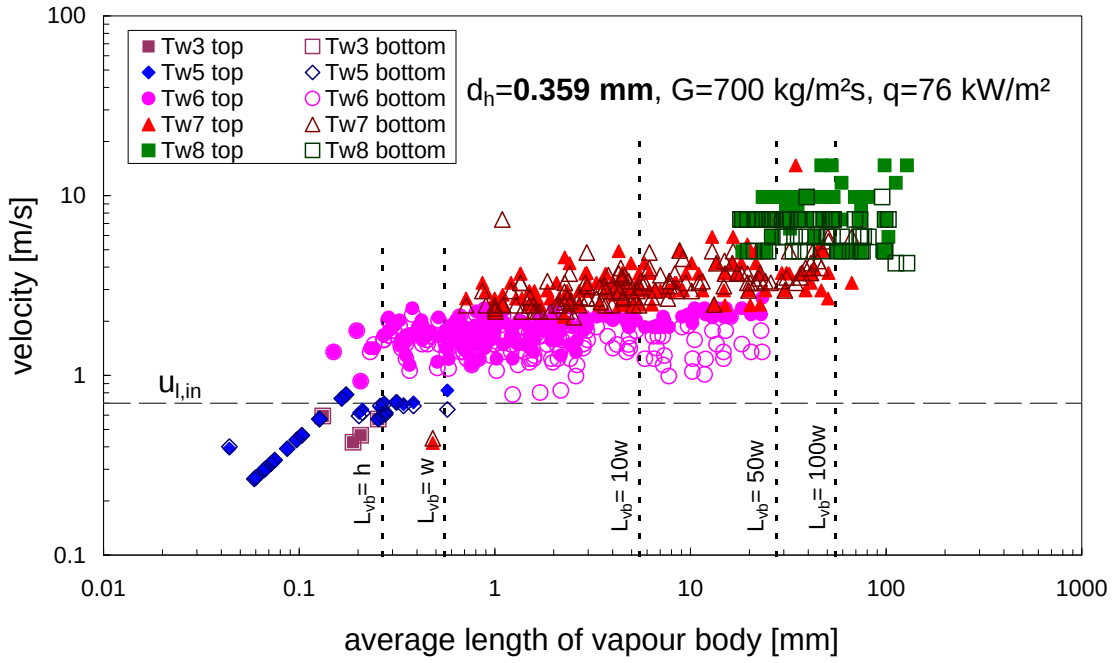

(b) 0.359 mm channel

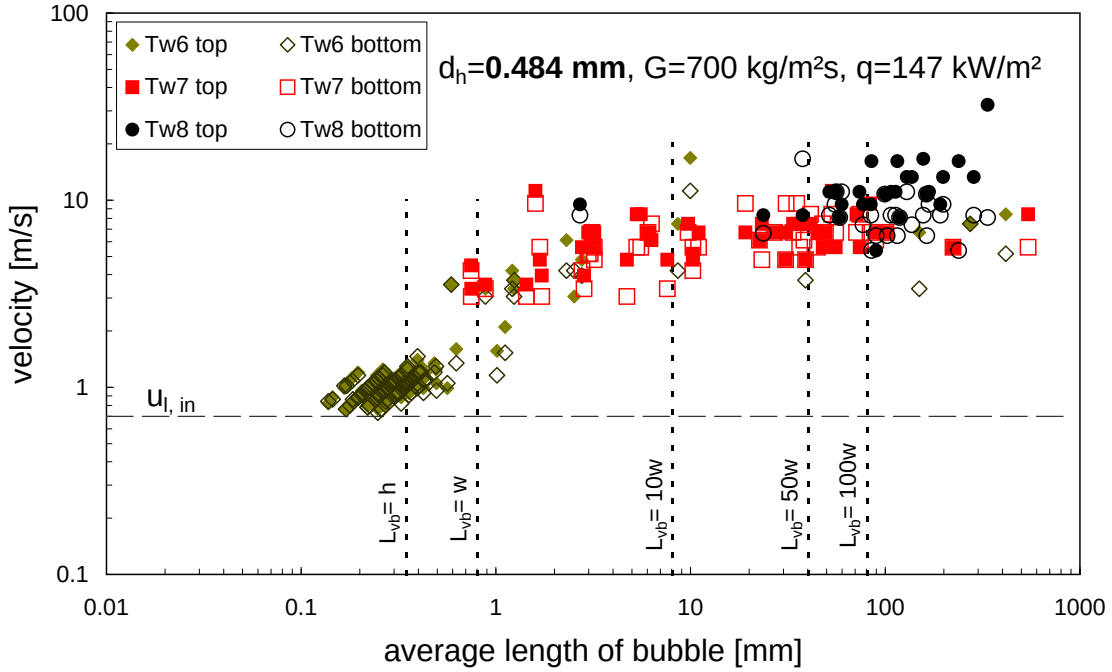

(c) 0.484 mm channel

Figure 5.2: Vapour body velocity vs. vapour body length (continued)

Additionally it was found that the velocity of the vapour body at its top is usually higher than that at its bottom which is due to evaporation (vapour slug growth). A vapour body elongation due to the pressure drop could also be a factor but due to the small view window a more detailed study was not possible. A rough estimation of pressure change within one slug shows that for the considered experiments this effect can be neglected (see Appendix C).

Investigating the influence of mass flux on the vapour body velocity (Fig 5.3) some tendencies are observed . The velocity increases with increasing mass flux up to a vapour body length equal ten times the channel width. For mass flux 1500 kg/m^2s the slope is lower than for 700 kg/m^2s. For higher vapour body lengths $L_{vb} > 50w$ the influence of mass flux is not distinguishable. Note that for mass flux 1500 kg/m^2s very long vapour slugs were not observed (it would have required a very high heat flux which, because of a technical temperature limitation could not applied, see Chapter 4.1). A summarising schematic diagram of the influence of mass flux on vapour body velocity is presented in Fig. 5.4. The limited influence of mass flux on the vapour body velocity can be explained as follows. In the "mass flux influence" region there are bubbles and short vapour slugs. Isolated bubbles move upwards almost uninfluenced by wall effect (almost free rising). The pumping force (mass flux) and buoyancy control their velocities. For short vapour slugs ($1w < L_{vb} < 10w$) shear

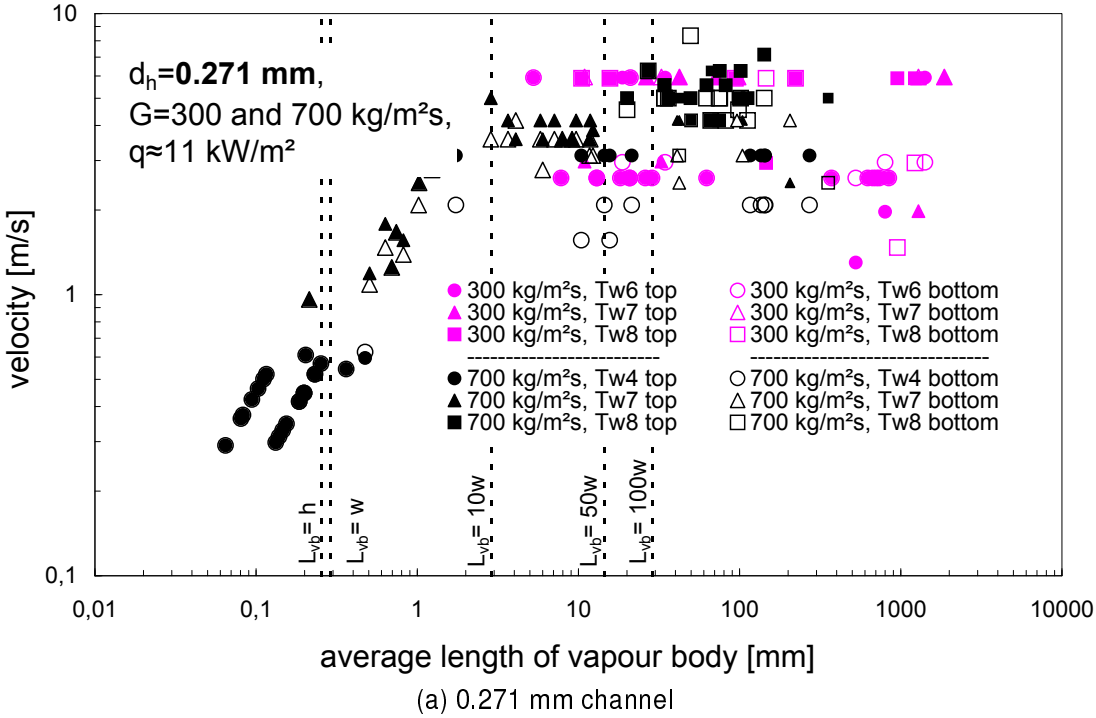

(a) 0.271 mm channel

Figure 5.3: Influence of mass flux on the vapour body velocity

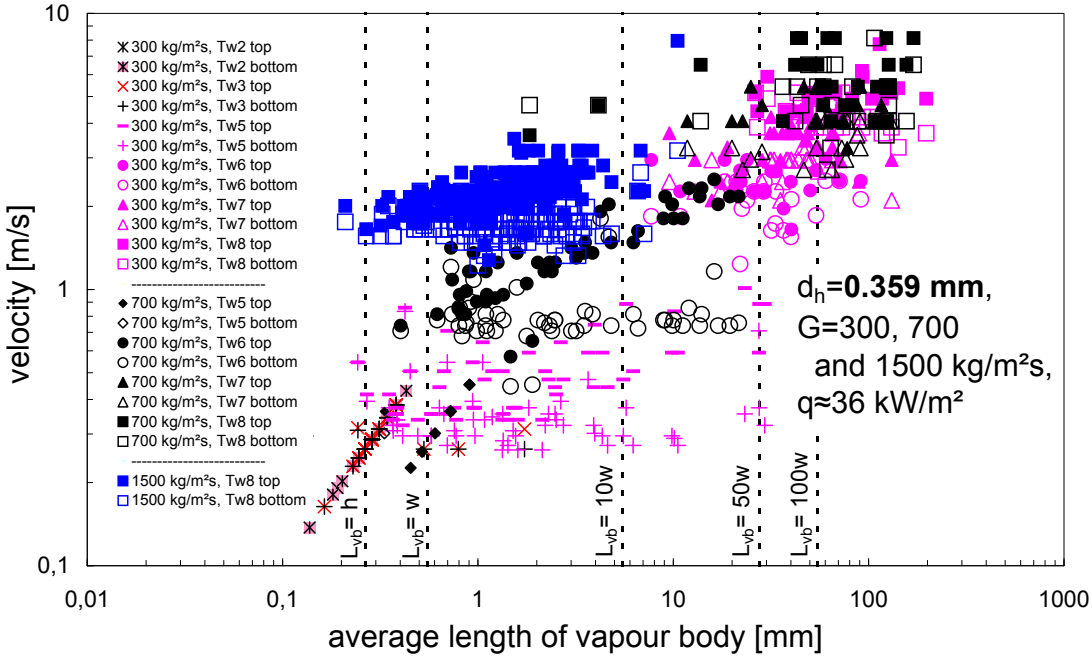

(b) 0.359 mm channel

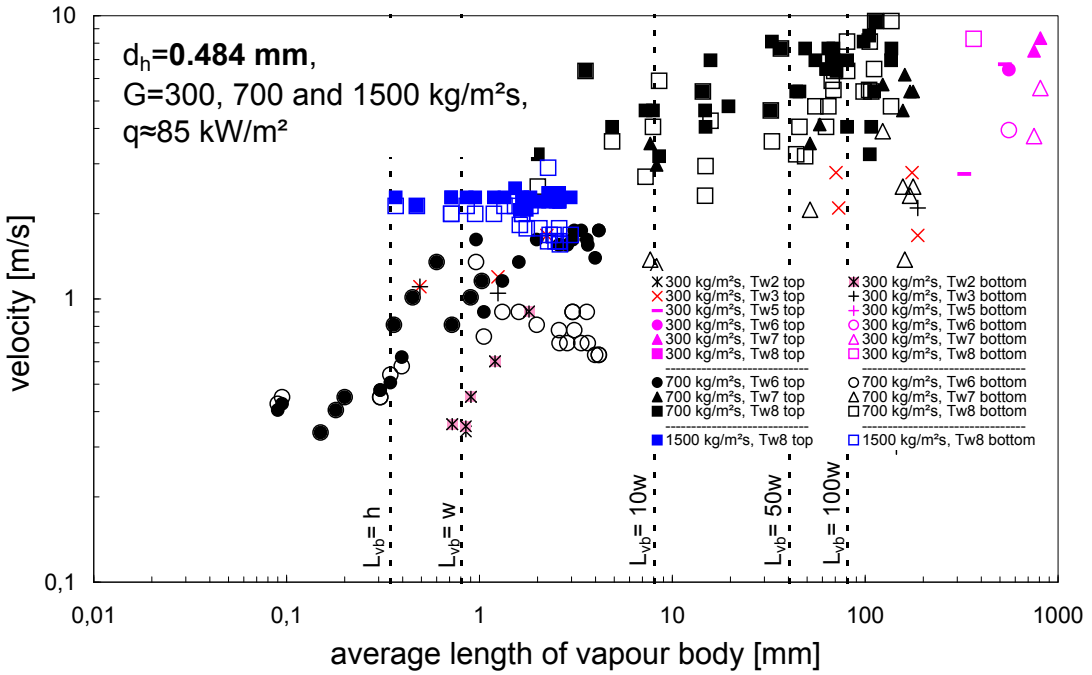

(c) 0.484 mm channel

Figure 5.3: Influence of mass flux on the vapour body velocity (continued)

stress becomes important but still inertia is a dominant force. The velocity of a much longer vapour slug ($L_{vb} > 50w$) seems to be determined mostly by heat flux. For the given hydraulic diameter and two different mass fluxes, the same heat flux generates the same amount of vapour and in consequence, with assumption of constant fluid temperature, the same volumetric flow rate of vapour. Assuming that the vapour occupies the whole cross-sectional area (void fraction close to one) and using the continuity equation, one can find out that the vapour body velocity is equal for two different mass fluxes and ceteris paribus (other conditions constant).

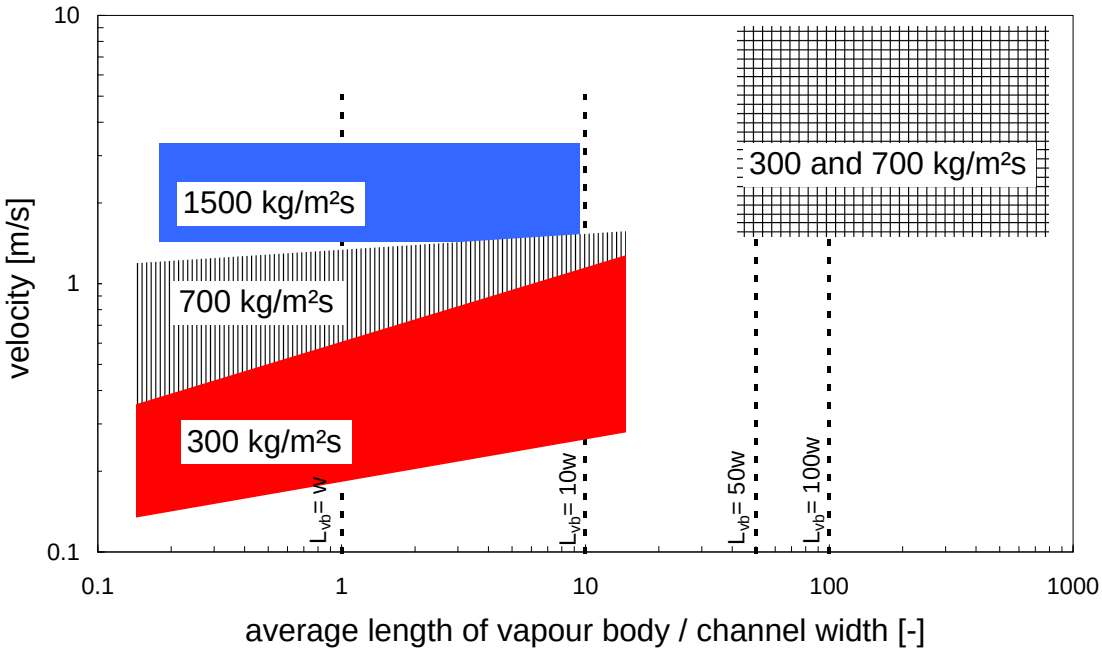

Figure 5.4: Influence of mass flux on the vapour body velocity - general

Summarising the above discussion: the mass flux influences the velocity of bubbles and vapour slugs with a length shorter than about ten times the channel width. For higher vapour body length $L_{vb} > 50w$ the influence of mass flux is not distinguishable. Because for the present visualisation, a typical annular flow was not observed (there were always some liquid bridges which interrupt the vapour core), the slug-annular transition has to be assumed and as a criterion the mass flux influence can be used. Based on the above discussion annular flow can be regarded as flow with vapour slugs uninfluenced by mass flux. In consequence, a flow with vapour slugs longer than fifty times the channel width is defined as annular flow in this study.

Histograms

In general, for a given position more than one type of vapour body was observed. In this case flow patterns were defined according to the dominant one by means of histograms. In Fig. 5.5 histograms of vapour body length for different mass fluxes at a similar heat flux ($q = 110$ to $131\ kW/m^2$) in the $0.484\ mm$ channel are presented. For example, for high mass flux in Fig. 5.5c for all three positions (positions of thermocouples Tw6, Tw7 and Tw8) bubbles and short vapour slugs were observed. At Tw6-position bubbles (with length smaller than $0.81\ mm$) account for about 43 % of total vapour body number. At Tw7- and Tw8-positions vapour slugs with a length greater than $0.81\ mm$ account for about 66 % and 61 %, repectively, of total observed vapour body number. Hence slug flow, per definition, was found at three positions (Tw6, Tw7 and Tw8). At low mass flux (Fig. 5.5a) bubbly flow dominated at the positions near the channel inlet (Tw1, Tw2). Away from the channel inlet slug flow (Tw3) and annular flow (Tw5 - Tw8) became dominant. With increasing mass flux bubbly and slug flows became more and more dominant.

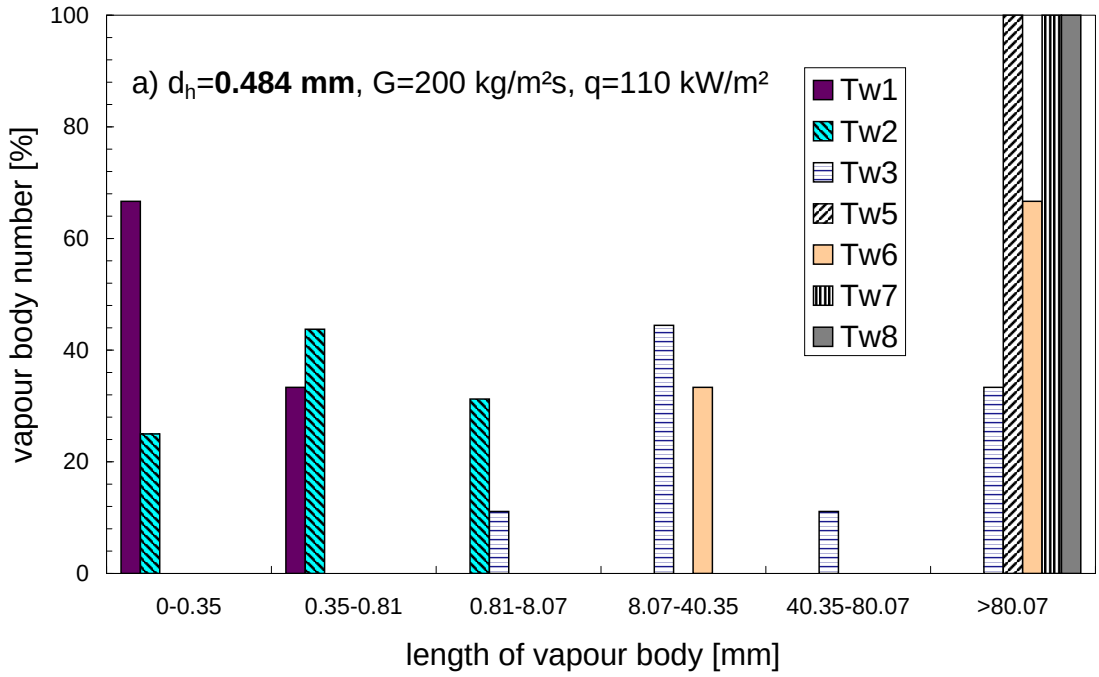

Figure 5.5: Histograms of vapour body lengths for heat fluxes of 110 to $131\ kW/m^2$ in the $0.484\ mm$ channel

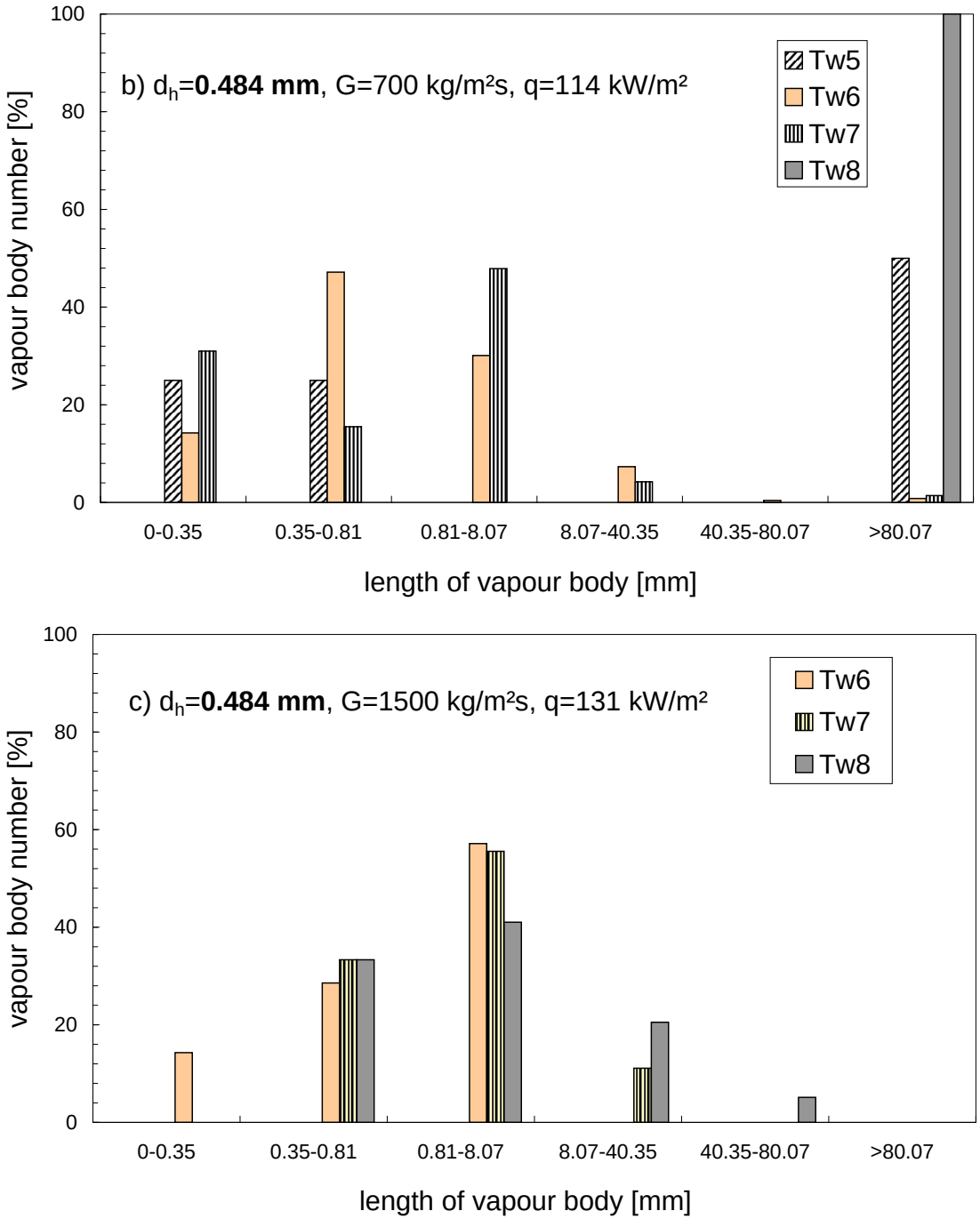

Figure 5.5: Histograms of vapour body lengths for heat fluxes of 110 to 131 kW/m^2 in the 0.484 *mm* channel (continued)

Void fraction

Based on the visualisation the experimental void fraction was determined (Chapter 3.2). Experimental data were compared with the empirical void fraction equation (Eq. 3.35) with constants proposed by Lockhart and Martinelli. In order to improve the agreement the correlation was modified, viz. exponent n_3 was varied. The best agreement was found by changing the exponent of the viscosity term in Eq. 2.3 from 0.07 to 0.30, Fig. 5.6. Physically it means that the slip ratio is increasing and in consequence the liquid velocity diminishes (for the detailed explanation see Appendix E).
Table 5.1 presents a comparison between experimental and calculated void fractions. Eq. 3.35 with both $n_3 = 0.07$ and $n_3 = 0.3$ was further used to calculate the flow boiling pressure drop (Chapter 5.2).

Table 5.1: Comparison of experimental void fraction with calculated data

d_h [mm]		MAE [%]	percentage within error		
			$\pm$10 %	$\pm$20 %	$\pm$30 %
0.271	$n_3 = 0.07$	45	31	77	85
	$n_3 = 0.3$	35	50	62	73
0.359	$n_3 = 0.07$	69	11	55	71
	$n_3 = 0.3$	40	44	62	73
0.484	$n_3 = 0.07$	58	14	43	72
	$n_3 = 0.3$	31	31	57	72
all channels	$n_3 = 0.07$	61	16	57	74
	$n_3 = 0.3$	37	42	61	73

From Fig. 5.6, one can see that for saturation condition there are only few samples of bubbly flow. They occurred for thermodynamic vapour quality $x_{th} < 0.01$ and void fraction $\alpha < 0.1$. A very simple geometrical consideration for adiabatic flow (Mishima and Ishii [51]) points out a much higher value $\alpha = 0.3$ as bubbly-slug boundary. Slug flow was observed up to $\alpha \approx 0.7$. Annular flow was observed at void fractions mostly higher than 0.6, although some points were down to $\alpha \approx 0.1$. The slug-annular boundary can be roughly placed for void fraction equal 0.65.

Based on data of Fig. 5.6, the α- and the x_{th}-ranges for the occurrence of the different flow patterns are presented in Table 5.2. Note that the bubbly-slug transition inferred from this figure has to be treated with care, because of the limited number of bubbly flow data points under saturation conditions.

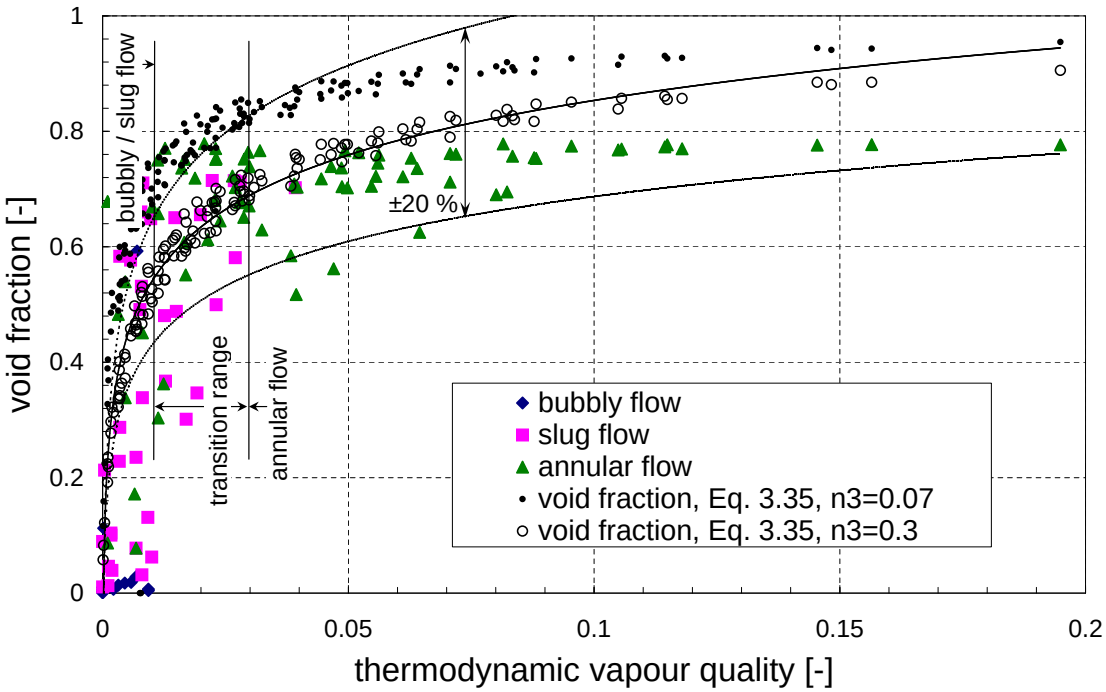

Figure 5.6: Experimental void fraction and comparison with Lockhart-Martinelli correlations Eq. 3.35

Table 5.2: Flow pattern ranges

	void fraction [-]		thermodynamic vapour quality [-]	
	range	transition	range	transition
bubbly flow	$0 \cdots 0.1$	≈ 0.1	$0 \cdots 0.01$	≈ 0.01
slug flow	$0 \cdots 0.7$	≈ 0.65	$0 \cdots 0.03$	$0.01 \cdots 0.03$
annular flow	$0.1 \cdots 0.8$		$0.01 \cdots 0.2$	

Flow pattern maps

In all figures presented in this chapter bubbly, slug and annular flows are designed by the symbols: diamond, circle and triangle, respectively. The figures include data points obtained for all investigated channels.

As aforementioned, the visualisation can lead to a better understanding of the heat transfer mechanism. The thermodynamic vapour quality and mass flux are strongly representative for the heat transfer performance. Therefore, the flow patterns have been presented in a form to account for these two parameters.

In Fig. 5.7 the change of flow patterns with thermodynamic vapour quality for

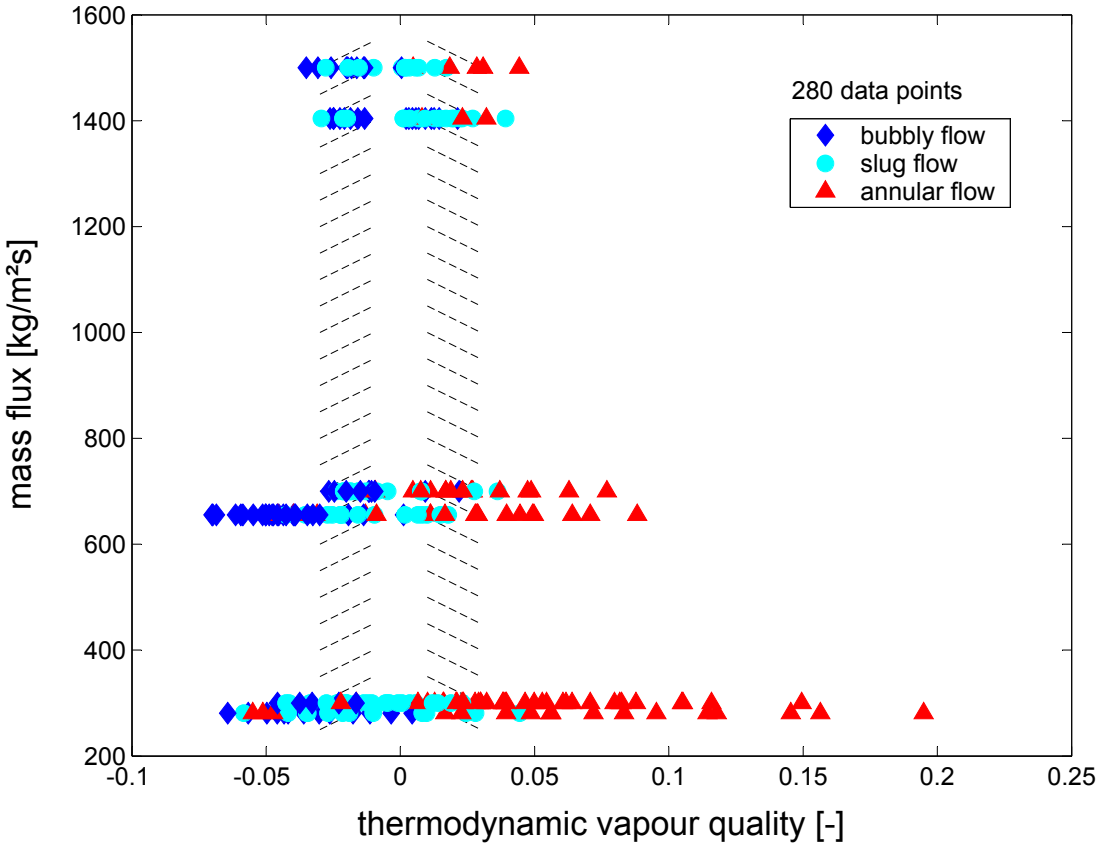

Figure 5.7: Flow pattern map: mass flux vs. thermodynamic vapour quality

different mass fluxes is shown. Bubbly flow occurred mostly for subcooled conditions ($x_{th} < 0$). With increasing vapour quality due to evaporation and eventually an agglomeration of bubbles (rarely observed and mostly for bubbly flow), slug and annular flow were observed.

The occurrence of different flow patterns in defined x_{th}-ranges is shown in Fig. 5.8. For thermodynamic vapour qualities lower than -0.03 bubbly flow clearly dominates. Slug flow was observed mostly at vapour qualities in the range $-0.01 < x_{th} < 0.01$. Annular flow dominates for $x_{th} > 0.03$. In the range $-0.03 < x_{th} < -0.01$ bubbly and slug flow were observed with almost the same frequency (≈ 43 %).
More detailed data are shown in Table 5.3. The thermodynamic vapour quality ranges are presented for which the respective flow patterns occur in more than 50% of the cases. From the overlapping regions the flow pattern transition ranges can be inferred (hatched areas in Fig. 5.7). For $-0.03 < x_{th} < -0.01$ the bubbly-slug transition occurs. The change from slug into annular flow is observed at $0.01 < x_{th} < 0.03$ with a dominance towards $x_{th} = 0.01$.

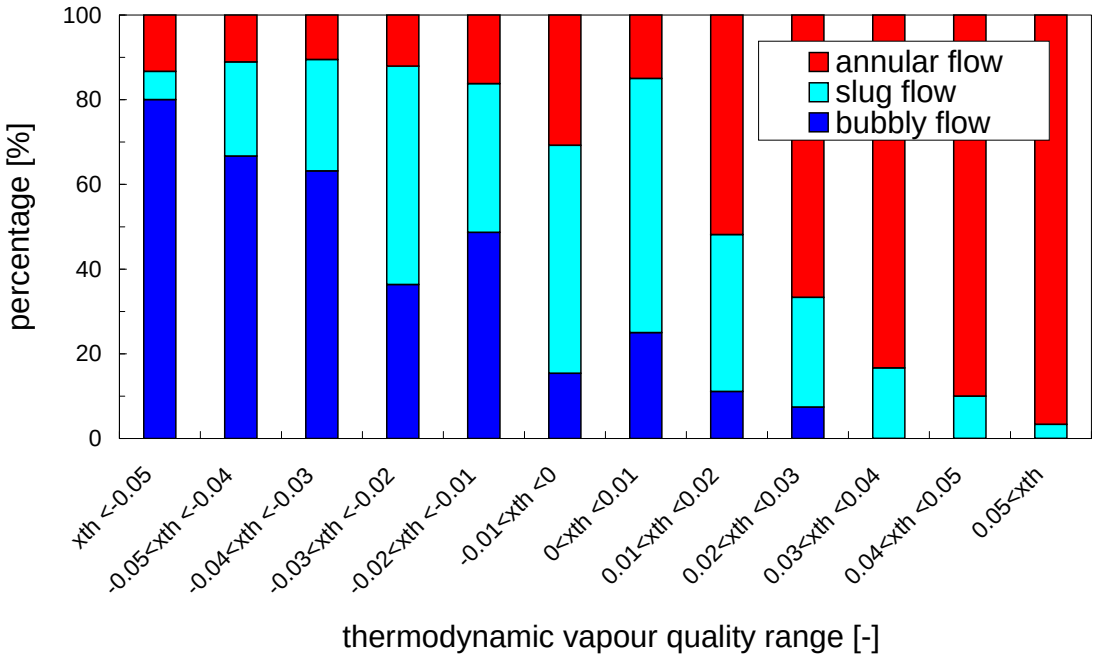

Figure 5.8: Percentage of occurrence of flow patterns in thermodynamic vapour quality regions

Table 5.3: The x_{th}-ranges for flow patterns

$d_h[mm]$	mass flux $[kg/m^2s]$	x_{th}-range (resp. pattern > 50 %)		
		bubbly	slug	annular
0.271	300	–	$-0.03 \cdots 0.01$	$0.01 \cdots 0.11$
	700	–	$-0.03 \cdots -0.01$	$0.01 \cdots 0.065$
	1500	–	$0 \cdots 0.01$	$0.01 \cdots 0.05$
0.359	300	$-0.05 \cdots 0$	$-0.01 \cdots 0.03$	$0.01 \cdots 0.19$
	700	$-0.07 \cdots -0.03$	$-0.03 \cdots 0.01$	$0.01 \cdots 0.15$
	1500	$-0.03 \cdots -0.01$	$0 \cdots 0.04$	$0.03 \cdots 0.04$
0.484	300	$-0.04 \cdots -0.03$	$-0.02 \cdots 0.01$	$0.01 \cdots 0.15$
	700	$-0.03 \cdots -0.01$	$-0.03 \cdots 0.03$	$0.01 \cdots 0.05$
	1500	$-0.04 \cdots -0.01$	$-0.01 \cdots 0.03$	–

In Fig. 5.9 experimental flow pattern results are presented with respect to superficial velocities. The hatched areas roughly represent transitions regions between the patterns. Three experimental data sets are shown which represent different mass fluxes (300, 700 and 1500 kg/m^2s). It is a consequence of the definition of the liquid superficial velocity (Eq. 2.17), that for a small thermodynamic vapour quality range and relatively constant liquid density the liquid superficial velocity changes almost insignificantly.

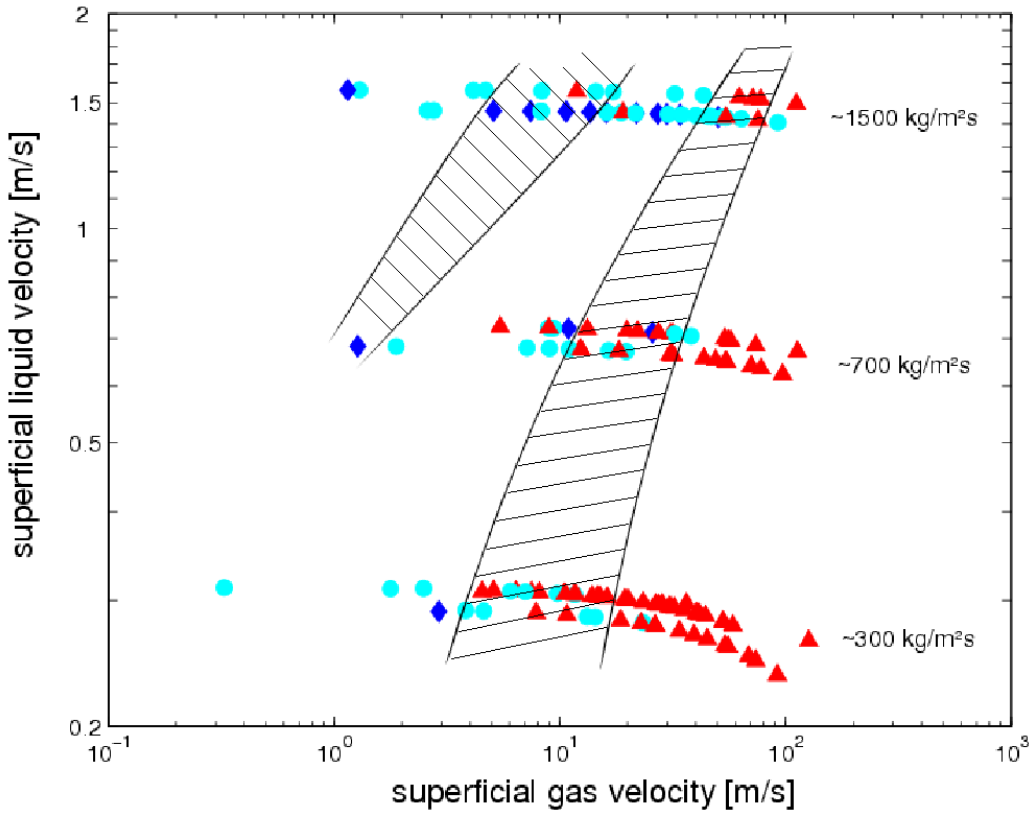

Figure 5.9: Flow pattern map: superficial liquid velocity vs. superficial gas velocity (experimental data)

For the same data as in Fig. 5.9 flow pattern transition boundaries proposed by different authors (see Chapter 2.2) are presented in Fig. 5.10. A discussion of the bubbly-slug transition is impeded because of limited bubbly flow points (bubbly flow occurs usually only for a subcooled condition). The slug-annular transitions proposed by Taitel at al. [50] and by Mishima and Ishii [51] (for big and small channels) are formulated as a constant superficial gas velocity (Eqs. 2.6, 2.9, 2.10, respectively). These boundaries (which depend on fluid properties) were calculated for every sample and therefore are shown as transition ranges instead of a single line.

None of presented flow pattern transition boundaries describes the experimental data precisely. The ”best” agreement was with the slug-annular transition (dash-dotted line) proposed by Tabatabai and Faghri [54] and the intermittent-annular criterion proposed by Zürcher et al. [56], Eq. 2.14 (solid blue line). Between these two criteria the experimental slug-annular transition range is placed with quite good accuracy (for 1500 kg/m^2s the Tabatabai-Faghri-criterion underpredicts the experimental boundary).

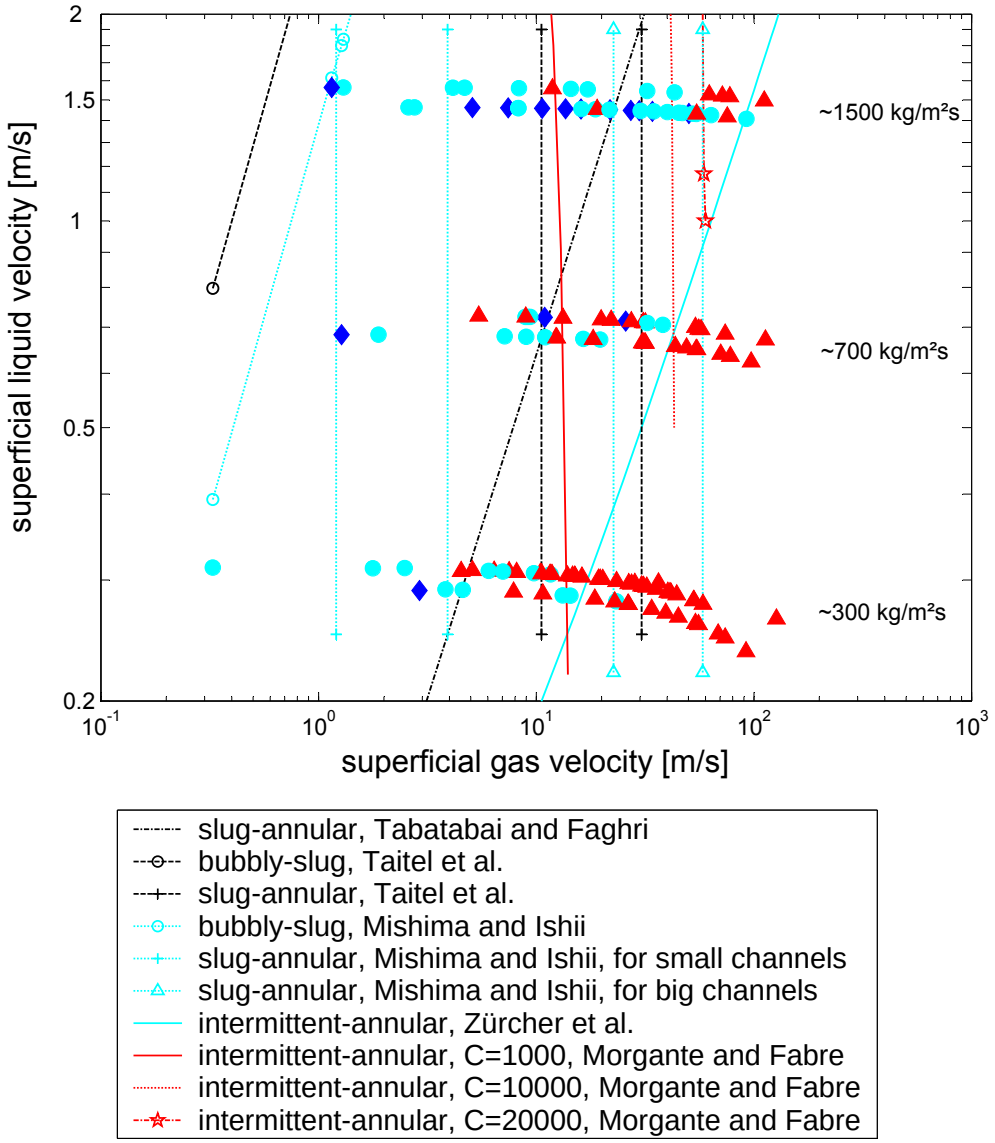

Figure 5.10: Flow pattern map: superficial liquid velocity vs. superficial gas velocity (comparison with theory)

Mishima and Ishii used their model criteria also for comparison with experimental data of a steam-water flow at high pressure in a rectangular channel $d_h = 5.64\ mm$ (Hosler [92], cited from [51]). The comparison had shown reasonable agreement. In our case, the most probable reason for the differences between the theory and the experimental results was the different inlet pressure which for the presented experiments was smaller than in the Hosler-data base. Their assumption that the void fraction during bubbly-slug transition was $\alpha = 0.3$ [51] can also be an additional reason.

Taitel et al. compared their model criteria with experimental data from a air-

water flow at low pressure in pipes with $d_h = 20 - 60\ mm$. In our case, the proposed churn-annular (slug-annular) criterion works quite well but only for 700 kg/m^2s, Fig. 5.10. For the bubbly-slug boundary, their void fraction assumption $\alpha = 0.25$ [50] could be a reason for the large discrepancy to the experimental data.

In the presented graph the intermittent-annular transition proposed by Morgante and Fabre [57] was calculated for a Weber number $We = 1000$, 10000 and 20000 (constant C in Eq. 2.15). Note that they proposed for the $1x1\ mm^2$ channel $We = 10$. With increasing Weber number this boundary moves to higher values of the superficial gas velocity. Only for such high values the annular flow initiation can be described for mass fluxes of 300, 700 and 1500 kg/m^2s, respectively. Physically it means that the inertia force has to be much stronger than the capillary force in order to guarantee vapour flow in the channel core and a liquid layer around it.

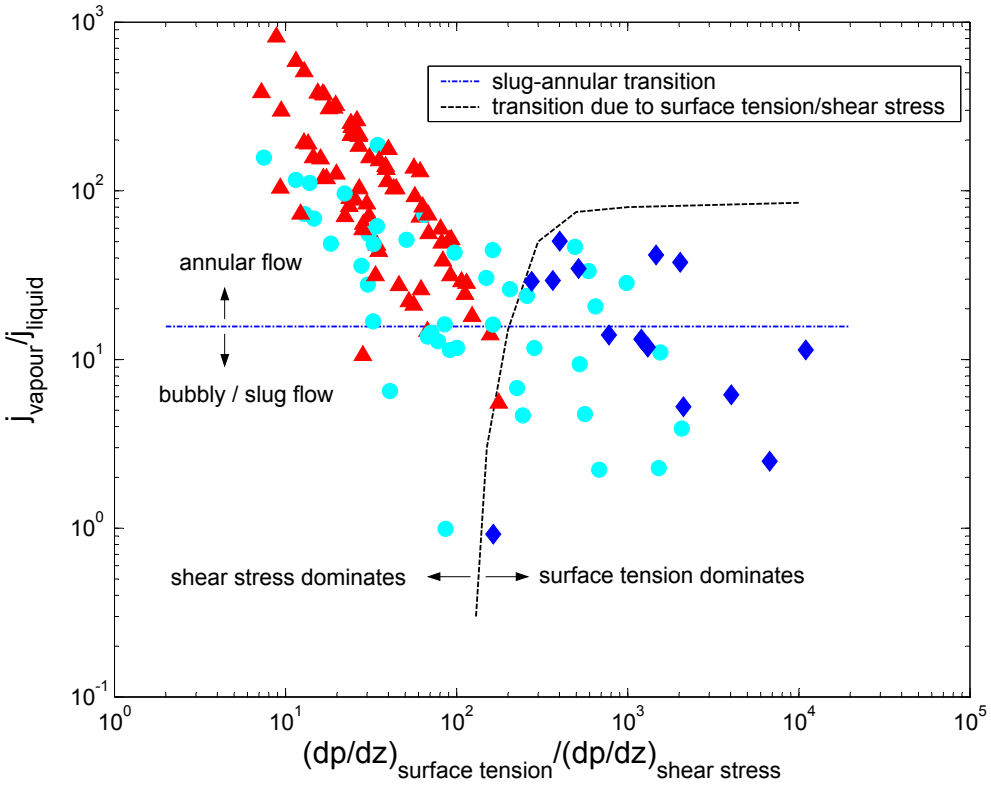

Figure 5.11: Flow pattern map proposed by Tabatabai and Faghri [54]

Following Tabatabai and Faghri, two regions can be distinguished, one with dominance of surface tension and a second with shear stress as the main force (dotted line in Fig. 5.11). In the first one the dominance of surface tension allows bubbly flow to occur. For annular and slug flow (with relatively long slugs) shear stress becomes dominant. The slug-annular boundary (the same

as presented in Fig. 5.10) predicts experimental data quite well. The occurrence of slug flow in the surface tension region as well as in the shear stress dominated region can be explained by the wide definition of slug flow (Chapter 3.2). It can be either a flow with short slugs and some bubbles, where surface tension is the dominant force or a flow with relatively long slugs, but not sufficiently long to call it annular flow (shear stress dominates).

5.2 Two-phase pressure drop

Pressure drop, as one of three aspects of flow boiling, was measured during experimental investigations. The measured values were compared with the predictions given by the model described in Chapter 3.3. This is based on the governing equations (conservation of mass, energy and momentum: Eqs. 3.12, 3.13 and 3.14, respectively). The momentum equation can be described as the total pressure drop correlation, within which three components are distinguished: acceleration, gravitational and frictional term. The single- and two-phase regions were considered separately during calculation. For the frictional two-phase pressure drop the Lockhart-Martinelli method was used (Eq. 3.17-3.30). The void fraction was calculated from Eq. 3.35 with constants proposed by Lockhart and Martinelli.

In further discussion any "calculated pressure drop" or "prediction" should be understood as value calculated according to this algorithm. The terms "model" and "program" are also related to this algorithm as long as nothing else is mentioned.

Figure 5.12 presents the experimental total pressure drop versus thermodynamic vapour quality at the channel outlet for the three channels and different mass fluxes. It can be concluded that the total pressure drops increase with increasing thermodynamic vapour quality and mass flux and decrease with increasing hydraulic diameter, as was expected.

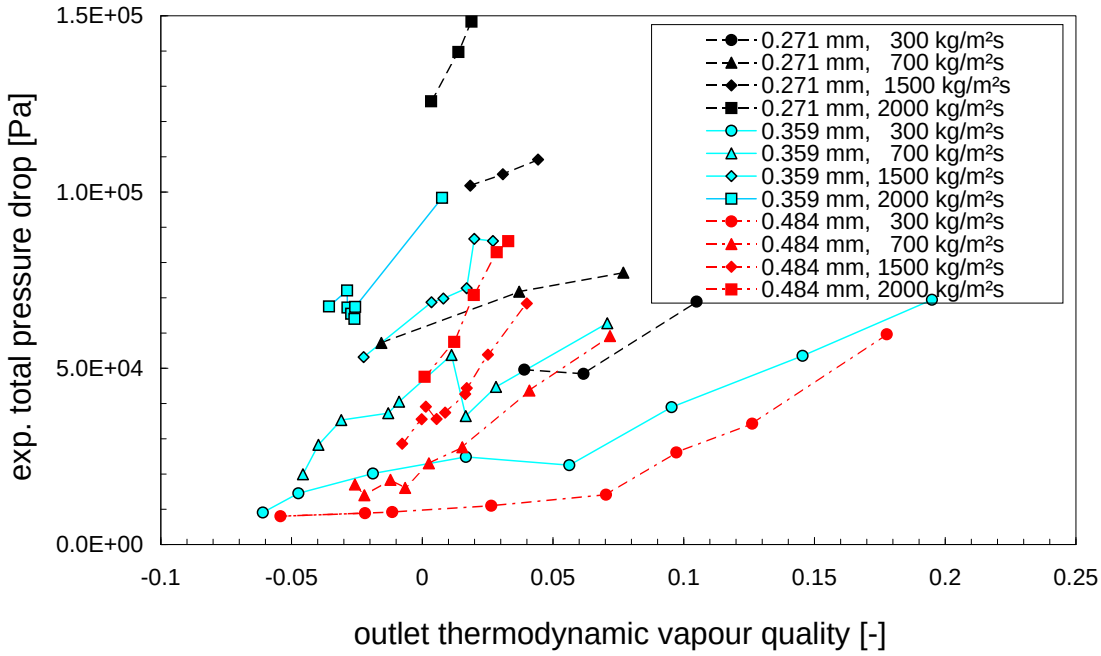

Figure 5.12: Experimental total pressure drop for the three channels

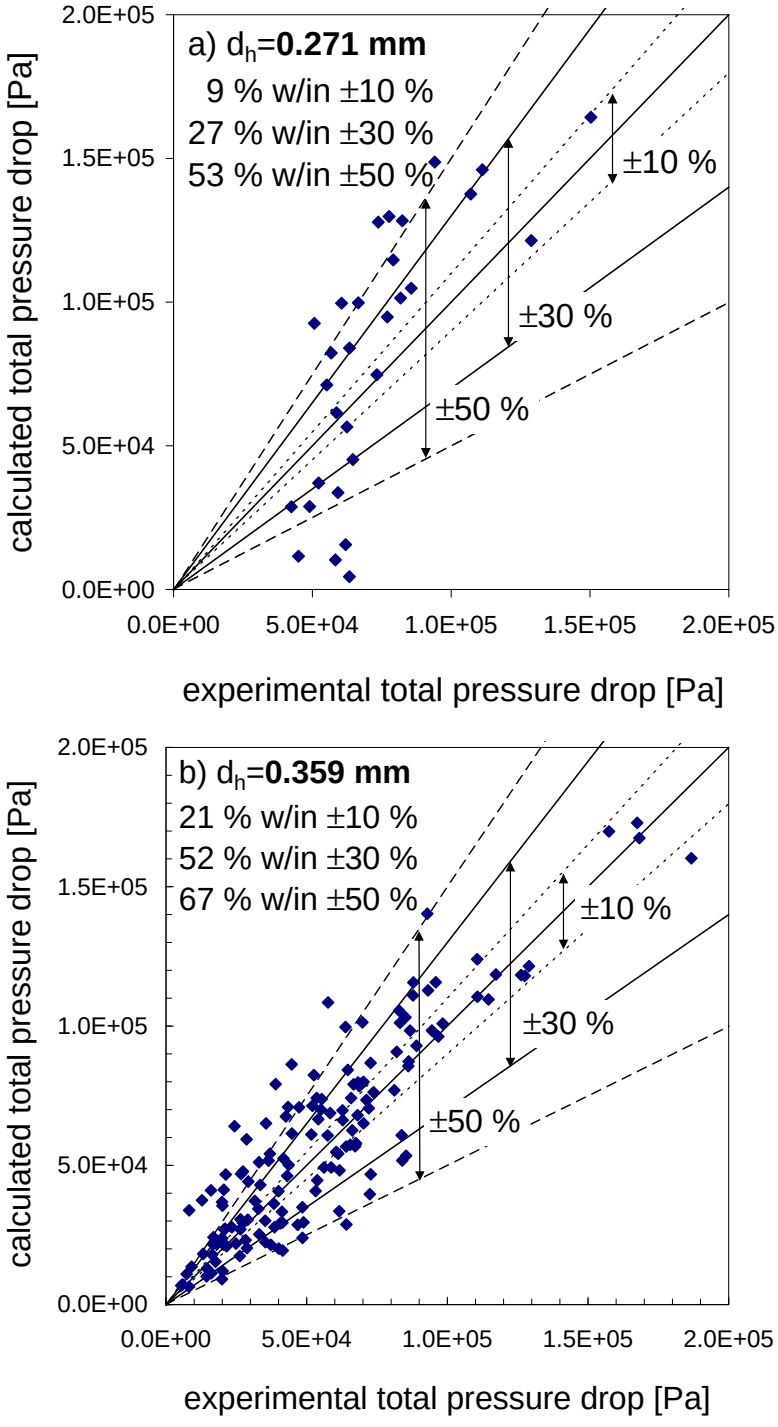

Figure 5.13: Comparison of experimental results with calculated data

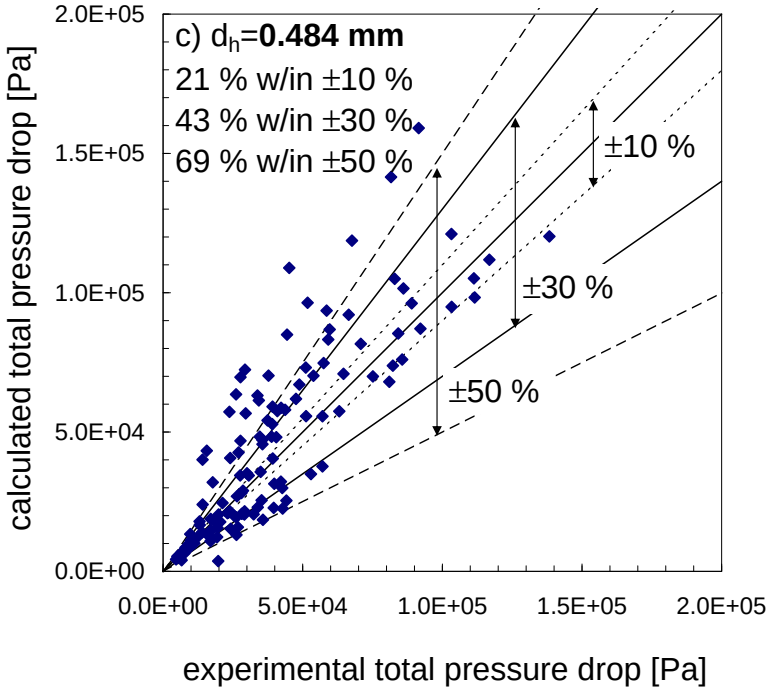

Figure 5.13: Comparison of experimental results with calculated data (continued)

The homogeneous model cannot predict the experimental results for all investigated channels with an acceptable accuracy. Using the separate flow model with constants proposed by Lockhart and Martinelli a better, but still not excellent, agreement has been obtained, Fig. 5.13a-5.13c. The experimental data were predicted with a mean absolute error (MAE) of about 35 %, Table 5.4. In this table the values given within brackets were obtained for the modified void fraction equation (Eq. 2.3 with $n_3 = 0.3$ instead of $n_3 = 0.07$ as proposed by Lockhart and Martinelli, Chapter 5.1). For the three channels there is no big difference in agreement between predictions and experimental data using either the Lockhart-Martinelli or the modified void fraction equation.

Table 5.4: Calculated data and comparison with experiments for two-phase flow

channel [mm]	MAE [%]	percentage of exp. data within		
		±10 %	±30 %	±50 %
0.271	44 (49)	9 (9)	27 (22)	53 (64)
0.359	31 (32)	21 (22)	52 (49)	67 (64)
0.484	35 (39)	21 (22)	43 (50)	69 (61)

Using the same program, the influence of frictional, acceleration and gravita-

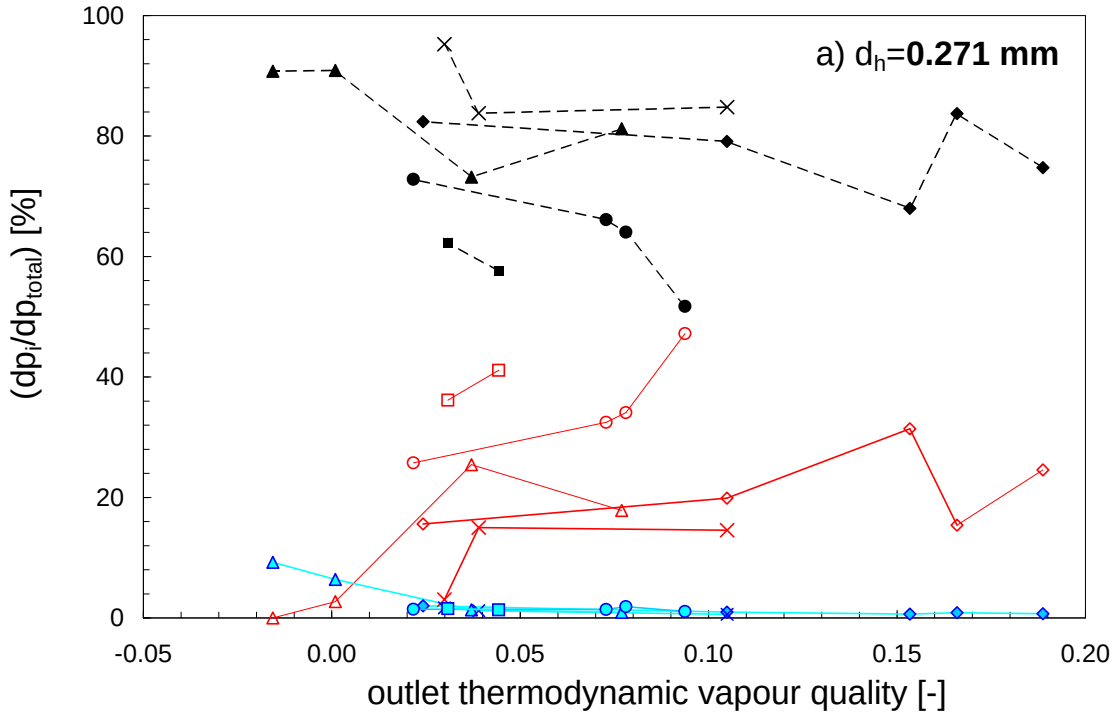

Figure 5.14: Percentage of frictional, gravitational and acceleration pressure drop of total pressure drop

tional terms ($i = f, a, g$) on the total pressure drop can be discussed. The pressure drops as a function of thermodynamic vapour quality at the channel outlet are shown in Figs. 5.14a-5.14c. Note that the legend in Fig. 5.14b is valid for all three graphs. For all channels a similar tendency has been found. The acceleration term of the pressure drop increases with increasing vapour quality. The frictional and gravitational terms of the pressure drop decrease with increasing vapour quality because of a decrease of gas viscosity and of mean density due to an increase in void fraction.
Note that the absolute value of the gravitational pressure drop stays almost constant (the same channel length and void fraction close to one in most of cases, Eq. 3.32) and the total pressure drop increases with increasing mass flux (Fig. 5.12). Therefore with decreasing mass flux the percentage of the gravitational pressure drop increases.
The frictional pressure drop is dominant in all cases (more than 50 % of total pressure drop) and therefore it can be concluded that the total pressure drop is caused mostly by shear stress.

This Chapter can be concluded by two statements. The flow boiling pressure drop in narrow channels can be predicted by a separated flow model (governing correlations (conservation of mass, energy and momentum) with the Lockhart-Martinelli method to calculate frictional two-phase pressure drop and

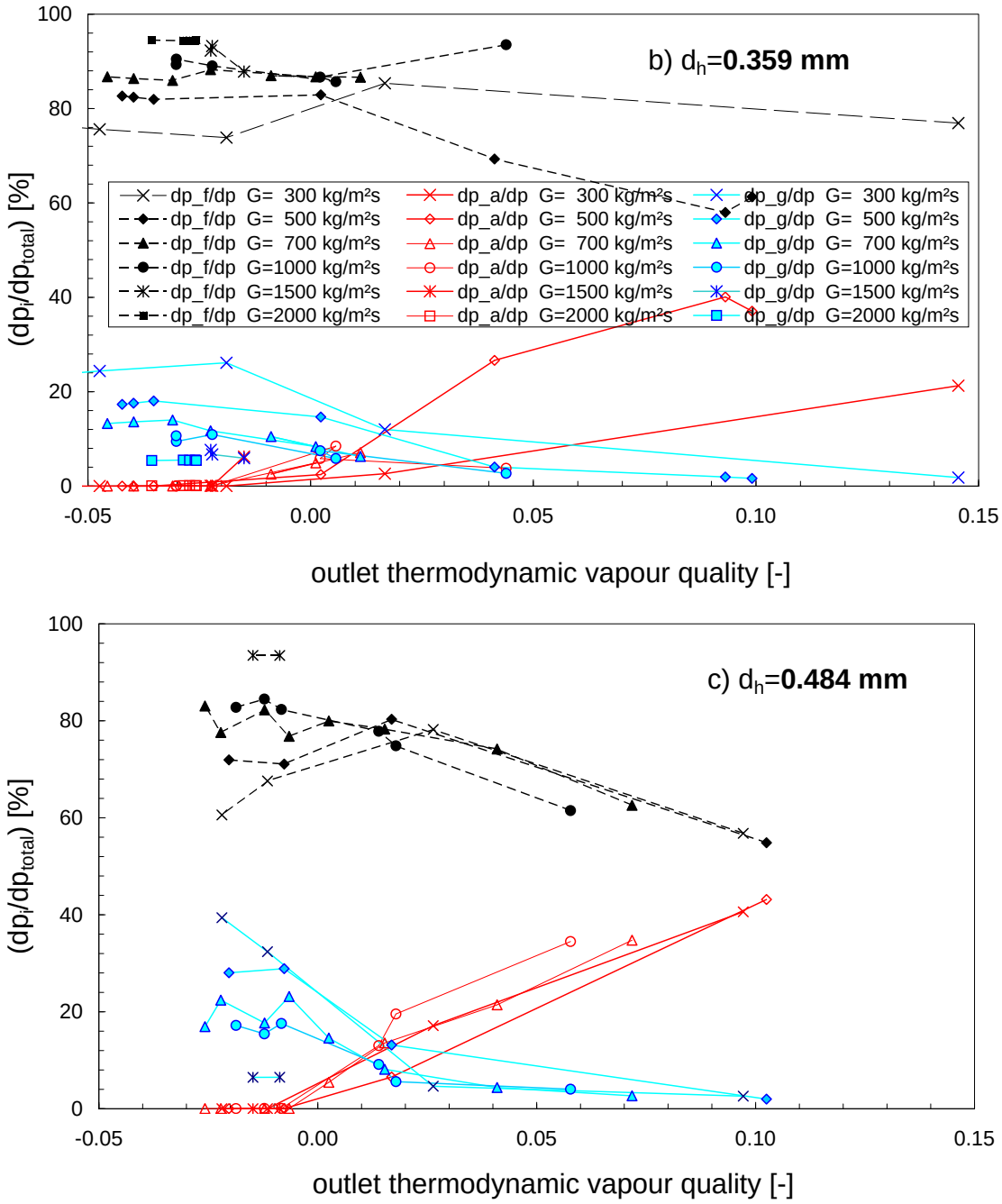

Figure 5.14: Percentage of frictional, gravitational and acceleration pressure drop of total pressure drop (continued)

empirical void fraction equation with constants proposed by Lockhart and Martinelli) with an acceptable agreement. The total pressure drop is caused mostly by shear stress.

5.3 Two-phase heat transfer

The local heat transfer coefficients were calculated according to Eq. 3.38. Figure 5.15 presents the local heat transfer coefficients vs. thermodynamic vapour quality for mass fluxes of 300, 700 and 1500 kg/m^2s for the three channels considering the whole channel length. It should be emphasised that the experiments were performed always under conditions of subcooling (see Table 4.4) at the channel inlet to guarantee only liquid flow there. The growth of bubbles and their agglomeration changes the flow pattern from bubbly to slug flow and finally to annular flow. A partial dryout close to the outlet was also observed, especially for low mass fluxes. Bubbly, slug and annular flow patterns are indicated by rhombic, circular and triangular symbols, respectively. The hatched bands show roughly the flow pattern transition ranges.

In all three channels, for given experimental conditions, the relationship between local heat transfer coefficient (Eq. 3.38) and thermodynamic vapour quality (Eqs. 3.42 and 3.43) is similar. Because of subcooled conditions at the inlet, a portion of the channel was occupied by single-phase flow with corresponding low heat transfer coefficient (this is on the left side of Fig. 5.15, the part of the curves with small slope, where there are no symbols indicated on the curves). Two-phase flow started already at negative vapour qualities for all three channels. Nucleate boiling was the dominating heat transfer mechanism where bubble growth and departure were observed. The highest local heat transfer coefficient was mostly found for slug flow. Such maxima were usually observed at thermodynamic vapour qualities close to zero and at a short distance from the position where the onset of boiling started. With the elongation of bubbles and slugs convective boiling became a considerable heat transfer mechanism. A reduction of the liquid layer thickness by evaporation led to the generation of temporary local dry-outs, causing a decrease of the local heat transfer coefficient along the channel.

It is well known that if the heat transfer coefficient increases with increasing heat flux nucleate boiling is dominant. On the other hand convective boiling is dominant if the heat transfer coefficient increases with increasing mass flux and vapour quality. In Fig. 5.15, the local heat transfer coefficient increases with heat flux (especially under saturation condition); this means that nucleate boiling is dominant. However, from flow observations (slug and annular flow, both characterised by a thin liquid layer at the wall) convective boiling would be expected at the corresponding positions.

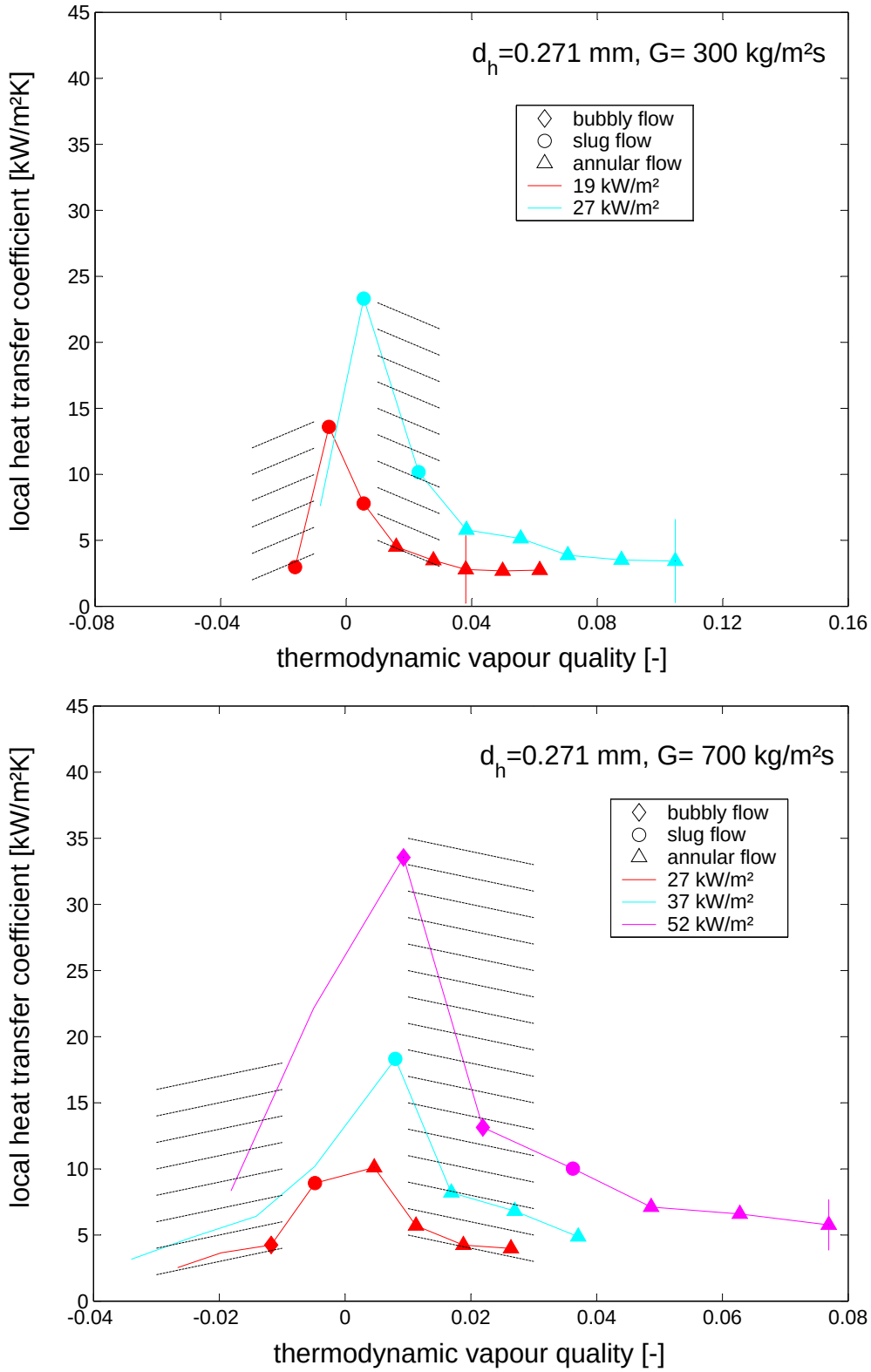

Figure 5.15: Local heat transfer coefficient

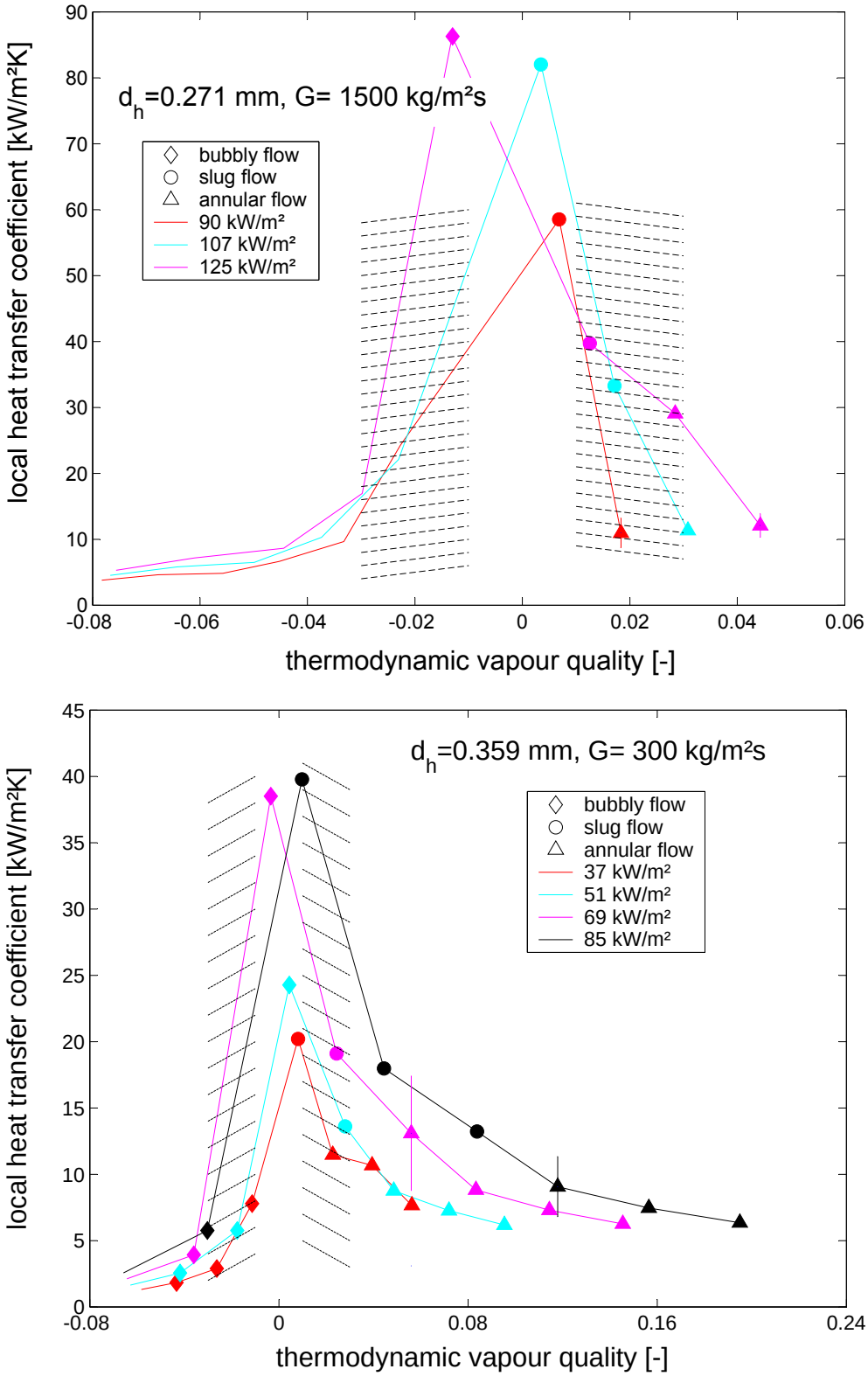

Figure 5.15: Local heat transfer coefficient (continued)

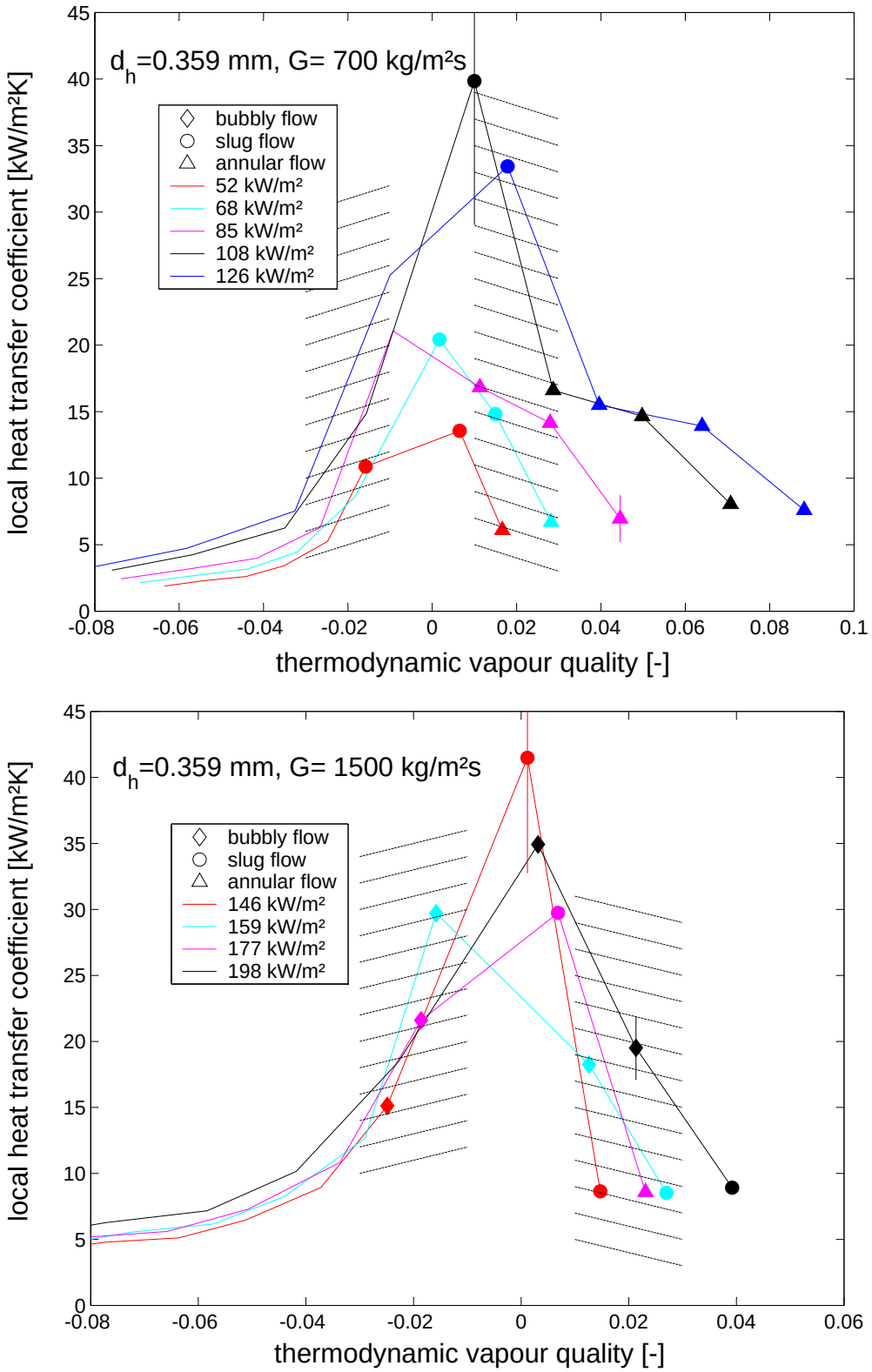

Figure 5.15: Local heat transfer coefficient (continued)

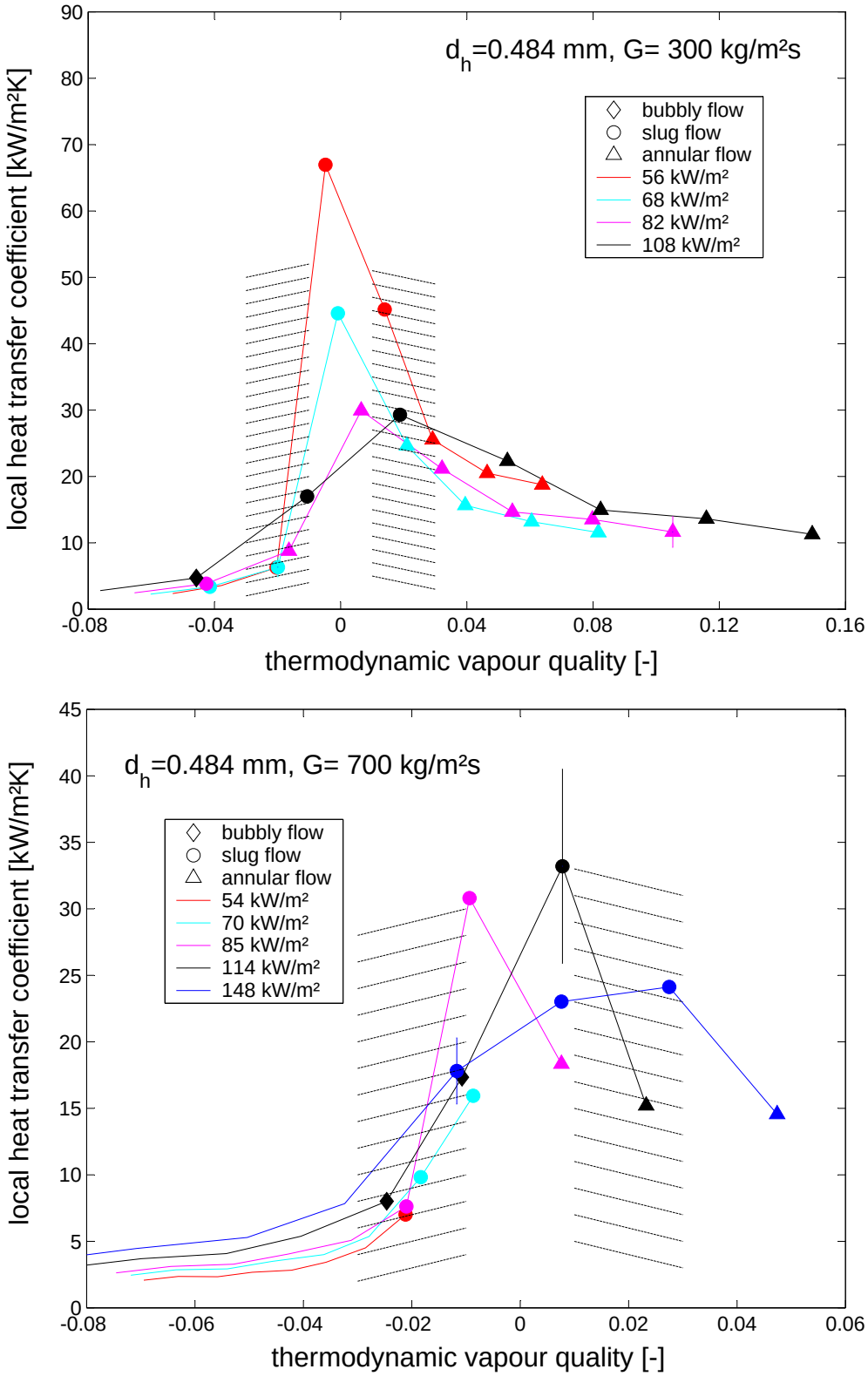

Figure 5.15: Local heat transfer coefficient (continued)

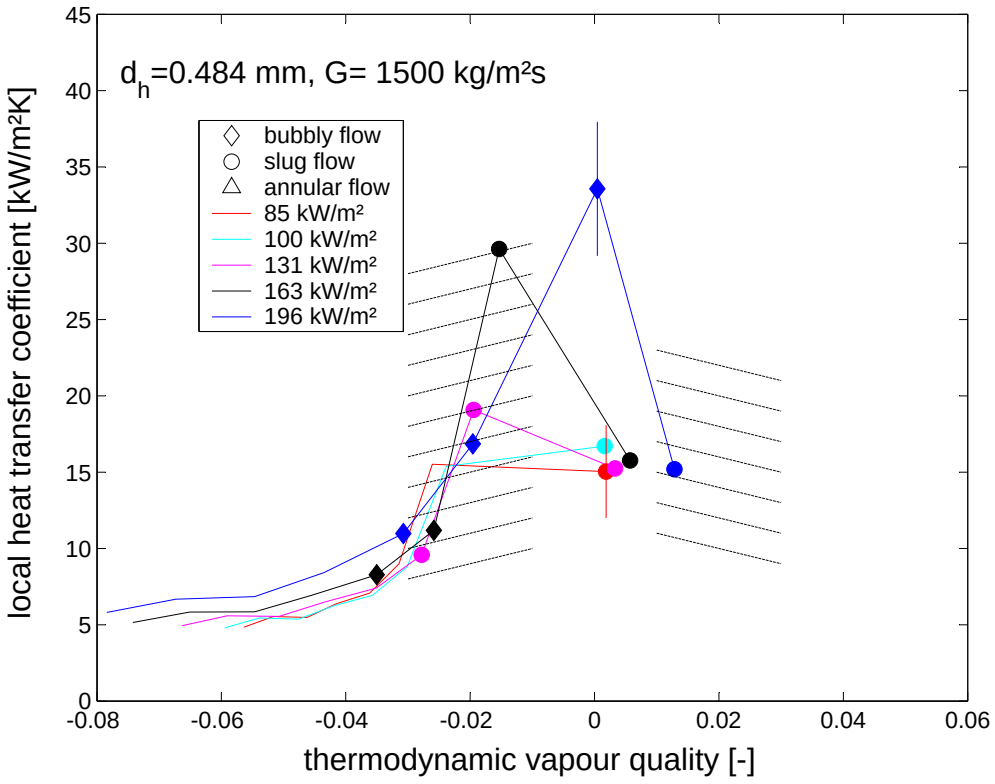

Figure 5.15: Local heat transfer coefficient

Figure 5.16 presents local heat transfer coefficients for all three channels and the following experimental conditions: $G = 300,\ 700,\ 1500\ kg/m^2s$ and $q = 34 - 198\ kW/m^2$. In this figure only the experimental points for which the dominance of one vapour body category is higher than 80 % are presented. This manipulation was applied in order to emphasize the boundary between flow pattern ranges. Bubbly flow occurred mostly for negative vapour quality and was characterised by a low heat transfer coefficient, at least for $x_{th} < -0.04$. For $x_{th} > 0.03$ annular flow was dominant with the tendency of decreasing heat transfer performance with increasing vapour quality. Slug flow was observed for thermodynamic vapour quality close to zero. Fig. 5.16 proves that the best heat transfer performance was obtained at thermodynamic vapour qualities close to zero and was associated with slug flow.

In comparison with conventional size channels, where convective boiling during annular flow offers the best heat transfer performance (Fig. 5.17), the maximum of the heat transfer performance in narrow space channels is shifted towards the inlet of the channel, where it can be assumed that nucleate boiling was the dominant heat transfer mechanism.

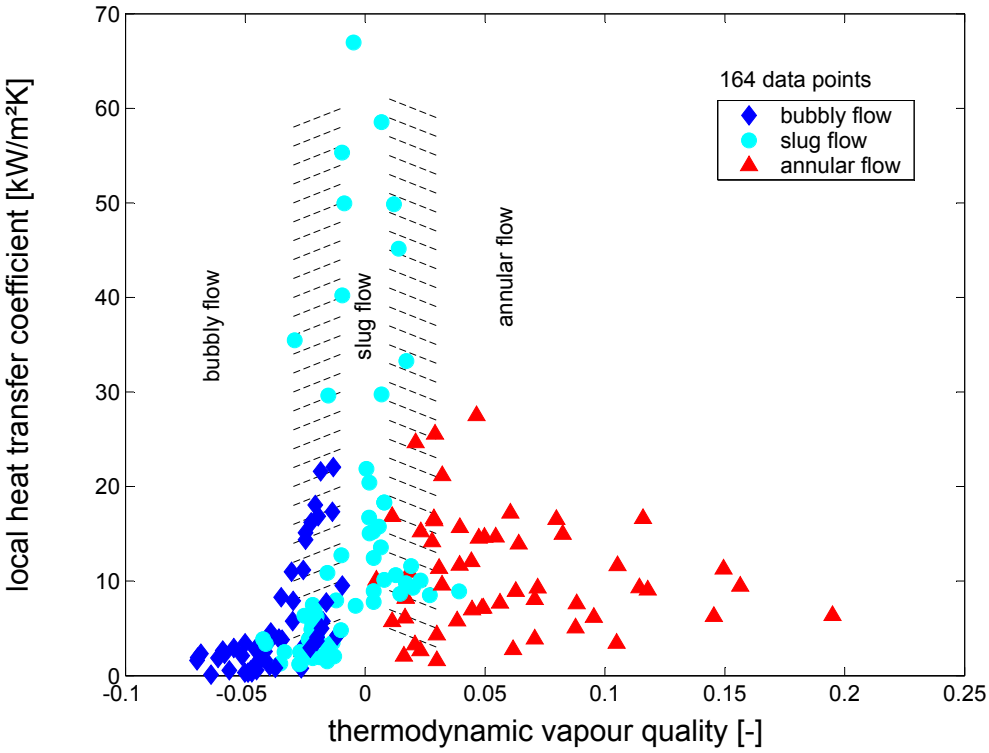

Figure 5.16: Local heat transfer coefficient for $d_h = 0.271, 0.359, 0.484\ mm$, $G = 300, 700, 1500\ kg/m^2s$ and $q = 34 - 198\ kW/m^2$

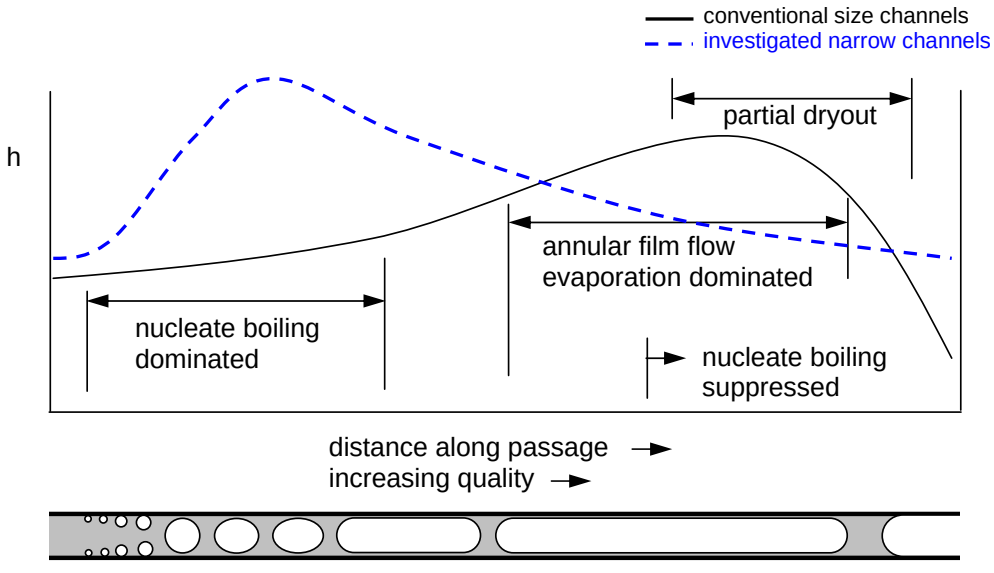

Figure 5.17: Schematic comparison between heat transfer coefficient in conventional size channels and the investigated narrow channels

The experimental results were compared with available empirical correlations under saturation conditions. In Table 5.5 the mean absolute error (MAE) and percentage of experimental data within different error ranges are presented for all checked correlations. It can be found that the agreement increases with increasing hydraulic diameter. This can be caused by the uncertainty of the results, which increases with decreasing channel size.

The best agreement was found for equations proposed by Yu et al. [81] and by Lazarek and Black [72]. These methods assume nucleation as the dominant heat transfer mechanism; this proves the dominance of nucleate boiling in the considered channels. To describe the two bigger channels (0.359 *mm* and 0.484 *mm*) the Shuai correlation, and to a lesser extent, the equation proposed by Kandlikar for nucleate boiling and the VDI-correlation can be used with somewhat smaller agreement. The Kandlikar equation has still a reasonable agreement also for the 0.271 *mm* channel.

Figs. 5.18 and 5.19 show the comparison between the experimental data and the theoretical data on the basis of the correlation of Yu et al. [81] and Lazarek and Black [72], respectively. The wide scatter of data, especially the high experimental local heat transfer coefficient, may be partly explained by mea-

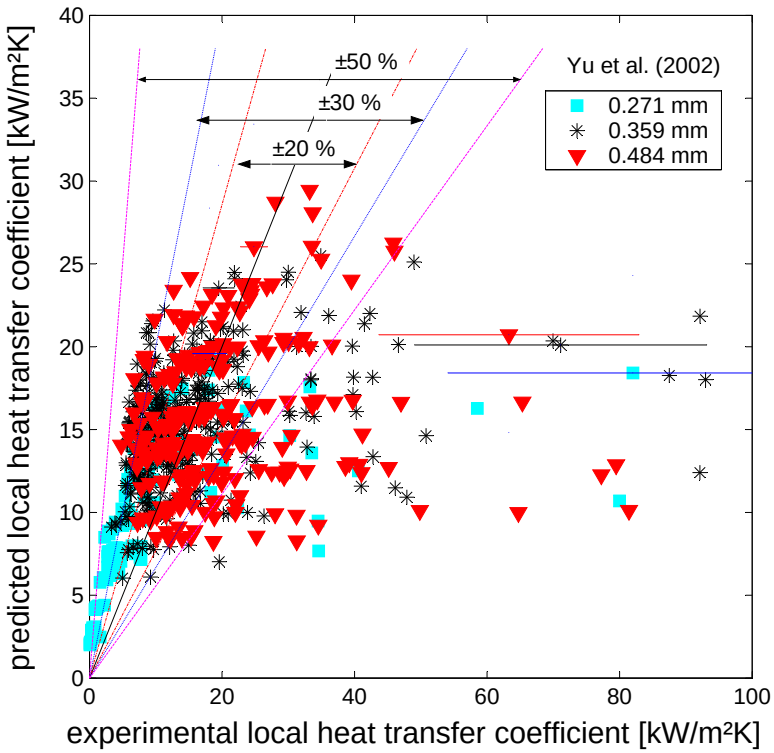

Figure 5.18: Comparison of experimental local heat transfer coefficient with the Yu et al. correlation (Eq. 2.32)

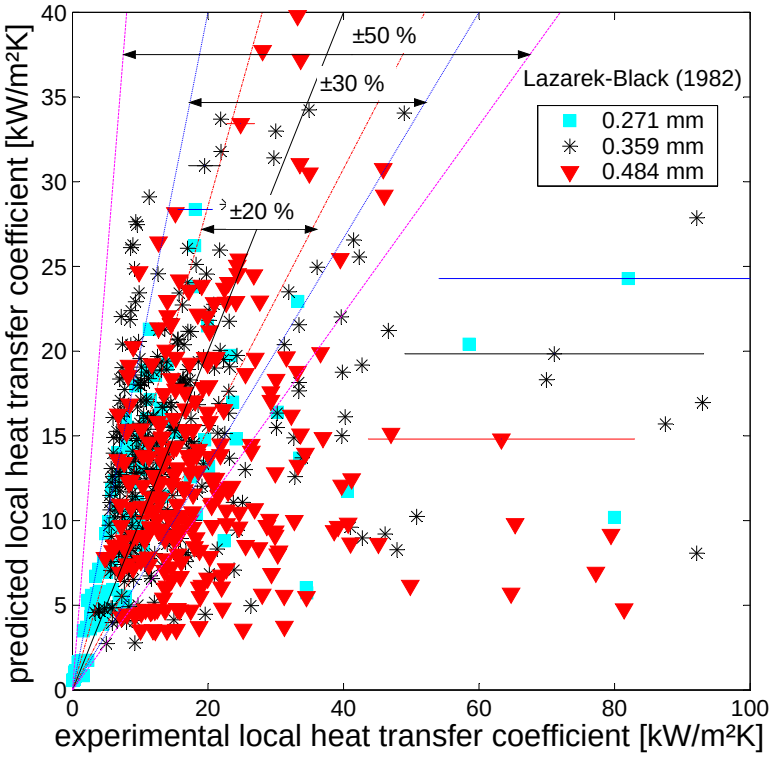

Figure 5.19: Comparison of experimental local heat transfer coefficient with the Lazarek and Black correlation (Eq. 2.28)

surement uncertainties.

Table 5.5: Comparison of experimental local heat transfer data with results from empirical correlations

		MAE [%]	percentage of experimental data within		
			± 20 %	± 30 %	± 50 %
Chen, 1966 [67]	0.271 mm	5118	2.50	4.17	7.5
	0.359 mm	525	4.15	6.71	15.65
	0.484 mm	452	10.12	17.00	29.96
Lazarek and Black, 1982 [69]	**0.271 mm**	**70**	**18.33**	**35.00**	**74.17**
	0.359 mm	**49**	**28.43**	**43.45**	**67.41**
	0.484 mm	**44**	**23.89**	**34.41**	**47.77**
Kandlikar, 1990 [76]	0.271 mm	576	5.00	6.67	12.50
	0.359 mm	338	6.07	9.90	25.24
	0.484 mm	151	14.98	21.86	40.49
Kandlikar, only NBD, 1990 [76]	0.271 mm	189	10.00	15.00	36.67
	0.359 mm	85	21.09	30.67	60.70
	0.484 mm	56	19.43	28.74	48.18
VDI-Wärmeatlas, 1997 [68]	0.271 mm	815	5.00	9.17	23.33
	0.359 mm	85	18.85	28.11	49.20
	0.484 mm	46	19.03	29.15	41.70
Yu et al., 2002 [78]	**0.271 mm**	**181**	**16.67**	**28.33**	**54.17**
	0.359 mm	**51**	**30.03**	**43.77**	**70.61**
	0.484 mm	**39**	**31.98**	**46.15**	**67.21**
Warrier et al., 2002 [72]	0.271 mm	2639	3.33	5.00	9.17
	0.359 mm	157	6.07	10.86	32.91
	0.484 mm	52	30.77	46.15	79.35
Shuai, 2004 [79]	0.271 mm	709	10.00	17.50	40.00
	0.359 mm	77	20.45	37.38	70.29
	0.484 mm	41	41.70	57.89	79.76

Chapter 6

Summary and conclusions

The main goal of the work was to find the circumstances for which the heat transfer in narrow channels (microchannels) is most efficient as well as to verify the validity of correlations for conventional-size channels for smaller scale channels, in our case $0.289x0.255\ mm^2$ ($d_h = 0.271\ mm$), $0.550x0.266\ mm^2$ ($d_h = 0.359\ mm$) and $0.807x0.349\ mm^2$ ($d_h = 0.484\ mm$). Diabatic two-phase flow in three vertical rectangular narrow channels was investigated. Water was used as the working fluid. The areas of interest were: 1) visualisation of the two-phase flow and identification of flow patterns; 2) measurement of pressure drop and comparison with existing correlations; 3) investigation of heat transfer coefficient and comparison with existing correlations. Adiabatic single-phase flow (liquid only) investigations were used in order to calibrate the test-rig. In order to determine heat loss functions (used to estimate the heat loss for two-phase flow), diabatic single-phase experiments were performed.

Visualisation

High-speed videos were recorded at every thermocouple position along the channel axis, when two-phase flow was observed there. During the image evaluation a relatively big human error occurred, so the visualisation results are more of qualitative nature.

The main goal of visualisations was to define flow patterns for given conditions (hydraulic diameter, mass and heat flux) along the channel axis in order to obtain a better understanding of the heat transfer mechanism. For all three channels ($d_h = 0.271\ mm$, $d_h = 0.359\ mm$,$d_h = 0.484\ mm$) and three mass fluxes (300, 700 and 1500 kgm^2s) the number of vapour bodies, their velocities and lengths were directly and/or indirectly obtained from video recordings.

Three basic flow patterns were distinguished: bubbly, slug and annular flow. Because for the present visualisation a typical annular flow was not observed

(there were always some liquid bridges which interrupted the vapour core), the slug-annular transition had to be assumed and as a criterion the mass flux influence was used. Finally annular flow was defined as flow with extended vapour slugs, where the slugs are not influenced by the mass flux. In consequence, a flow with vapour slugs longer than fifty times the channel width is defined as annular flow in this study. In general, for a given position more than one type of vapour body was observed. In this case, flow patterns were defined according to the dominant flow type by means of histograms.

No distinguishable differences between the same flow patterns were observed in the three investigated channels.

The velocity of a vapour body increases with its increasing length up to a certain value, depending on experimental conditions, and then remains unchanged. The velocity of the vapour body at its top is usually higher than that at its bottom which is mostly due to evaporation (vapour slug growth).

Experimental void fractions were compared with results from the empirical equation (Eq. 3.35) with constants proposed by Lockhart and Martinelli. In order to improve the agreement, a modification of the exponent of the viscosity term (n_3) in this correlation was made.

None of the obtained flow pattern transition boundaries could describe the experimental data precisely.

Pressure drop

The pressure drop was measured for all experiments. The single-phase data bank was enlarged by experimental results obtained at two independent institutes (ENEA, KTH). For all cases (single- and two-phase flow) the experimental results were compared with predictions given by classical theory.

For single-phase flow, an evaluation of the frictional pressure drop in microconduits was carried out. Taking into consideration such quantities as channel (hydraulic) diameter (from 0.259 to 1.699 mm), shape (circular, rectangular) and aspect ratio, inclination, working fluid (water and R-134a) and heat input, it was found that the Hagen-Poiseuille and the Blasius equation can describe the friction factor well (Appendix A). The IKE-experimental results were used for validation of the test section.

The flow boiling pressure drop investigations can be concluded by two statements. The flow boiling pressure drop in narrow channels can be predicted by a separate flow model, which is based on governing equations (conservation of mass, energy and momentum). The momentum equation was used as a total pressure drop correlation. Within it, three pressure drop terms can be

distinguished: frictional, acceleration and gravitational pressure drop. To calculate the frictional two-phase pressure drop, the Lockhart-Martinelli method was used. In order to solve the whole set of equations, the void fraction value is required. There was no measurement of this parameter and therefore the empirical void fraction equation with constants proposed by Lockhart and Martinelli was used. It can be concluded that the flow boiling pressure drop can be described by the aforementioned separate flow model quite well.

The character of the pressure drop was investigated, viz. the influence of frictional, acceleration and gravitational terms on the total pressure drop was checked. The total pressure drop is caused mostly by shear stress, because the frictional pressure drop is dominant in all cases (more than 50 % of the total pressure drop).

Heat transfer

Flow boiling is complicated by the fact that, simultaneously with a change of flow patterns, different vaporisation mechanisms are encountered at different positions along the channel. The boiling of refrigerants in small-diameter channels can be dominated by nucleate boiling, by convective boiling, or both mechanisms.

The highest local heat transfer coefficient was found mostly for slug flow. Such maxima were usually observed at thermodynamic vapour qualities close to zero and at a short distance from the position where the onset of boiling started. With the elongation of bubbles and vapour slugs convective boiling became a considerable heat transfer mechanism. A reduction of the liquid layer thickness by evaporation at higher vapour quality led to the generation of temporary local dry-outs, causing a decrease of the local heat transfer coefficient along the channel.

The local heat transfer coefficient increases with heat flux (especially under saturation conditions); this would suggest that nucleate boiling is dominant. However, flow observations show predominantly slug and annular flow and this would let us expect convective boiling at the corresponding positions.

The local heat transfer coefficients (under saturation conditions) were compared with eight empirical correlations. The best agreement was found for equations proposed by Yu et al. [81] and by Lazarek and Black [72].

Further investigations?

Based on the experience gained from the experiments and data evaluation, some hints regarding further work can be given as follows:

- The estimation of the heat loss for two-phase flow should be more accurate. The two-phase heat transfer coefficient error is caused mostly by this uncertainty.
- It would be optimal to observe the flow patterns along the whole length of the channel simultaneously. This could give the possibility to observe nucleation, bubble growth, departure and growth of every vapour body.
- A local pressure measurement would allow to find the exact fluid pressure profile (and hence the fluid temperature profile in the saturation region).
- In the thesis only two-dimensional visualisation was possible. The problem with illumination lead sometimes to not very clear pictures. An improvement of the illumination system or any change of the test section which allows for a better illumination would be required in further work.
- Because nucleate boiling seems to be the best heat transfer mechanism, this process should be especially investigated in great detail. On the other hand, the occurrence of dryout areas (for which the heat transfer performance is worst) is also a useful investigation area.

The thesis can be concluded with the following statements:

The best heat transfer performance was found at thermodynamic vapour qualities close to zero. The checked heat transfer coefficient correlations from the literature are not able to predict the experimental data very well.

Slug flow is observed simultaneously with the best heat transfer performance.

The accompanying high pressure drop can be well described by conventional correlations (governing equations: conservation of mass, energy and momentum, the Lockhart-Martinelli method and the empirical void fraction correlation with constants given by Lockhart and Martinelli).

Bibliography

[1] M.B. Bowers and I. Mudawar. High flux boiling in low flow rate, low pressure drop mini-channel and micro-channel heat sinks. *Int. J. Heat Mass Transfer*, 3(2):321–334, 1994.

[2] K. Azar. The history of power dissipation. *Electronics Cooling*, 6(1), 2000.

[3] K. Azar. Cooling technology options, Part 1. *Electronics Cooling*, 9(4), 2003.

[4] R.E. Simons. Direct liquid immersion cooling for higher power density microelectronics. *Electronics Cooling*, 2(2), 1996.

[5] S. Lin, K. Sefiane, and J.R.E. Christy. Prospects of confined flow boiling in thermal management of microsystems. *Applied Thermal Engineering*, 22:825–837, 2002.

[6] R.C. Chu. A review of IBM sponsored research and development projects for computer cooling. 15^{th} *IEEE Semi-Therm Symposium, San Diego, USA*, pages 151–165, 1999.

[7] Y. Chen. *Enhanced Boiling of Hydrocarbon Mixtures - Heat Transfer and Bubble Dynamics*. PhD thesis, University of Stuttgart, 2004.

[8] T.A. Grimley, I. Mudawar, and F.P. Incropera. Limits to critical heat flux enhancement in a liquid film falling over a structured surface that simulates a microelectronic chip. *Transactions of ASME, Journal of Heat Transfer*, 110:535–538, 1988.

[9] F.P. Incropera and D. DeWitt. *Fundamentals of Heat and Mass Transfer*. John Wiley Sons, New York, 2002.

[10] D.T. Vader, G.M. Chrysler, R.C. Chu, and R.E. Simons. Experimental investigation of subcooled liquid nitrogen impingement cooling. *IEEE Transactions, CPMT-Part A*, 18(4):788–794, 1995.

[11] G.M. Chrysler, R.C. Chu, and R.E. Simons. Jet impingement boiling of a dielectric coolant in narrow gaps. *IEEE Transactions CPMT-Part A*, 18(3):527–533, 1995.

[12] K. Azar. Cooling technology options, Part 2. *Electronics Cooling*, 9(4), 2003.

[13] S. Godfrey. An introduction to thermoelectric coolers. *Electronics Cooling*, 2(3), 1996.

[14] S. Khandekar. *Thermo-hydrodynamics of Closed Loop Pulsating Heat Pipe*. PhD thesis, University of Stuttgart, 2004.

[15] J. Kirshberg, K.L. Yerkes, and D. Liepmann. Demonstration of a micro-CPL based on MEMS fabrication technologies. 35^{th} *Intersociety Energy Conversion Engineering Conference and Exhibition, Las Vegas, NV, USA*, 2:1198–1204, 2000.

[16] Yu.F. Maydanik. Loop heat pipes. *Applied Thermal Engineering*, 25:635–657, 2005.

[17] Y. Chen and P. Cheng. Heat transfer and pressure drop in fractal tree-like microchannel nets. *Int. J. Heat Mass Transfer*, 45:2643–2648, 2002.

[18] T.M. Harms, M.J. Kazmierczak, and F.M. Gerner. Developing convective heat transfer in deep rectangular microchannels. *Int. J. Heat Fluid Flow*, 20:149–157, 1999.

[19] W. Qu and I. Mudawar. Experimental and numerical study of pressure drop and heat transfer in a single-phase micro-channel heat sink. *Int. J. Heat Mass Transfer*, 45:2549 – 2565, 2002.

[20] B. Agostini, B. Watel, A. Bontemps, and B. Thonon. Friction factor and heat transfer coefficient of R134a liquid flow in mini-channels. *Applied Thermal Engineering*, 22:1821–1834, 2002.

[21] W. Qu and I. Mudawar. Measurement and prediction of pressure drop in two-phase micro - channel heat sink. *Int. J. Heat Mass Transfer*, 46:2737–2753, 2003.

[22] B. Agostini and A. Bontemps. Vertical flow boiling of refrigerant R134a in small channels. *Int. J. Heat and Fluid Flow*, 26:296–306, 2004.

[23] P.A. Kew and K. Cornwell. Confined bubble flow and boiling in narrow spaces. 10^{th} *Int. Heat Transfer Conf., Brighton, UK*, 7:473–478, 1994.

[24] G.P. Celata. *Heat Transfer and Fluid Flow in Microchannels*. Begell House, 2004.

[25] W. Fritz. Berechnung des Maximalvolumens von Dampfblasen. *Phys. Z.*, 36:379–388, 1935.

[26] S.S. Mehendale, A.M. Jacobi, and R.K. Shah. Heat exchangers at micro and meso-scale. *Proc. Int. Conf. Process Industries, Ed. R.K.Shah, NY, Begell, House, Inc.*, pages 55–74, 1999.

[27] S.G. Kandlikar. Fundamental issues related to flow boiling in minichannels and microchannels. *Experimental Thermal and Fluid Science*, 26:389–407, 2002.

[28] D.M. Tuckerman and R.F.W. Pease. High-performance heat sinking for VLSI. *IEEE Electron Device Lett.*, 2(5):126–129, 1981.

[29] G. Hetsroni, A. Mosyak, E. Pogrebnyak, and L.P. Yarin. Fluid flow in micro-channels. *Int. J. Heat Mass Transfer*, 48:1982–1998, 2005.

[30] G. Hetsroni, A. Mosyak, E. Pogrebnyak, and L.P. Yarin. Heat transfer in micro-channels: Comparison of experiments with theory and numerical results. *Int. J. Heat Mass Transfer*, 48:5580–5601, 2005.

[31] Z.-Y. Guo. Size effect on flow and heat transfer characteristics in MEMS. *Int. Conf. on Heat Transfer and Transport Phenomena in Microscale, Banff, Canada*, pages 24–31, 2000.

[32] G.M. Mala, D. Li, and J-D. Dale. Heat transfer and fluid flow in microchannels. *Int. J. Heat Mass Transfer*, 40(13):3079–3088, 1997.

[33] C. Yang, D. Li, and J.H. Masliyah. Modeling forced liquid convection in rectangular microchannels with electrokinetic effects. *Int. J. Heat Mass Transfer*, 41:4229–4249, 1998.

[34] L. Ren, W. Qu, and D. Li. Interfacial electrokinetic effects on liquid flow in microchannels. *Int. J. Heat Mass Transfer*, 44:3125–3134, 2001.

[35] J. Yang and D.Y. Kwok. Analytical treatment of electrokinetic microfluidics in hydrophobic microchannels. *Analytica Chimica Acta*, 507:39–53, 2004.

[36] D.C. Tretheway and C.D. Meinhart. Apparent fluid slip at hydrophobic microchannel walls. *Physic of Fluids*, 14:9–12, 2002.

[37] H.Y. Wu and P. Cheng. An experimental study of convective heat transfer in silicon microchannels with different surface conditions. *Int. J. Heat Mass Transfer*, 46:2547–2556, 2003.

[38] D.B.R. Kenning and Y. Yan. Saturated flow boiling of water in a narrow channel: Experimental investigation of local phenomena. *Trans IChemE*, 79, Part A:425–436, 2001.

[39] G. Marazana, I. Perry, and D. Maillet. Mini- and micro-channels: Influence of axial conduction in the walls. *Int. J. Heat Mass Transfer*, 47:3993–4004, 2004.

[40] Van P. Carey. *Liquid-Vapour Phase-Change Phenomena*. Taylor & Francis, 1992.

[41] B.K. Kozlov. Forms of flow of gas-liquid mixtures and their stability limits in vertical tubes. *Associated Technical Services Translation 136R. Translated from Zh. Tekh. Fiz.*, 24:2285–2288, 1954.

[42] A.W. Bennett, G.F. Hewitt, H.A. Kearsey, R.K.F. Keeys, and P.M.C. Lacey. Flow visualisation studies of boiling at high pressure. *Symposium on boiling heat transfer in steam generating units and heat exchangers, Manchester, UK*, 1965.

[43] K. Cornwell and P.A. Kew. Boiling in small parallel channels. *CEC Conf. on Energy Efficiency in Process Technology, Athens, Greece, Paper 22, Elsevier Applied Sciences*, 1992.

[44] J. Bonjour and M. Lallemand. Flow patterns during boiling in a narrow space between two vertical surfaces. *Int. J. Multiphase Flow*, 24:947–960, 1998.

[45] Z. Feng and A. Serizawa. Two-phase flow patterns in ultra-small channels. 2^{nd} *Japanese-European Two-Phase Flow Meeting , Tsukuba, Japan*, 2000.

[46] O. Baker. Simultaneous flow of oil and gas. *Oil Gas J.*, 53(185), 1954.

[47] P.B. Whalley. *Two-Phase Flow and Heat Transfer*. Oxford University Press, 1996.

[48] D.S. Scott. Properties of co-current gas-liquid flow. *Advances in Chemical Engineering*, 4:199–277, 1963.

[49] G.F. Hewitt and D.N. Roberts. Studies of two-phase flow patterns by simultaneous flash and x-ray photography. *AERE-M2159*, 1969.

[50] Y. Taitel, D. Barnea, and A.E. Dukler. Modelling flow pattern transitions for steady upward gas-liquid flow in vertical tubes. *AIChE Journal*, 26(3):345–354, 1980.

[51] K. Mishima and M. Ishii. Flow regime transition criteria for upward two-phase flow in vertical tubes. *Int. J. Heat Mass Transfer*, 27(5):723–737, 1984.

[52] M. Ishii. One-dimensional drift-flux model and constitutive equations for relative motion between phases in various two-phase flow regimes. *ANL Report ANL-77-47*, 1977.

[53] S. Lin, P.A. Kew, and K. Cornwell. Characteristics of air/water flow in small tubes. *Heat and Technology, Calore e Tecnologia*, 17(2):63–70, 1999.

[54] A. Tabatabai and A. Faghri. A new two-phase flow map and transition boundary accounting for surface tension effects in horizontal miniature and micro tubes. *J. Heat Transfer*, 123:958–968, 2001.

[55] D. Steiner. *Zweiphasenströmung in Apparateelementen*. Hochschulkurs Wärmeübertragung II. Forschungs-Gesellschaft Verfahrenstechnik e.V. Düsseldorf, 1983.

[56] O. Zürcher, D. Favrat, and J.R. Thome. Development of a diabatic two-phase flow pattern map for horizontal flow boiling. *Int. J. Heat Mass Transfer*, 45:291–301, 2002.

[57] A.-M. Morgante and J. Fabre. Two-phase flow in square mini-channels: Flow pattern transition. 3^{rd} *Int. Conf. on Microchannels and Minichannels, Toronto, Ontario, Canada*, 2005.

[58] R.W. Lockhart and R.C. Martinelli. Proposed correlation of data for isothermal two-phase, two-component flow in pipes. *Chemical Engineering Progress*, 45(1):39–48, 1949.

[59] J.G. Collier and J.R. Thome. *Convective Boiling and Condensation.* 3^{rd} *Edition*. Clarendon Press, Oxford, 1994.

[60] Y-Y. Yan and T-F. Lin. Evaporation heat transfer and pressure drop of refrigerant R134a in a small pipe. *Int. J. Heat Mass Transfer*, 41:4183–4194, 1998.

[61] S.M. Zivi. Estimation of steady state steam void fraction by means of the principle of minimum entropy production. *J. Heat Transfer*, 86:247–252, 1964.

[62] D.S. Wen and D. Kenning. Two-phase pressure drop of water during flow boiling in a vertical narrow channel. *Experimental Thermal and Fluid Science*, 28:131–138, 2004.

[63] K. Mishima, T. Hibiki, and H. Nishihara. Some characteristics of gas-liquid flow in narrow rectangular ducts. *Int. J. Multiphase Flow*, 19(1):115–124, 1993.

[64] J. Shuai, R.Kulenovic, and M. Groll. Heat transfer and pressure drop for flow boiling of water in narrow vertical rectangular channels. *Therm. Sci. Eng.*, 11(6):73–81, 2003.

[65] J.-S. Kim, K.-T. Lee, J.-H. Kim, S.-J. Ha, and Y.-B. Im. A relation between two-phase pressure drop and flow distribution in a compact heat exchanger header. 2^{nd} *Int. Conf. on Microchannels and Minichannels, Rochester, New York, USA*, pages 413–420, 2004.

[66] L. Friedel. Improved friction pressure drop correlations for horizontal and vertical two-phase pipe flow. *European Two-Phase Flow Group Meeting, Ispra, Italy*, (Paper E2), 1979.

[67] H.J. Lee and S.Y. Lee. Pressure drop correlation of two-phase flow within horizontal rectangular channels with small heights. *Int. J. Multiphase Flow*, 27:783–796, 2001.

[68] M. Kawahara, M. Sadatomi, K. Okayama, and M. Kawaji. Effects of liquid properties on pressure drop of two-phase gas-liquid flows through a microchannel. *Therm. Sci. Eng.*, 11:25–33, 2003.

[69] K. Mishima and T. Hibiki. Some characteristics of air-water two-phase flow in small diameter vertical tubes. *Int. J. Multiphase Flow*, 22(4):703–712, 1996.

[70] J.C. Chen. A correlation of boiling heat transfer to saturated fluids in convective flow. *Industrial and Engineering Chemistry Process Design and Development*, 5:322–329, 1966.

[71] *VDI-Wärmeatlas*. Verein Deutscher Ingenieure, VDI-Gesellschaft Verfahrenstechnik und Chemieingenieurwesen, Hbb, 1997.

[72] G.M. Lazarek and S.H. Black. Evaporative heat transfer, pressure drop and critical heat flux in a small vertical tube with R113. *Int. J. Heat Mass Transfer*, 25(7):945–960, 1982.

[73] M.W. Wambsganss, D.M. France, J.A. Jendrzejczyk, and T.N. Tran. Boiling heat transfer in a horizontal small-diameter tube. *J. Heat Transfer*, 115:963–972, 1993.

[74] T.S. Ravigururajan. Impact of channel geometry on two-phase flow heat transfer characteristics of refrigerants in microchannel heat exchangers. *J. Heat Transfer*, 120:485–491, 1998.

[75] G.R. Warrier, T. Pan, and V.K. Dhir. Heat transfer and pressure drop in narrow rectangular channels. 4^{th} *Int. Conf. on Multiphase Flow, New Orleans, Louisiana, USA*, 2001.

[76] M.E. Steinke and S.G. Kandlikar. Flow boiling and pressure drop in parallel flow microchannels. 1^{st} *Int. Conf. on Microchannels and Minichannels, Rochester, New York, USA*, pages 567–578, 2003.

[77] S. Lin and P.A. Kew. Characteristic of two-phase flow and heat transfer in small tubes. 6^{th} *UK Conference on Heat Transfer, Edinburgh, UK*, pages 185–190, 1999.

[78] T.-H. Yen, N. Kasagi, and Y. Suzuki. Forced convective boiling heat transfer in microtubes at low mass and heat fluxes. *Symp. on Compact Heat Exchangers,Grenoble, France*, pages 401–406, 2002.

[79] S.G Kandlikar. A general correlation for two-phase flow boiling heat transfer coefficient inside horizontal and vertical tubes. *J. Heat Transfer*, 22:219–228, 1990.

[80] T.N. Tran, M.W. Wambsganss, and D.M. France. Small circular- and rectangular-channel boiling with two refrigerants. *Int. J. Multiphase Flow*, 22(3):485–498, 1996.

[81] W. Yu, D.M. France, M.W. Wambsganss, and J.R. Hull. Two-phase pressure drop, boiling heat transfer and critical heat flux to water in small diameter horizontal tube. *Int. J. Multiphase Flow*, 28:927–941, 2002.

[82] J. Shuai. *Flow boiling heat transfer in narrow vertical channels*. PhD thesis, University of Stuttgart, 2004.

[83] R.K. Shah. Laminar flow friction and forced convection heat transfer in ducts of arbitrary geometry. *Int. J. Heat Mass Transfer*, 18:849–862, 1975.

[84] M.C. Diaz, H. Boye, I. Hapke, J. Schmidt, Y. Staate, and Z. Zhekov. Flow boiling in mini and microchannels. 2^{nd} *Int. Conf. on Microchannels and Minichannels, Rochester, New York, USA*, pages 445–452, 2004.

[85] S. Lin, P.A. Kew, and K. Cornwell. Two-phase heat transfer to a refrigerant in a 1 mm diameter tube. *Int. J. Refrigeration*, 24:51–56, 2001.

[86] C. Vlasie, H. Macchi, J. Guilpart, and B. Agostini. Flow boiling in small diameter channels. *Int. J. Refrigeration*, 27:191–201, 2004.

[87] F.M. White. *Fluid Mechanics,* 5^{th} *Edition*. McGrawHill, 2003.

[88] Y. Chin, M.S. Lakshminarasimhan, Q. Lu, D.K. Hollingsworth, and L.C. Witte. Convective heat transfer in vertical asymmetrically heated narrow channels. *J. Heat Transfer*, 124:1019–1025, 2002.

[89] D. Butterworth. A comparison of some void-fraction relationships for co-current gas-liquid flow. *Int. J. Multiphase Flow*, 1:845–850, 1975.

[90] R. Koch and A. Noworyta. *Procesy Mechaniczne w Inżynierii Chemicznej*. Wydawnictwo Naukowo Techniczne, Warszawa, 1998.

[91] S.C. Mohapatra. An overview of liquid coolants for electronics cooling. *Electronics Cooling*, 12(2), 2006.

[92] E.R. Hosler. Flow patterns in high pressure two-phase (steam-water) flow with heat addition. *Chem. Engng. Prog. Symp.*, Ser. 64 (82), 54, 1968.

[93] G.P. Celata, K. Chmiel, R. Kulenovic, C. Martin-Callizo, S. McPhail, R. Mertz, W. Owhaib, B. Palm, E. Sobierska, and G. Zummo. Frictional pressure drop in single-phase flow in narrow channels. 4^{th} *Int. Conf. on Nanochannels, Microchannels and Minichannels, Limerick, Ireland*, 2006.

[94] R.K. Shah and A.L. London. *Laminar Flow Forced Convection in Ducts*. Academic Press, 1978.

[95] S. Kakac, R.K. Shah, and W. Aungand. *Handbook of Single-Phase Convective Heat Transfer*. John Wiley and Sons, 1987.

[96] W. Tong, A.E. Bergles, and M. Jensen. Pressure drop with highly sub-cooled flow boiling in small-diameter tubes. *Experimental Thermal and Fluid Science*, (15):202–212, 1997.

[97] S.J. Kline and F.A. McClintock. Describing uncertainties in single-sample experiments. *Mechanical Engineering*, 75:3–8, 1953.

[98] R.F. Moffat. Describing the uncertainties in experimental results. *Experimental Thermal and Fluid Science*, 1:3–17, 1988.

Appendix A

Single-phase pressure drop

In order to design and fabricate thermo-fluid dynamic microdevices (Micro-Electro-Mechanical Systems - MEMS) the fluid flow phenomena at the microlevel have to be known well. Researchers are still looking for what are the differences at this scale with classical theory - if there are any. Some studies claimed that the pressure drop and the flow characteristic in a microchannel cannot be correctly predicted using existing models and classical correlations for large channels. Therefore, new correlations were generated to describe the fluid phenomena with better accuracy. Others found that it is usually measurement accuracy that is at the heart of these discrepancies. It should be pointed out, however, that several effects, which are normally neglected at macroscale, may become significant at microscale.

To underpin this statement, this chapter presents the pressure drop behaviour in microchannels with a wide range of experimental conditions, incorporating the work of three independent institutions (ENEA[1], IKE[2], KTH[3]) which cooperated in the project Heat and Mass Transfer in Microchannels (HMTMIC) funded by the European Union in the frame of the programme "Improving the Human Research Potential and Socio-Economic Knowledge Base". The presented single-phase pressure drop data were already published in reference [93], where set-ups used by the other institutes are described in detail.

The placement of pressure sensors allows to measure total and frictional pressure drop. The relationship between those is explained by means of Fig. A.1. All pressure sensors were connected by a pipe filled with water.
The difference between the absolute inlet and outlet pressures results in the

[1]Ente per le Nuove Tecnologie, l'Energie e l'Ambiente Sezione, Istituto di Termofluidodinamica Energetica, Rome, Italy

[2]Institut für Kernenergetik und Energiesysteme, Abteilung Energiewandlung und Wärmetechnik, Universität Stuttgart, Germany

[3]Kungliga Tekniska Högskolan, Department of Energy Technology, Stockholm, Sweden

total pressure drop.

$$\Delta p_{total} = p_{in} - p_{out} \tag{A.1}$$

The measured differential pressure can be described by Eq. A.2.

$$\Delta p_{measured} = p_{left} - p_{right} \tag{A.2}$$

where p_{left} and p_{right} are the pressures on the left/right side of the differential pressure sensor and p_{left} equals the inlet pressure and p_{right} is calculated with the Bernoulli equation.

$$p_{right} = p_{out} + \rho g h \tag{A.3}$$

Assuming that the acceleration pressure drop is negligible, the measured differential pressure is approximately equal to the frictional pressure drop, Eq. A.4

$$\Delta p_{measured} = p_{in} - p_{right} = p_{in} - p_{out} - \rho g h = \Delta p_{total} - \Delta p_G \approxeq \Delta p_F \tag{A.4}$$

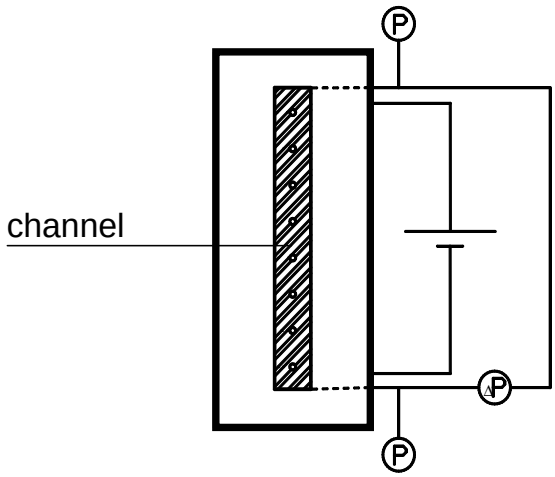

Figure A.1: Pressure measurement system

For single-phase flow it is convenient to present fluid hydrodynamic properties in terms of the friction factor which can be calculated from the Darcy-Weisbach equation, Eq. A.5.

$$\Delta p = 0.5 f \frac{G^2}{\rho} \frac{L}{d_h} \tag{A.5}$$

For conventional channels there are well-known correlations to predict the single-phase friction factor in a circular technical smooth tube for laminar and turbulent flow. The Hagen-Poiseuille correlation (Eq. A.6) for laminar flow and the Blasius correlation (Eq. A.7) for turbulent flow are commonly used.

$$f_c = \frac{64}{Re} \qquad Re \leqslant 2300 \tag{A.6}$$

$$f_c = \frac{0.3164}{Re^{0.25}} \qquad 2300 < Re \leqslant 10^5 \tag{A.7}$$

For rectangular conventional channels, Shah and London [94] and Kakac et al. [95] have proposed a modification of the Hagen-Poiseuille and the Blasius equations. Both correlations are multiplied with different factors which are dependent on the channel aspect ratio.

For laminar flow: Shah and London [94]

$$f = \frac{96}{Re}\left(1 - 1.3553a + 1.19467a^2 - 1.7012a^3 + 0.9564a^4 - 0.2537a^5\right) \tag{A.8}$$

For fully developed turbulent flow Eq. A.9 was published by Kakac et al. [95].

$$f = f_c(1.0875 - 0.1125a) \tag{A.9}$$

where f_c is friction factor for a circular channel.

Taking into account the influence of the temperature profile on the friction factor for diabatic conditions, a correlation (Eq. A.10) was suggested by Tong et al. [96] for fully developed turbulent flow and by Steinke and Kandlikar [76] for laminar flow.

$$\frac{f}{f_{ad}} = \left(\frac{\mu_w}{\mu_{ave}}\right)^b \tag{A.10}$$

with $b = 0.163$ and -0.58 according to [96] and [76], respectively.

Experimental friction factor

The experimental friction factor is calculated from the Darcy-Weisbach equation (Eq. A.5) and compared with the Hagen-Poiseuille (Eq. A.6) and the Blasius (Eq. A.7) correlations.

In Fig. A.2 the experimental friction factor for adiabatic conditions is shown. It can be seen that the Hagen-Poiseuille and the Blasius equations work well for small hydraulic diameter channels, regardless of working fluid, channel cross-sectional shape and inclination.

Model predictions

As mentioned earlier, the total pressure drop is caused by shear stress (frictional part), density change (acceleration part) and gravity. The weight of these terms as calculated by the model is summarised in Table A.1 for adiabatic conditions. Additionally, in Fig. A.3 the frictional (closed symbols) and gravitational

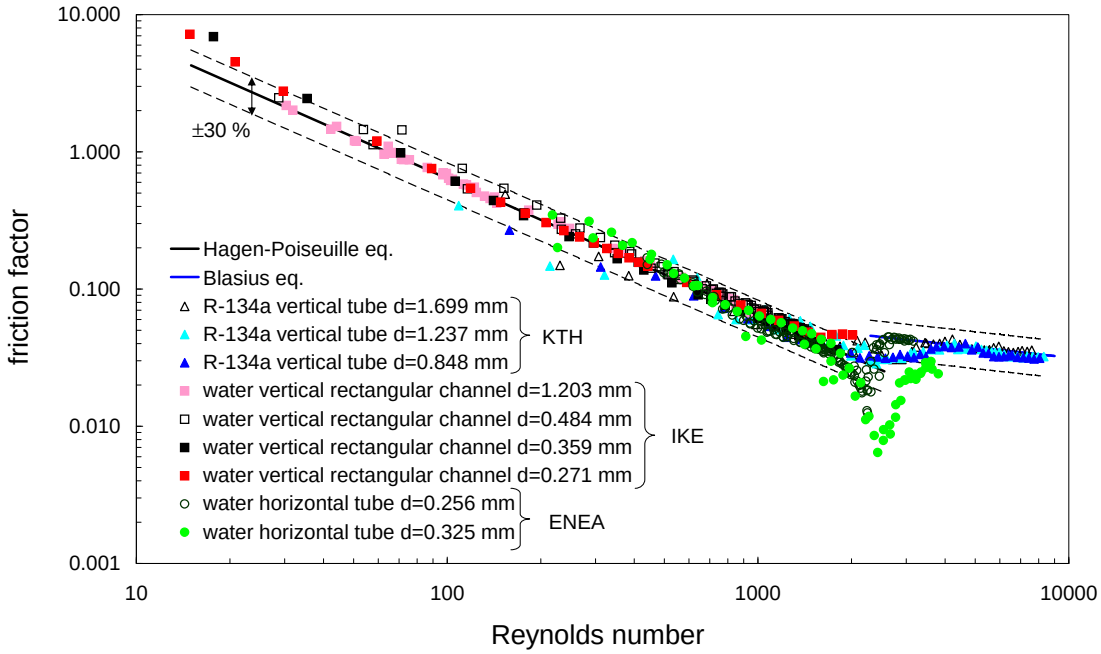

Figure A.2: Friction factor under adiabatic conditions

(open symbols) contributions to the total pressure drop are plotted for adiabatic flow of water (IKE) and R-134a (KTH). For adiabatic flow the acceleration part is zero due to the absence of (temperature dependent) density change. Since the tubes investigated by ENEA were in horizontal position, the gravity part for those results also becomes zero. The influence of fluid properties should not be omitted. The density ratio of R-134a to water at $25°C$ is equal to 1.2 and the viscosity of water at the same temperature is about 4.5 times higher than the viscosity of R-134a. Because of higher liquid density and lower viscosity the influence of the gravity term is expected to be stronger for R-134a than for water. The frictional contribution to the total pressure drop exceeds the gravitational one only over a specific mass flux. Due to the dependence of the frictional part on the 5^{th} power of the diameter, for the smallest channels this inversion point happens already at very low mass fluxes. For example, for R-134a in tubes with diameters 0.848 and 1.237 mm this point occurs at about 800 ($Re = 3200$) and 1000 kg/m^2s ($Re = 6200$), respectively. For the rectangular channel with water (hydraulic diameter 1.2 mm) this point occurs at about 500 kg/m^2s ($Re = 530$). The influence of shear stress increases with a decrease of hydraulic diameter and with higher viscosity (see the ≈ 1.2 mm channels with water and R-134a in Fig. A.3).

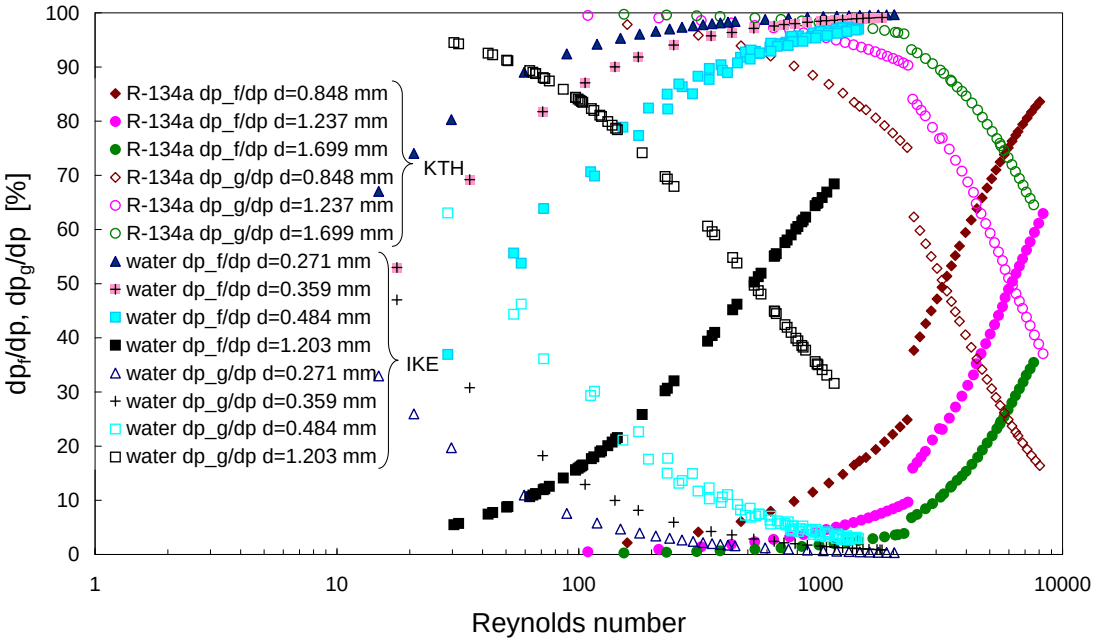

Figure A.3: Variation of percentage of frictional and gravity parts in total pressure drop under adiabatic condition for water and R-134a

Frictional pressure drop

Experimental frictional pressure drop data are presented and compared to predictions from the model. In the adiabatic pressure drop experiments performed at KTH with R-134a, the gravity term was eliminated by calibration. The measurements of the other groups contain all pressure drop terms, but the gravity contribution can be neglected: the position of tubes at ENEA was horizontal while additional measurements done at IKE for vertical channels (see Chapter 3.3) proved the gravity term to be insignificant for the mass flow rates considered. In all cases, the acceleration term can be disregarded because of the small density change within the working temperature ranges. Eq. A.5, with the friction factor rewritten as K/Re (where K (the Poiseuille constant) equals 64 - see Eq. A.6), becomes:

$$\frac{\Delta p}{L} = 0.5K\frac{\mu G}{\rho d_h^2} \tag{A.11}$$

This is the frictional pressure drop per unit length. For equal diameters, this quantity depends on fluid properties (i.e. dynamic viscosity μ), mass flux (i.e. bulk velocity u) and channel geometry (i.e. Poiseuille constant K). These separate influences are depicted in Figs. A.4 and A.5.

Figure A.4 shows the dependence of (hydraulic) diameter and the channel

geometry on the pressure gradient for adiabatic flow conditions. It is obvious that with decreasing channel size the pressure drop increases. For the circular and rectangular channels with practically equal hydraulic diameters (0.256 and 0.271 *mm*, respectively) it can be seen how the data points are overlaying. This proves the effect of channel shape to be very small at the aspect ratio considered and therefore justifies the use of the uncorrected correlations, Eqs. (A.6, A.7).

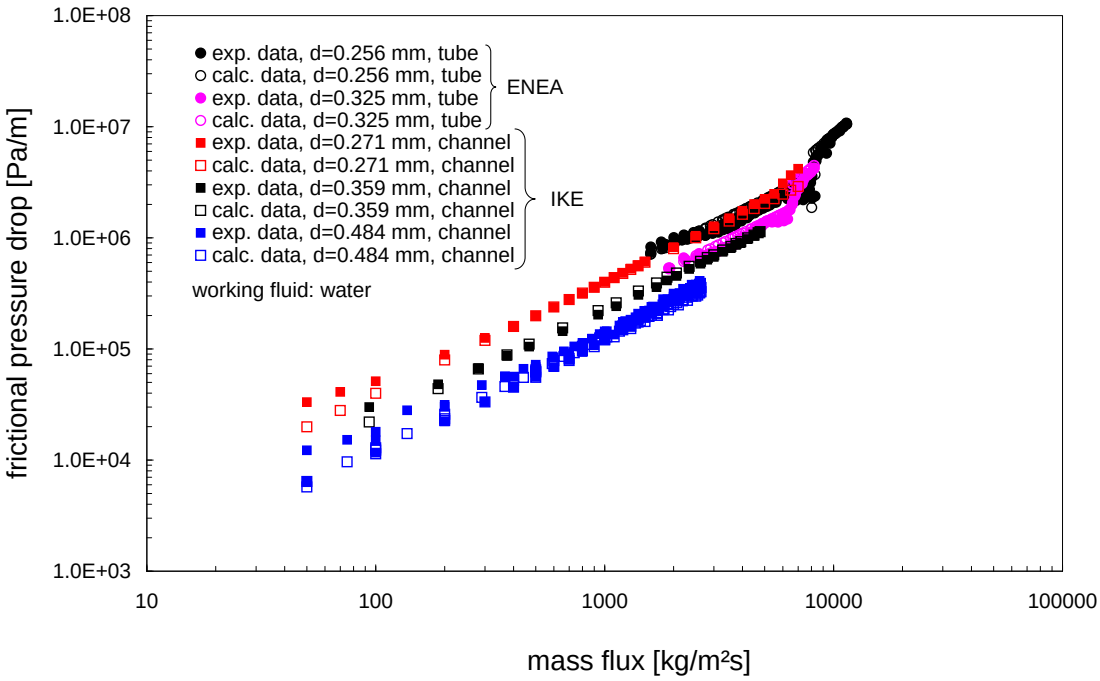

Figure A.4: Frictional pressure drop vs. mass flux for $d_h < 0.5$ *mm* under adiabatic conditions

In Fig. A.5 the effect of fluid properties (viscosity) is shown (fluids: water and R134a). The frictional pressure drop for water is shown to be larger than for R-134a for equal mass flux and similar hydraulic diameters; e. g. 1.203 and 1.237 *mm*, respectively. This is explained by the higher viscosity of water causing higher shear stress. No large effect of the different channel shape is observed.

From Figs. A.4 and A.5 it is clear that predictions agree well with the experimental results. The average deviations and the percentages of agreements within 10 % and 30 % are given in Table A.1.

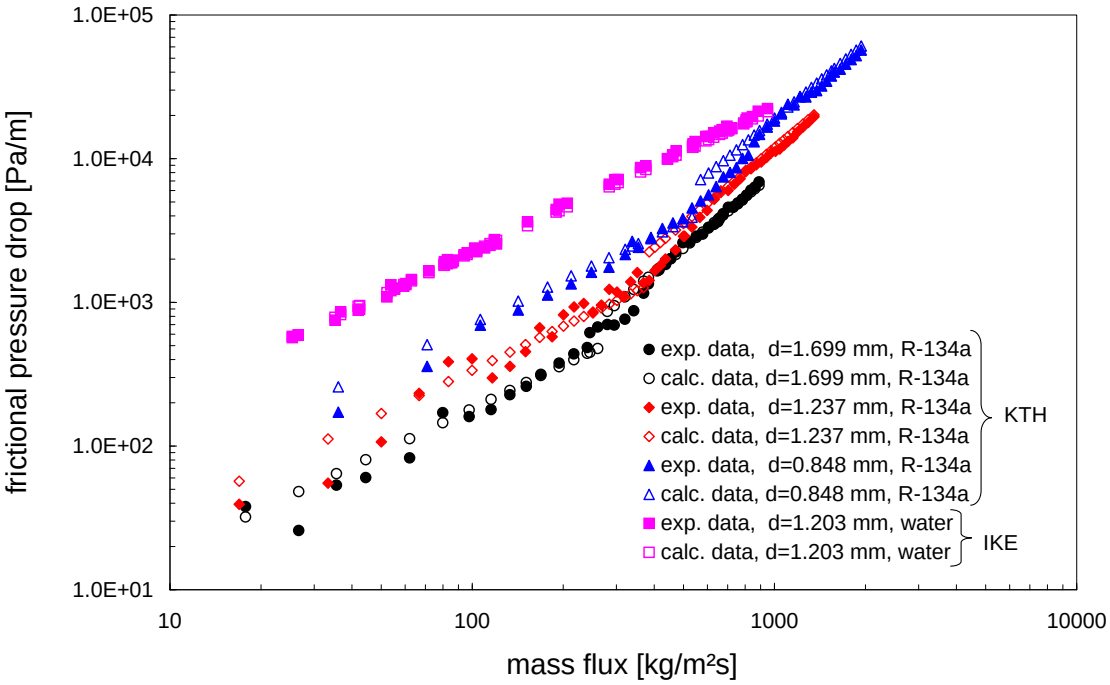

Figure A.5: Frictional pressure drop vs. mass flux for $d_h > 0.5$ *mm* under adiabatic conditions (R-134a (KTH) and water (IKE) flowed in vertical tubes and rectangular channels, respectively)

Summary

An evaluation of frictional single-phase pressure drop in micro-conduits was carried out, taking into consideration such quantities as channel hydraulic diameter (0.259 to 1.699 *mm*), shape (circular, rectangular) and aspect ratio, inclination, working fluid (water and R-134a) and mass fluxes.

Excellent agreement was verified between the experimental friction factor data and the Hagen-Poiseuille and the Blasius equations, down to $d_h = 0.259$ *mm*, regardless of channel shape, inclination and working fluid. **Classical theory can therefore describe the single-phase pressure drop in small hydraulic diameter channels for different fluids and geometry.**

Table A.1: Calculated data and comparison with experiments for adiabatic flow

	hydraulic diameter, d_h [mm]	aspect ratio [-], orientation	mass flux G [kg/m^{2}s]	(dp_f/dp) [%]	(dp_g/dp) [%]	(dp_a/dp) [%]	MAE [%]	percentage of exp. data within ±10 %	percentage of exp. data within ±30 %
ENEA	0.325	circular, horizontal	400 – 10000	100	0	0	13	61	93
	0.259	circular, horizontal	1500 – 11500	100	0	0	34	35	60
IKE	1.203 (0.86 x 2.0 mm²)	0.43 vertical	25 – 40 50 – 900	5 – 9 10 – 69	95 – 91 90 – 31	0	2	100	100
	0.484 (0.807 x 0.346 mm²)	0.43 vertical	50 – 1000 1200 – 2600	39 – 94 94 – 98	61 – 6 6 – 2	0	6	84	100
	0.359 (0.550 x 0.266 mm²)	0.48 vertical	50 – 1000 1000 - 5000	53 – 96 96 - 99	47 – 4 4 - 1	0	7	92	100
	0.271 (0.289 x 0.255 mm²)	0.88 vertical	50 – 1000 1100 – 7000	67 – 98 98 – 100	33 – 2 2 – 0.3	0	6	76	93
KTH	1.699	circular, vertical	15 – 900	0.2 – 36	65 – 51	0	11	65	93
	1.237	circular, vertical	15 – 1000 1000 – 1400	0.4 – 49 50 – 63	100 – 100 50 – 37	0	14	53	90
	0.848	circular, vertical	30 – 1000 1000 – 2000	2 – 59 62 – 84	98 – 41 38 – 16	0	15	59	98

Appendix B

Estimation of heat loss function

Based on a heat balance for diabatic single-phase flow (Eq. 3.36) the heat loss was calculated for the channels. The heat loss functions generated by linear regression as functions of average wall temperature represented the measured heat losses with an accuracy of $\pm 4\ W$, $\pm 7\ W$ and $\pm 7\ W$ respectively for the three channels (Fig. B.1a-B.1c). The error bands overlap about 80% of the presented data points. Note, the average wall temperature ranges start from $70°C$ which approximately corresponds to two-phase average wall temperature ranges. The respective heat loss functions used for the two-phase flow experiments are given by Eq. B.1.

$$\begin{aligned} Q_{loss} &= 0.59324\,(T_w)_{ave} - 15.676 && \text{for } d_h = 0.271\ mm \\ Q_{loss} &= 0.011955\,(T_w)^2_{ave} - 1.2214\,(T_w)_{ave} + 36.264 && \text{for } d_h = 0.359\ mm \\ Q_{loss} &= 0.007656\,(T_w)^2_{ave} - 0.58707\,(T_w)_{ave} + 13.102 && \text{for } d_h = 0.484\ mm \end{aligned} \quad \text{(B.1)}$$

where $(T_w)_{ave}$ is given in $°C$.

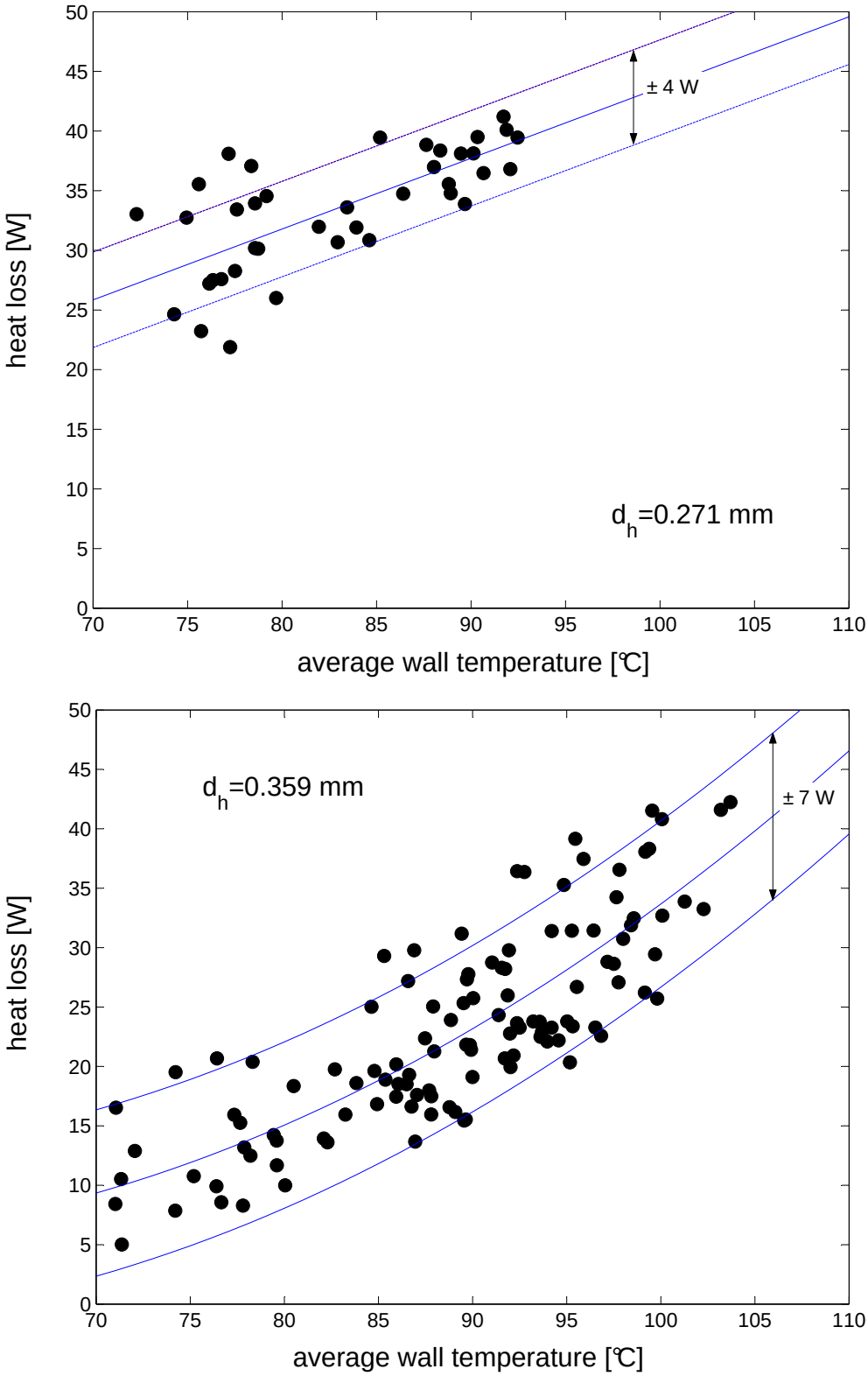

Figure B.1: Heat loss as a function of average wall temperature

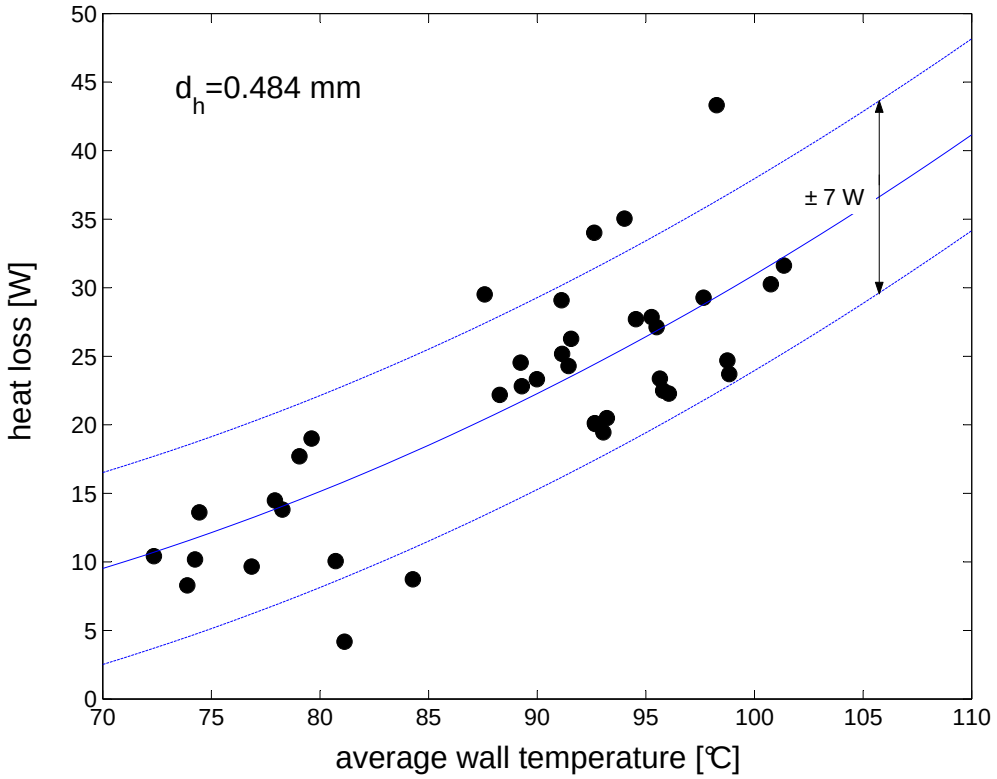

Figure B.1: Heat loss as a function of average wall temperature (continued)

Appendix C

Vapour slug elongation

During flow boiling investigations a difference between velocities at the top and at the bottom of a vapour slug was observed. There can be two reasons for this. First, the evaporation process causes a change of vapour mass. In consequence the slug expands in both directions. In the flow direction the expansion increases the velocity at the top. The expansion at the bottom works in opposite flow direction and hence the velocity is diminished.
Second reason can be due to the high pressure drop observed in microchannels. In case of long slugs the liquid pressure difference between their ends can be significant. The pressure difference within one slug can be calculated from the Bernoulli equation (Eq. C.1), with the assumption of non frictional vapour pressure loss.

$$p_{g,\,bottom}+\rho_{g,\,bottom}gh_{bottom}+\frac{u^2_{g,\,bottom}\rho_g}{2}=p_{g,\,top}+\rho_{g,\,top}gh_{top}+\frac{u^2_{g,\,top}\rho_{g,\,top}}{2} \quad \text{(C.1)}$$

A rough calculation was done for an extreme case, viz.: temperature equals $100\ ^\circ C$, the top and bottom velocity equals $10\ m/s$ and $0\ m/s$, respectively, and the slug length equals the channel length ($0.33\ m$). Considering these assumptions, Eq. C.1 can be rearranged into Eq. C.2.

$$p_{g,\,bottom}-p_{g,\,top}=\rho_{g,\,top}gh_{top}+\frac{u^2_{g,\,top}\rho_{g,\,top}}{2} \quad \text{(C.2)}$$

For such an extreme example the calculation shows a change of pressure within one slug of about $32\ Pa$. Obviously it is negligible in comparison with the pressure drop along the channel (min. value for the visualised cases is about $0.1\ bar$). A strong decrease in liquid pressure together with almost constant vapour pressure leads to different curvatures at the vapour body bottom and at the vapour body top.

Appendix D

Pressure drop model - algorithm

The measured pressure drop was compared with the separate flow model based on governing correlations (conservation of mass, energy and momentum), the Lockhart-Martinelli method and an empirical void fraction equation, Chapter 3.3. The theoretical predictions were calculated by means of a computer program (MATLAB 7.0) according to the algorithm presented below.

At the beginning of the program the input parameters have to be given. Then, it is checked if saturation occurs. In case of a subcooled condition (blue-line box) a pressure drop and a temperature increase is calculated for every step so long till saturation is achieved. This position is called Z_{sat}. Further, the two-phase pressure drop is calculated considering frictional, acceleration and gravitational terms (red-line box). The temperature in the saturation region is calculated based on the pressure profile.

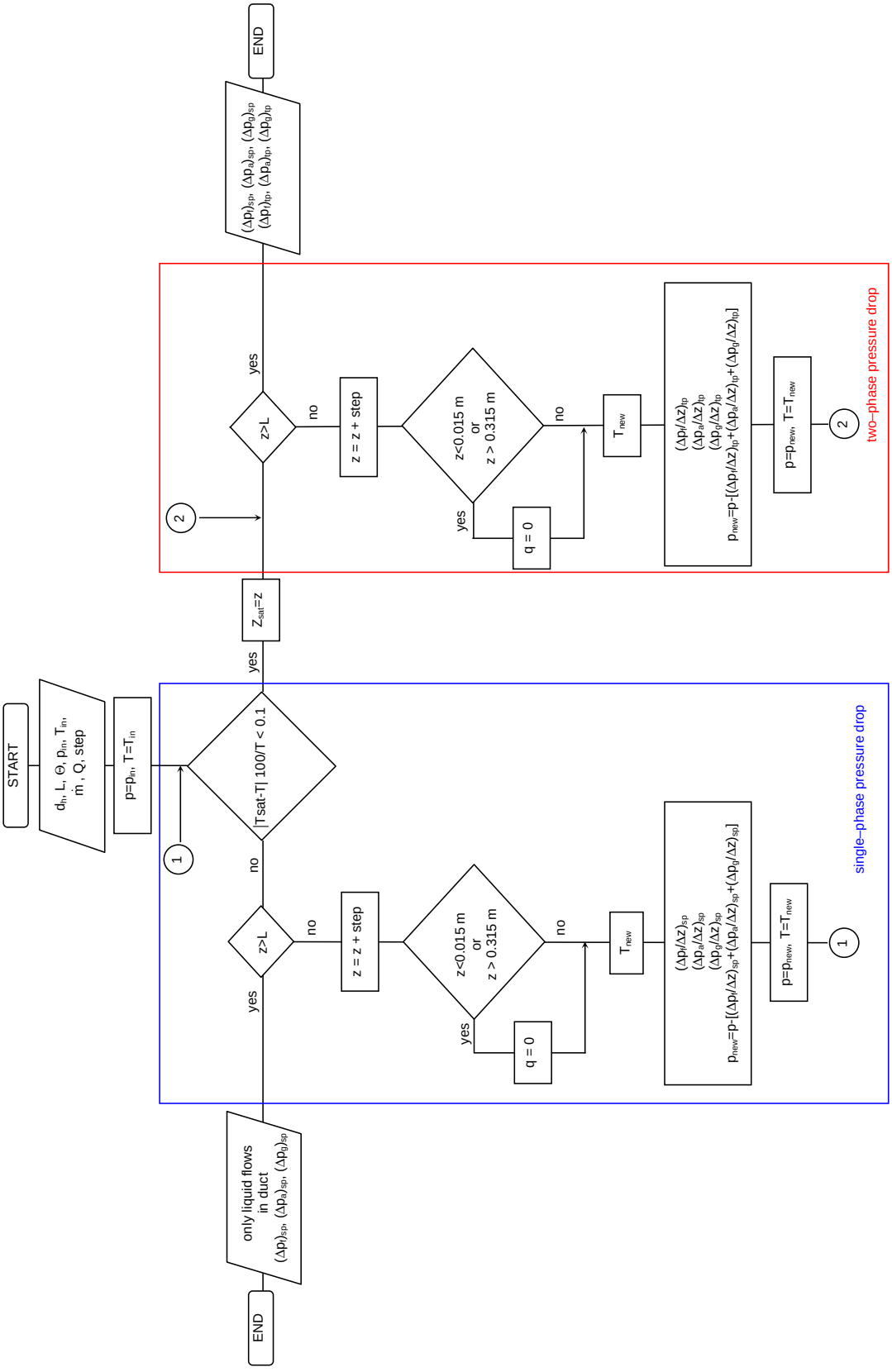
START
d_h, L, Θ, p_{in}, T_{in}, m , Q, step
$p=p_{in}$, $T=T_{in}$
1
|Tsat-T| 100/T < 0.1
yes
$Z_{sat}=z$
no
z>L
yes
no
z = z + step
z<0.015 m or z > 0.315 m
yes
q = 0
no
T_{new}
$(\Delta p_f/\Delta z)_{sp}$
$(\Delta p_a/\Delta z)_{sp}$
$(\Delta p_g/\Delta z)_{sp}$
$p_{new}=p-[(\Delta p_f/\Delta z)_{sp}+(\Delta p_a/\Delta z)_{sp}+(\Delta p_g/\Delta z)_{sp}]$
$p=p_{new}$, $T=T_{new}$
1
single–phase pressure drop
only liquid flows in duct
$(\Delta p_l)_{sp}$, $(\Delta p_a)_{sp}$, $(\Delta p_g)_{sp}$
END
2
z>L
yes
no
z = z + step
z<0.015 m or z > 0.315 m
yes
q = 0
no
T_{new}
$(\Delta p_f/\Delta z)_{tp}$
$(\Delta p_a/\Delta z)_{tp}$
$(\Delta p_g/\Delta z)_{tp}$
$p_{new}=p-[(\Delta p_f/\Delta z)_{tp}+(\Delta p_a/\Delta z)_{tp}+(\Delta p_g/\Delta z)_{tp}]$
$p=p_{new}$, $T=T_{new}$
2
two–phase pressure drop
$(\Delta p_l)_{sp}$, $(\Delta p_a)_{sp}$, $(\Delta p_g)_{sp}$
$(\Delta p_l)_{tp}$, $(\Delta p_a)_{tp}$, $(\Delta p_g)_{tp}$
END

Appendix E

Void fraction equation

The void fraction is defined as the gas-flow cross-sectional area A_g to the total cross-sectional area A_{cs}, Eq. 2.3. The direct measurement of the void fraction requires a special equipment and a special design of the set-up (e. g. two-laser-system and a borosilicate glass tube [http://ltcm.epfl.ch/page19417.html]). Therefore, the empirical correlation of the void fraction is commonly used.

The continuity equations for both phases are presented below [47].

$$A_{cs}G_g = A_{cs}Gx_{th} = \rho_g u_g A_g = \rho_g u_g A_{cs}\alpha \tag{E.1}$$

$$A_{cs}G_l = A_{cs}G(1-x_{th}) = \rho_l u_l A_l = \rho_l u_l A_{cs}(1-\alpha) \tag{E.2}$$

From Eq. E.1 and Eq. E.2 the correlation of slip ratio K' (Eq. E.3) is obtained.

$$\frac{x_{th}}{1-x_{th}} = \left(\frac{u_g}{u_l}\right)\left(\frac{\rho_g}{\rho_l}\right)\left(\frac{\alpha}{1-\alpha}\right)$$

$$K' = \frac{u_g}{u_l} = \left(\frac{x_{th}}{1-x_{th}}\right)\left(\frac{\rho_l}{\rho_g}\right)\left(\frac{1-\alpha}{\alpha}\right) \tag{E.3}$$

Rearranging Eq. E.3 the void fraction is defined.

$$\alpha = \left[1 + K'\left(\frac{1-x_{th}}{x_{th}}\right)\left(\frac{\rho_g}{\rho_l}\right)\right]^{-1} \tag{E.4}$$

Eq. E.4 provides the basic form of the void fraction equation, in which practically all empirical correlations are provided in the literature.

In general, for all practical problems x_{th}, ρ_l and ρ_g are known and/or specified for a given location. So the only unknown is the slip ratio. Once K' is computed "somehow", the void fraction follows for the specified boundary conditions. Thus, all empirical formulations for α are essentially based on determining the slip ratio.

The *homogeneous model* assumes that the liquid and gas phases flow have the same velocity $u_g = u_l$. Hence, it is the simplest empirical correlation for the slip ratio and makes $K' = 1$.

Slip ratio model: The so called "slip ratio" model gives an arbitrary numerical value for K'. The value may be completely arbitrary and generally applicable only for a particular experimental run or a small set of data. But indeed, giving a suitable value for K', solves the problem and makes α determinable, and "somehow" a fit can be obtained for the data. This approach is seriously limited in scope and application, but still works. It is, at the least, one level of sophistication higher than that of the homogeneous model.

Physical models: From a physical point of view the "slip" must be a function of individual thermophysical properties of the two phases. The density and the dynamic viscosity ratios are the most important to consider. Also, it may be argued that K' is a function of the thermodynamic vapour quality itself.

$$K' = f(p,\ x_{th}) \tag{E.5}$$

$$K' = f(\rho,\ \mu,\ x_{th}), \quad \rho,\ \mu = f(p) \tag{E.6}$$

$$K' = C_1 \left(\frac{1 - x_{th}}{x_{th}}\right)^a \left(\frac{\rho_g}{\rho_l}\right)^b \left(\frac{\mu_l}{\mu_g}\right)^c \tag{E.7}$$

Empirical data have been seen to fit this line of thinking and various correlations have been developed which take the general form. Substituting Eq. E.7 in Eq. E.4 the most general form of empirical correlation for the void fraction in terms of thermodynamic vapour quality and thermophysical properties of the two phases at the applicable pressure/temperature boundary condition is obtained (the same like Eq. 3.35).

$$\alpha = \left[1 + C_1 \left(\frac{1 - x_{th}}{x_{th}}\right)^{n_1} \left(\frac{\rho_g}{\rho_l}\right)^{n_2} \left(\frac{\mu_l}{\mu_g}\right)^{n_3}\right]^{-1} \tag{E.8}$$

The constants $C_1,\ n_1,\ n_2$ and n_3 are given in Table 3.3.

In Chapter 5.1 the experimental void fraction is described by Eq. E.8. The best agreement was obtained for the constants proposed by Lockhart and Martinelli with the change of exponent n_3 (from 0.07 to 0.3).
The effect of such change can be explained as follows. Note that the exponents c in Eq. E.7 and n_3 in Eq. E.8 are equal.

Considering only the viscosity term in Eq. E.7, it is obvious that with increasing n_3-exponent the slip ratio increases.

$$(K')_{n_3=0.07} = \left(\frac{u_g}{u_l}\right)_{n_3=0.07} \sim \left(\frac{\mu_l}{\mu_g}\right)^{n_3=0.07} < \left(\frac{\mu_l}{\mu_g}\right)^{n_3=0.3} \sim \left(\frac{u_g}{u_l}\right)_{n_3=0.3} = (K')_{n_3=0.3}$$

For constant gas velocity this leads to a reduction of the liquid velocity. From continuity equation, as a consequence of constant mass flow rate and lower liquid velocity, the liquid-flow cross-sectional area increases. This results in a lower A_g and then a lower void fraction (see also Fig. 5.6).

$$(u_l)_{n_3=0.07} > (u_l)_{n_3=0.3}, \quad u_g = const$$

$$(A_l)_{n_3=0.07} < (A_l)_{n_3=0.3}, \quad \dot{m}_l = A_l u_l \rho_l = const$$

$$(A_g)_{n_3=0.07} > (A_g)_{n_3=0.3}, \quad A_{cs} = A_g + A_l$$

$$(\alpha)_{n_3=0.07} > (\alpha)_{n_3=0.3}, \quad \alpha = \frac{A_g}{A_{cs}}$$

Appendix F

Calibration

The calibrations of measuring instruments were undertaken in order to improve their accuracy and to estimate a bias limit of parameters. The calibrations of pressure sensors and thermocouples were done before their installation. The flow meter was calibrated for every channel.
A computer program VEE Pro 6.0 was used to collect and save measured parameters as well as to control flow rate and heat input during experiments.

The calibration curves (function between electrical signals from instruments and real values given by a reference instrument) were obtained by linear regression. The coefficient of determination R^2 explains how much of the variability in the ordinate (y) can be explained by the fact that it is related to the abscissa (x), Eq. F.1.

$$R^2 = 1 - \frac{\text{var}\{x\}}{\text{var}\{y\}} = \frac{N(\sum xy) - (\sum x)(y)}{\sqrt{(N\sum x^2 - (\sum x)^2)\,(N\sum y^2 - y^2)}} \tag{F.1}$$

The average deviation (Eq. F.2) from the calibration curves was treated as measurement fixed error (bias limit) in further uncertainty analysis (Appendix G).

$$\Delta y = \frac{\sum \mid y_k - y_{curve} \mid}{N} \tag{F.2}$$

The obtained calibration curves for eight thermocouples and the used pressure sensors are presented in Fig. F.1 and Fig. F.2, respectively. In each graph the equation of the calibration curve and the coefficient of determination are shown. The obtained flow meter calibration curves were included in the computer program which controls the pump and hence the flow rate. Afterwards the tests were performed to validate these correlations and to determine a bias limit, Fig. F.3.

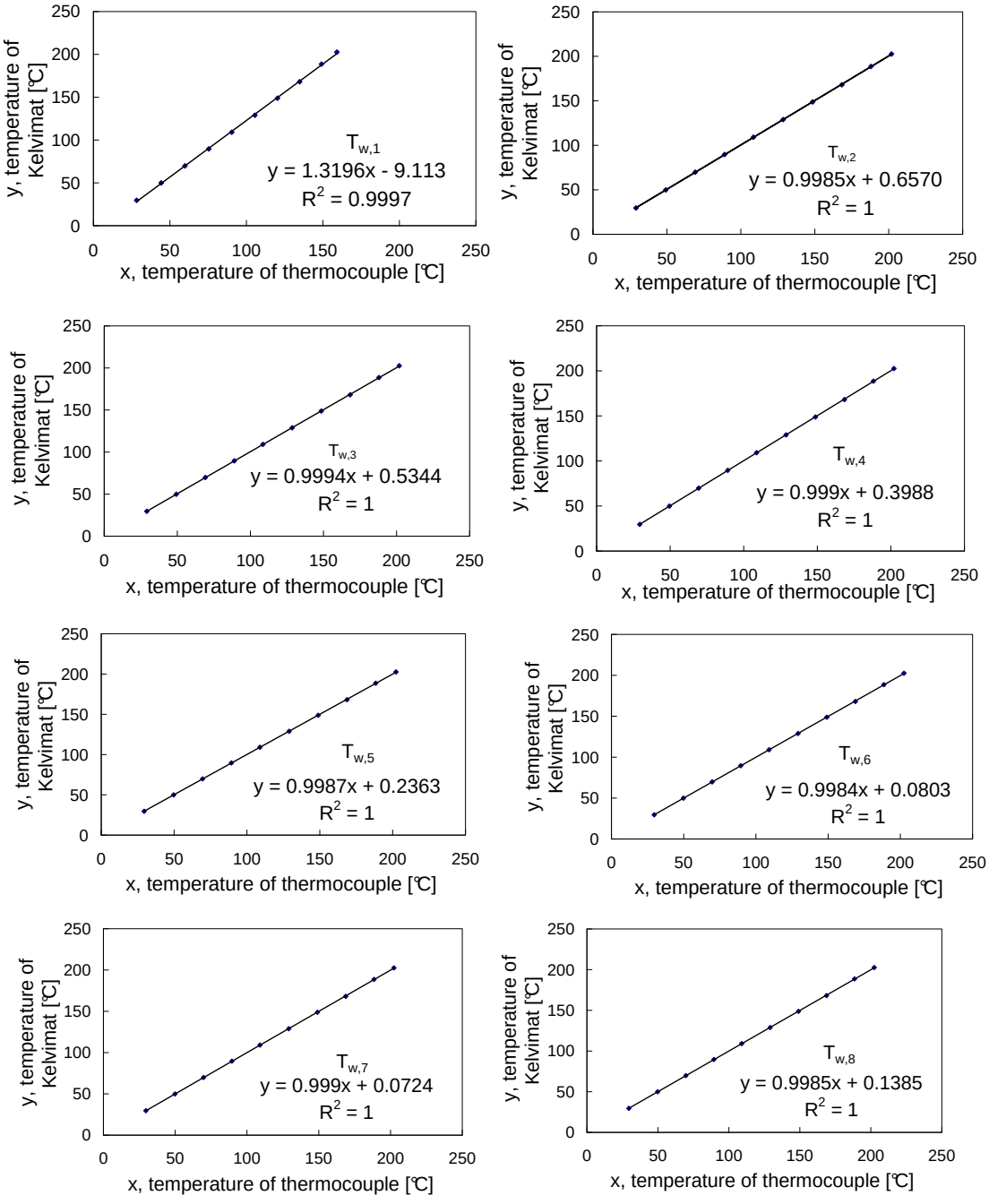

Figure F.1: Calibration curves of thermocouples (wall temperature)

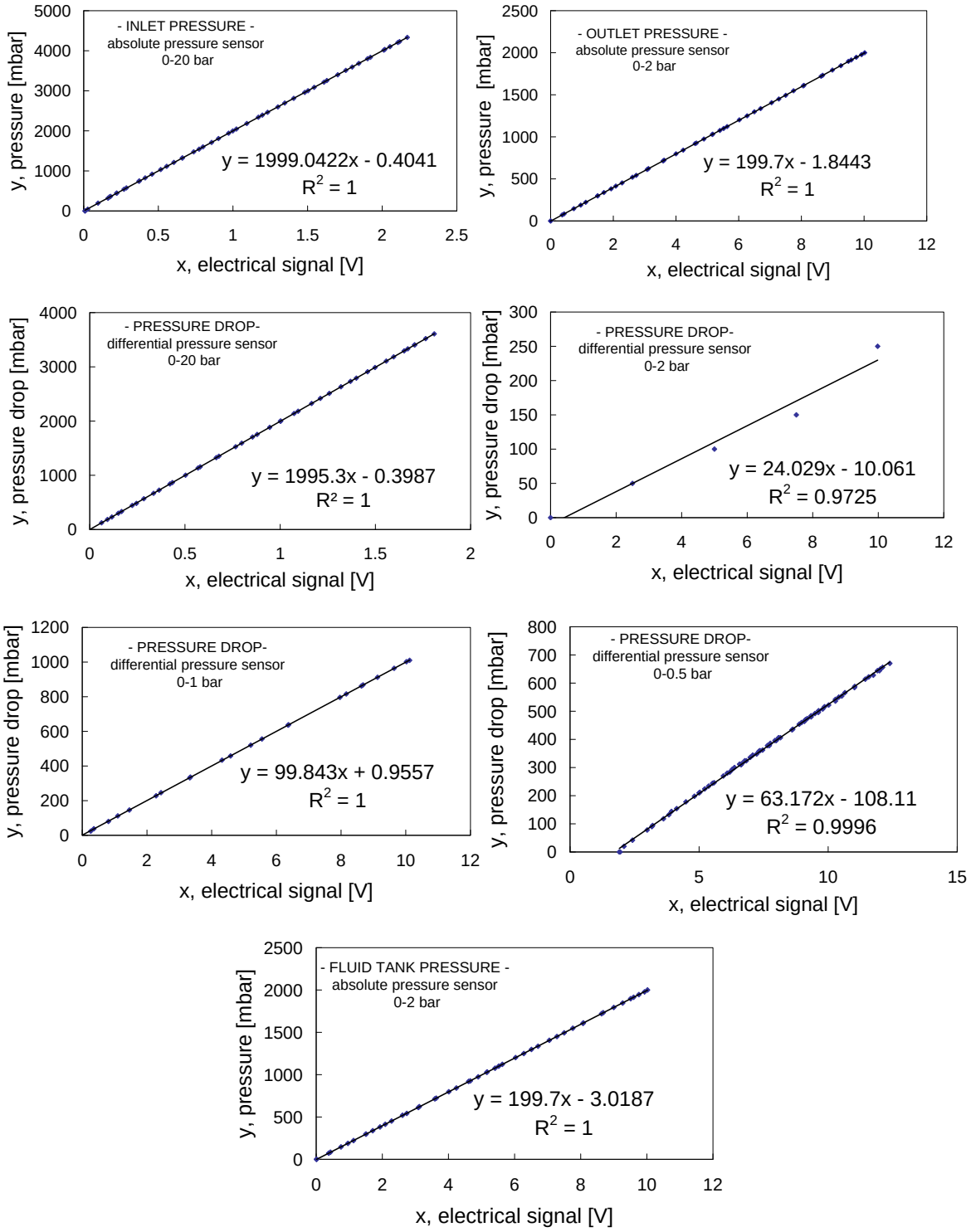

Figure F.2: Calibration curves of absolute and differential pressure sensors

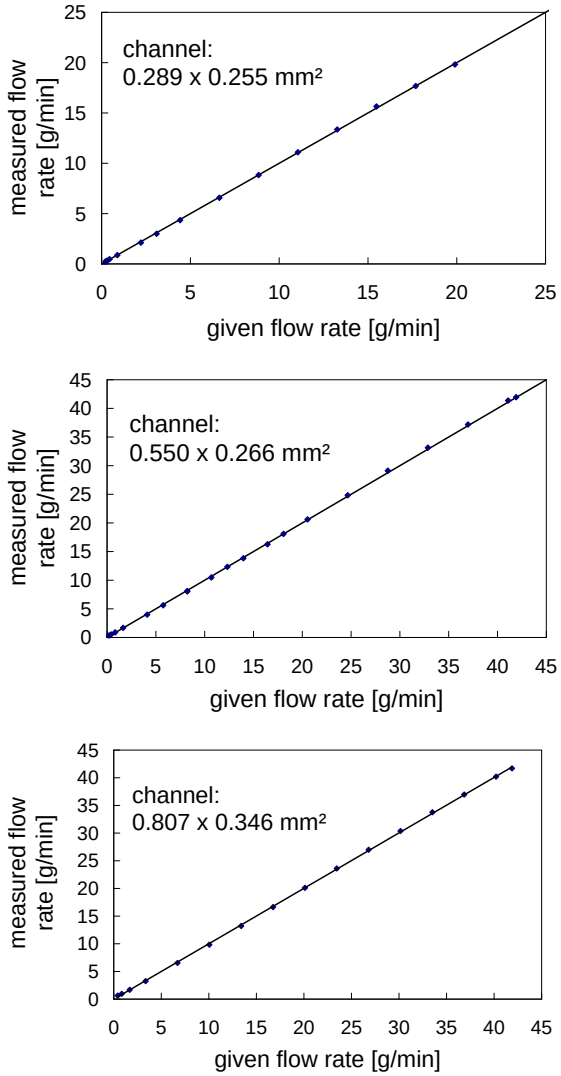

Figure F.3: Calibration curves of flow meter

Appendix G

Error analysis

The terms ”error” and ”uncertainty” can be traced back to S.J. Kline and F.A. McClintock [97] and still today their definitions are in common use in any error analysis. The error in measurement is the difference between true and measured value. In reality it is not easy to define what the error is. In most situations only the information, what the error might be, can be given. The ”uncertainty” gives ”a possible value that an error may have”.

The error sources are classified as ”fixed” (it does not change during an experiment), ”random” (it changes during an experiment) and ”variable but deterministic” (it changes during an experiment but not randomly). The general term ”variable error” is used to include both random and deterministic components of unsteady error. In the presented experiments each data set was obtained under steady state conditions. Hence the parameters are not changed during the investigation process, the third kind of error can be neglected and thus a total error δ is a sum of fixed and random error, Eq. G.1.

$$\delta = \beta + \epsilon \tag{G.1}$$

The fixed error (bias error) β is estimated by the bias limit and the random error (precision error) ϵ is estimated by the precision limit, Fig. G.1.

There are two ways to calculate the interval uncertainty (this is the interval around the mean value within which the true value is believed to lie): single-sample and multi-sample uncertainty analysis. All measurement parameters were collected under steady state conditions and saved by the computer program VEE Pro 6.0. The mean values of one hundred observations were used for further calculations. Hence, the multi-sample analysis could be used [98].

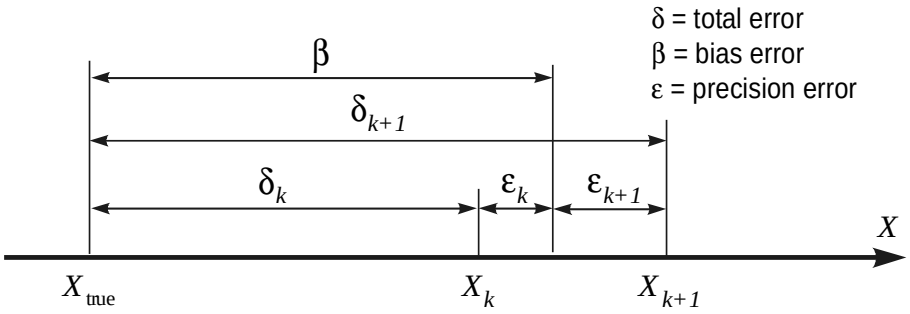

(a) two readings

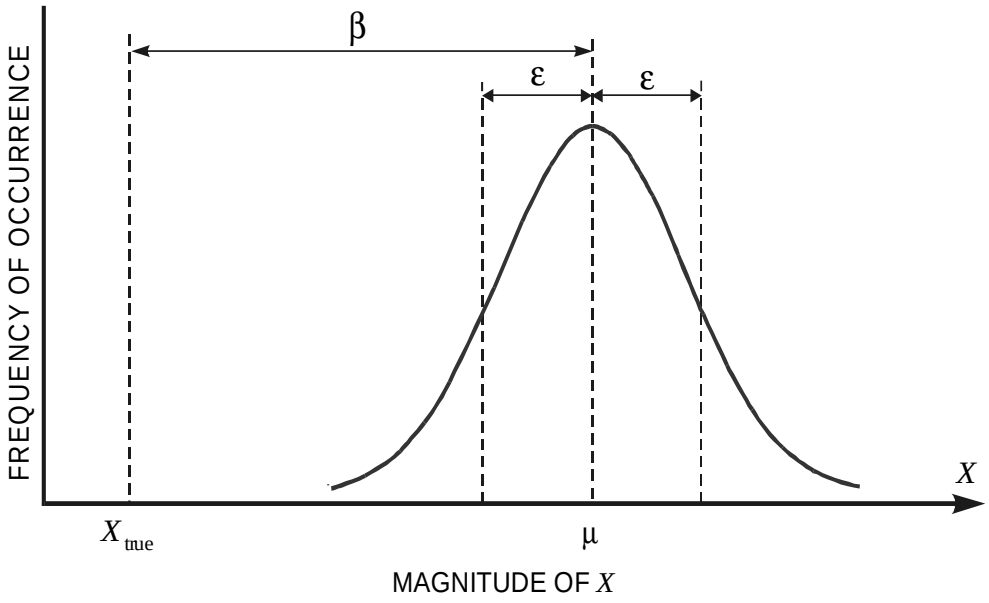

(b) infinite number of readings

Figure G.1: Illustration of error kinds by using Gaussian distribution

G.1 Overall uncertainty in a single measurement

The overall uncertainties for each measurement must include the measuring system uncertainties (after calibration, B_{cal}, S_{cal}) and additionally all those associated with system disturbance; system-sensor interactions (B_{int}, S_{int}) and the idealisations invoked in the data interpretation equations (B_{acq}, S_{acq}). Hence, the overall bias limit (Eq. G.2) and overall precision index (Eq. G.3) are the square root of combinations of all these fixed and random components, respectively.

$$B_x = \sqrt{B_{calc}^2 + B_{acq}^2 + B_{int}^2} \tag{G.2}$$

$$S_x = \sqrt{S_{calc}^2 + S_{acq}^2 + S_{int}^2} \tag{G.3}$$

In order to simplify the calculation, the fixed system-sensor interaction and data acquisition error are neglected. For the calibrated instruments the fixed error B_{calc} equals the average deviation (Eq. F.2). The geometry of the channels was measured by microscope and according to its properties the fixed error of geometry was given.

The precision index of a data set is equal to its standard deviation of the mean, $S_{\overline{x}}$.

$$S_{\overline{x}} = \left(\frac{\sum_{k=1}^{N} (x_{i,\,k} - \overline{x}_i)^2}{N(N-1)} \right)^{0.5} \tag{G.4}$$

The overall uncertainty in a single measurement includes the fixed and random terms. In Eq. G.5, t is the Student's multiplier for 95 % confidence and ν degrees of freedom. For a number of samples more than 10, the Student's multiplier is $t = 2$.

$$(U_{x_i})_{0.95} = \left(B_{x_i}^2 + (tS_{\overline{x_i}})^2 \right)^{0.5} \tag{G.5}$$

It can be noticed that the uncertainty in the results in multi-sample analysis, $(U_{x_i})_{0.95}$, corresponds to the zeroth-order uncertainty in simple-sample analysis.

In Table G.1 the working range, error (bias limit B_{x_i}) and overall uncertainty $(U_{x_i})_{0.95}$ of all measurement parameters are given. Note in all cases the precision indices ($S_{\overline{x}}$, $S_{\overline{y}}$) were equal zero or almost zero. Hence, these values are omitted (also in Tables G.2-G.6).

Table G.1: Uncertainty of measured parameters

measured parameter	instrument	working range of instrument	B_{xi}	$(U_{xi})_{0.95}$ [%]
flow rate	embedded in dosing pump DME 2	15 –2500 ml/h	± 0.06 g/min*	13 to 0.64
			± 0.14 g/min**	17 to 0.34
			± 0.14 g/min***	9 to 0.33
heating power	digital multimeter	0 – 1500 W	±1W	≈ 2
				≈ 2
				≈ 2
wall temperature (8 locations)	NiCr-Ni, type K, class 1	-40 – 1200 °C	± 0.2 °C	1
fluid temperature (inlet and outlet)	PT-100, type A	-200 – 600 °C	± 0.2 °C	0.5
pressure drop	piezoresistive pressure transducer	0 – $0.5{\cdot}10^5$ Pa*	± 250 Pa	≈ 1
		0 – $1.0{\cdot}10^5$ Pa**	± 100 Pa	≈ 2
		0 – $2.0{\cdot}10^5$ Pa***	± 100 Pa	≈ 1
		0 – $20{\cdot}10^5$ Pa	± 500 Pa	≈ 1
absolute pressure (channel inlet and outlet, fluid tank)	piezoresistive pressure transducer	0 – $2{\cdot}10^5$ Pa	± 200 Pa	≈ 0.3
		0 – $2{\cdot}10^5$ Pa	± 200 Pa	≈ 0.3
		0 – $20{\cdot}10^5$ Pa	± 500 Pa	≈ 0.4
channel geometry	width	see table 4.1	± 0.002 mm	<0.7
	height	see table 4.1	± 0.001 mm	<0.4
	length / heated length	330 / 300 mm	± 0.05 mm	0.015 / 0.017

*) for the 0.271 mm channel, **) for the 0.359 mm channel, ***) for the 0.484 mm channel

G.2 Overall uncertainty of a result

A lot of parameters like friction factor, heat transfer coefficient can not be directly measured but there are functions of independent variables, like e.g. temperature, which can be easily measured. In this case, the errors in the single measurements are included in the overall uncertainty of the result, $(U_y)_{0.95}$, by a similar equation like the overall uncertainty in a single measurement, G.5. Again the Student's multiplier for 95 % confidence and ν degrees of freedom is $t = 2$.

$$(U_y)_{0.95} = \left(B_y^2 + (tS_y)^2\right)^{0.5} \tag{G.6}$$

The bias limit and precision index of each measurement affect the fixed and random terms of the calculated results in proportion to their sensitivity coefficient (the partial derivative of results, y, with respect to the measurement, x_i). They are calculated by root-sum-square method and are given by Eq. G.7 and Eq. G.8, respectively.

$$B_y = \left(\sum_{i=1}^{M}\left(\frac{\partial y}{\partial x_i}B_i\right)^2\right)^{0.5} \qquad y = y(x_1,\ x_2 \cdots x_M) \tag{G.7}$$

$$S_y = \left(\sum_{i=1}^{M}\left(\frac{\partial y}{\partial x_i}S_{\overline{x_i}}\right)^2\right)^{0.5} \qquad y = y(x_1,\ x_2 \cdots x_M) \tag{G.8}$$

The thermophysical properties of the fluid were calculated from NIST- website http://webbook.nist.gov/chemistry/fluid/ (NIST: National Institute of Standards and Technology). Their bias error was assumed to be equal ± 1 % of property values.

In Table G.2 the uncertainties of geometrical parameters are given. The biggest error occurs for the smallest channels. Table G.3 presents the error analysis results for single-phase flow investigations. The uncertainty of parameters dependent on geometry and flow data (mass flux, the Reynolds number, friction factor) is below 17 %.

The uncertainty of diabatic flow results is relatively large (Table G.4), mostly because of not sufficient precise heat loss estimation (Appendix B). Note, the considered thermodynamic vapour quality can be equal to zero or almost zero. This could lead to an infinitely large uncertainty. So, in the table only the extreme values are given but it should be remembered that with decreasing absolute value of the parameter its error increases. The local heat transfer coefficient uncertainty is affected by uncertainties in mass and heat flux, e. g. for constant mass flux a lower heat flux gives a higher uncertainty than with

Table G.2: Uncertainty of geometrical parameters

parameter	channel	value	B_{y_i}	$(U_{y_i})_{0.95}$ [%]
hydraulic diameter [mm]	0.271 mm	0.271	$1.044 \cdot 10^{-3}$	0.39
	0.359 mm	0.359	$1.003 \cdot 10^{-3}$	0.28
	0.484 mm	0.484	$1.044 \cdot 10^{-3}$	0.22
cross-section area [mm^2]	0.271 mm	0.074	$5.86 \cdot 10^{-4}$	0.79
	0.359 mm	0.146	$7.65 \cdot 10^{-4}$	0.52
	0.484 mm	0.279	$10.63 \cdot 10^{-4}$	0.38
heat transfer area [mm^2]	0.271 mm	239.676	0.849	0.35
	0.359 mm	324.568	0.850	0.26
	0.484 mm	449.655	0.852	0.19

Table G.3: Uncertainty of adiabatic single-phase flow results

parameter	channel	range	B_{y_i}	$(U_{y_i})_{0.95}$ [%]
to mass flux [kg/m^2s]	0.271 mm	100 *to* 7000	13 *to* 57	13 *to* 0.8
	0.359 mm	100 *to* 5000	16 *to* 30	16 *to* 0.6
	0.484 mm	100 *to* 2600	9 *to* 13	9 *to* 0.4
Reynolds number [$-$]	0.271 mm	29 *to* 2020	3 *to* 28	10.3 *to* 1.4
	0.359 mm	35 *to* 1800	6 *to* 22	17 *to* 1.2
	0.484 mm	53 *to* 1436	4 *to* 17	7.5 *to* 1.2
friction factor [$-$]	0.271 mm	0.04 *to* 2.77	0.0006 *to* 0.3610	1.5 *to* 13
	0.359 mm	0.03 *to* 2.49	0.0004 *to* 0.4189	1.3 *to* 16.8
	0.484 mm	0.04 *to* 1.46	0.0005 *to* 0.1258	1.3 *to* 8.6

a higher heat flux (uncertainty in heat flux is based on the absolute error in estimated heat input).

Table G.4 is valid for the whole investigated range including also extreme cases. More detailed information is given in Tables G.5 and G.6, where, as an example, the uncertainties of similar points (viz. different channels but similar mass flux and heat flux) are given for the two bigger channels (a technical limitation does not allow to apply the same experimental conditions for the smallest channel). Additionally, a change of the heat transfer coefficient uncertainty along the channel is presented.
From these tables it is obvious that with increasing hydraulic diameter and with decreasing heat flux the result uncertainty decreases. A clear influence of mass flux is bigger not distinguishable. For some cases (e. g. 0.359 mm, 300 kg/m^2s, 85 kW/m^2) the heat transfer coefficient uncertainty changes along the channel in the way that the highest heat transfer coefficient has the high-

Table G.4: Uncertainty of two-phase flow results

parameter	channel	range	B_{y_i}	$(U_{y_i})_{0.95}$ [%]
mass flux $[kg/m^2s]$	0.271 *mm*	100 *to* 2000	13 *to* 21	13 *to* 1
	0.359 *mm*	100 *to* 4500	16 *to* 30	16 *to* 0.67
	0.484 *mm*	100 *to* 2500	9 *to* 13	9 *to* 0.52
heat flux $[kW/m^2]$	0.271 *mm*	19 *to* 148	≈ 17	89 *to* 11.5
	0.359 *mm*	25 *to* 462	≈ 22	88 *to* 4.8
	0.484 *mm*	18 *to* 335	≈ 16	89 *to* 4.8
thermodynamic vapour quality $[-]$	0.271 *mm*	-0.101 *to* 0.239	0.0028 *to* 0.0516	2.8 *to* 21.6
	0.359 *mm*	-0.172 *to* 0.756	0.0037 *to* 0.278	2.2 *to* 36.8
	0.484 *mm*	-0.101 *to* 0.662	0.0026 *to* 0.1332	2.6 *to* 20.2
heat transfer coefficient $[kW/m^2K]$	0.271 *mm*	2 *to* 80	0.63 *to* 64	11 *to* 90
	0.359 *mm*	0.78 *to* 80	0.49 *to* 56	4 *to* 88
	0.484 *mm*	0.88 *to* 80	0.38 *to* 72	4 *to* 87

est uncertainty. This can be explained as follows: for constant heat flux, the fluid-wall temperature difference determines the heat transfer coefficient value (Eq. 3.38). The smaller the temperature difference, the higher the heat transfer coefficient but also the higher the temperature difference uncertainty and in consequence the higher the heat transfer coefficient uncertainty.

Table G.5: Uncertainty of two-phase flow in the 0.359 *mm* channel

mass flux $[kg/m^2s]$	heat flux $[kW/m^2]$	uncertainty [%] of								
		heat flux	local heat transfer coefficient at position							
			$T_{w,1}$	$T_{w,2}$	$T_{w,3}$	$T_{w,4}$	$T_{w,5}$	$T_{w,6}$	$T_{w,7}$	$T_{w,8}$
300	51	42	47	47	41	49	44	42	42	41
	85	25	32	32	36	28	26	25	25	25
700	52	42	43	46	54	71	41	42	43	41
	85	26	26	30	25	25	29	27	26	25
1500	38	57	57	58	60	63	57	57	57	57
	80	27	27	29	32	38	50	30	29	28

Table G.6: Uncertainty of two-phase flow in the 0.484 *mm* channel

mass flux $[kg/m^2s]$	heat flux $[kW/m^2]$	uncertainty [%] of								
		heat flux	local heat transfer coefficient at position							
			$T_{w,1}$	$T_{w,2}$	$T_{w,3}$	$T_{w,4}$	$T_{w,5}$	$T_{w,6}$	$T_{w,7}$	$T_{w,8}$
300	56	42	30	43	44	45	46	37	38	33
	82	19	21	31	30	29	25	22	22	20
700	54	29	29	31	33	36	41	50	29	30
	85	18	18	20	23	27	18	19	28	23
1500	43	37	37	38	39	41	37	37	39	42
	85	18	18	19	21	23	27	19	21	20

Appendix H

Measurement of channel size and surface roughness

The channel height (Fig. H.1) and surface roughness of channel wall (Fig. H.2) were measured by the electron microscope at ENEA. The width of channel was measured by an optical microscope.

In Fig. H.1, shown as an example, there are four images obtained for the 0.484 mm channel ($0.807x0.346\ mm^2$). The measurement was performed at six different positions along the channel and an average value was taken as the channel height.

The imagines can be described as follows:

Top left: The 2D view of a square section of the channel taken by the profilometer from above is shown here. The colour legend on the side shows the height. Across this square picture a line with triangles at its extremities is drawn.

Top right ("Oblique Plot"): This is the 3D elaboration of the 2D picture (the image at top left). The axes x, y and z (in the colour legend) are placed for the measured space.

Bottom left ("Surface Profile"): This is the precise cross-sectional profile at the line position (a line with triangles at its ends in the top-left image). The green line shows the channel shape. The dashed white line is a reference level (top edge of channel) to the blue dashed line (level of the bottom right channel corner) from a perpendicular coordinate system. The coordinate values are given in the little window right next to the image ("Profile Plot"). The axial y location with respect to the reference plane (which is the upper surface) is marked, viz. the value $-343.1303\ \mu m$ is a channel height measured as the distance between two lines (white and blue) exactly at the bottom right corner of the channel profile.

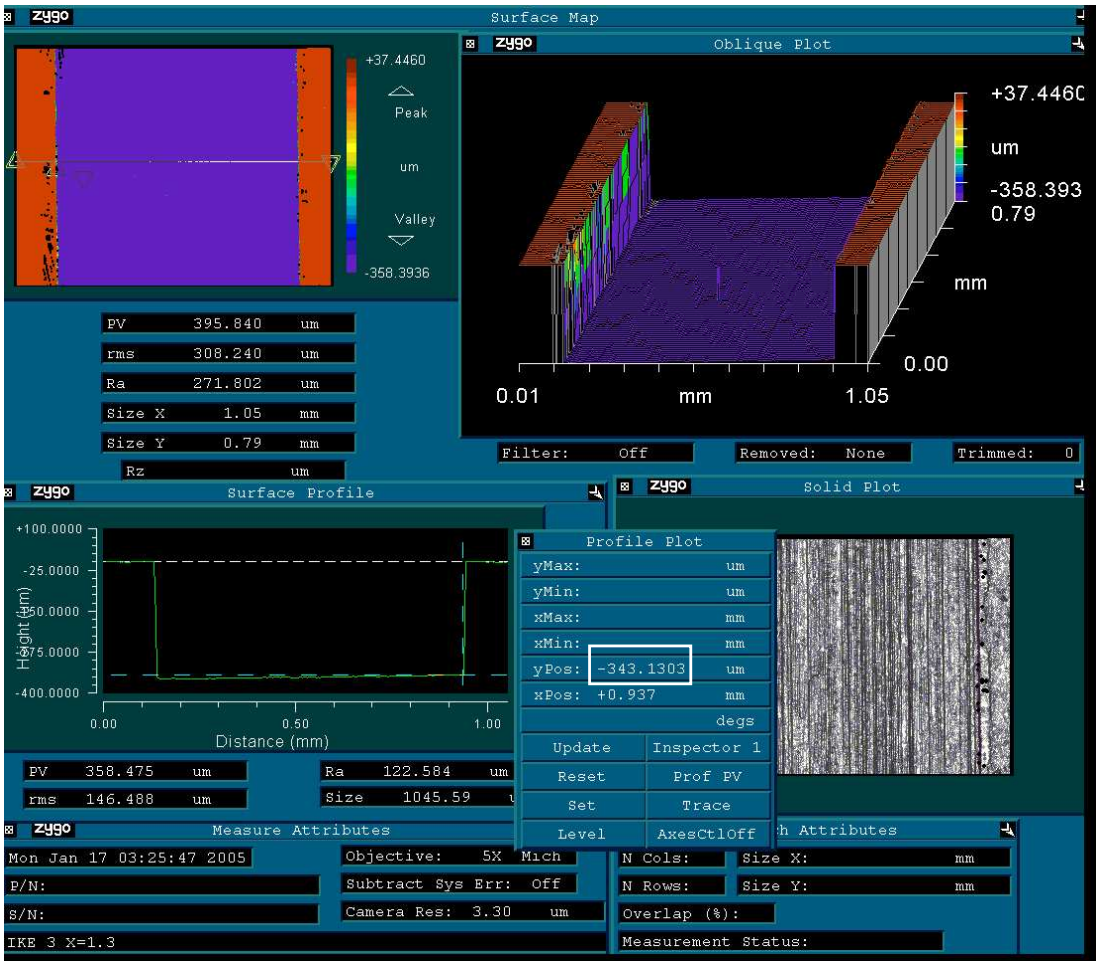

Figure H.1: Measurement of channel height

Bottom right ("Solid Plot"): A photo of the sample is shown.

Fig. H.2 presents the surface roughness results. An average deviation from the mean line R_a is used to described the surface properties. The first R_a-value (marked by solid-line box) is averaged over the entire plane of measurement. The second one (marked by dashed-line box) is averaged along the line drawn across the plane of measurement (line with triangles at the end in the top-left corner of the figure).

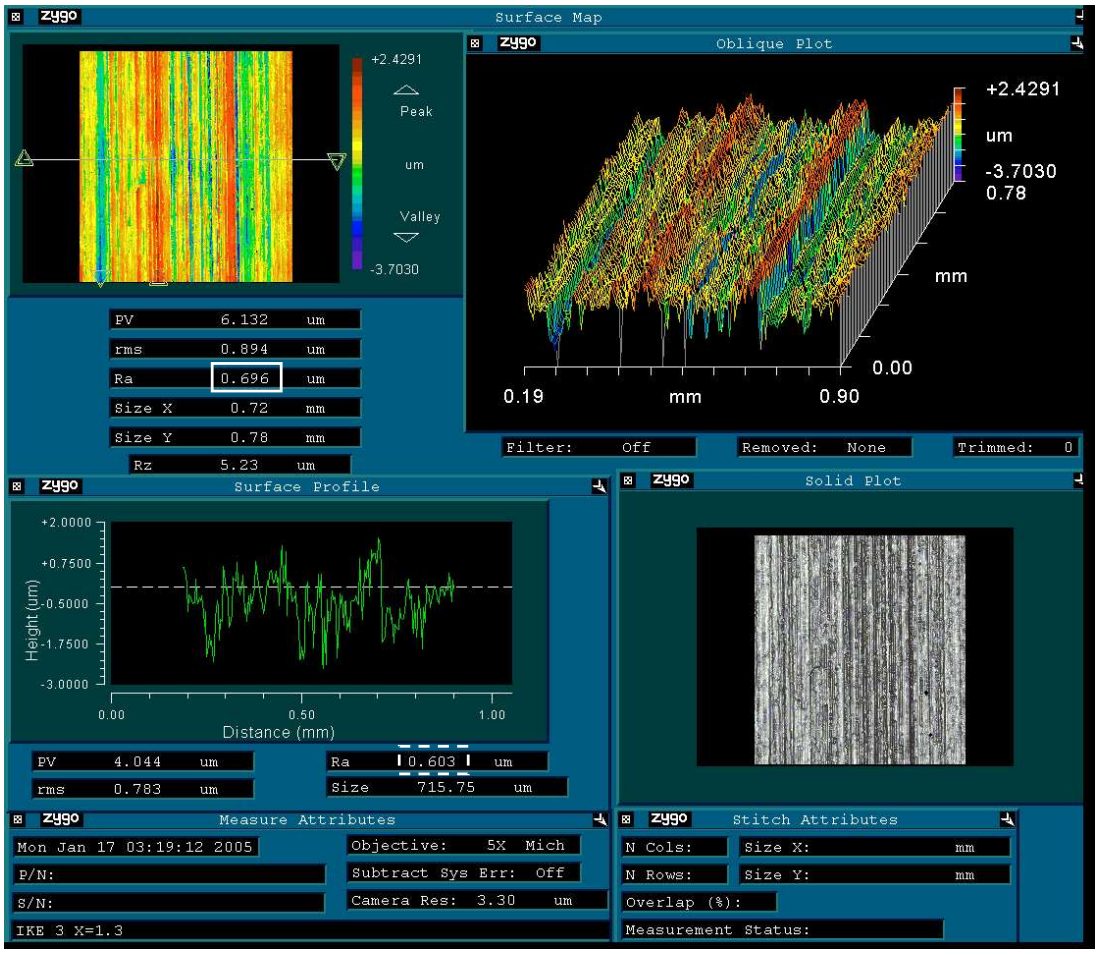

Figure H.2: Measurement of channel surface roughness